広島大学 学位論文

Electric-field Dependence of Local Structure in $BaTiO_3$ Probed by X-ray Absorption Spectroscopy and Reverse Monte Carlo Calculations

X線吸収分光法と逆モンテカルロ計算による $BaTiO_3$ における局所構造の電場依存性

Graduate School of Advanced Science and Engineering,
Hiroshima University
Seiya Kato

広島大学大学院先進理工系科学研究科
加藤 盛也

Thesis Outline

主論文

Electric-field Dependence of Local Structure in $BaTiO_3$ Probed by X-ray Absorption Spectroscopy and Reverse Monte Carlo Calculations

(X 線吸収分光法と逆モンテカルロ計算による
$BaTiO_3$ における局所構造の電場依存性)

公表論文

1. **Dielectric Response of $BaTiO_3$ Electronic States under AC Fields via Microsecond Time-resolved X-ray Absorption Spectroscopy**

   Seiya Kato, Nobuo Nakajima, Shintaro Yasui, Sou Yasuhara, Desheng Fu, Junichi Adachi, Hiroaki Nitani, Yasuo Takeichi, and Andris Anspoks

   Acta Materialia **207**, (2021) 116681.

参考論文

1. **Photoluminescence Mechanism of Self-activated Titanate Phosphors Investigated by X-ray Absorption Spectroscopy under UV Irradiation**

   Fan Dongxiao, Nobuo Nakajima, **Seiya Kato**

   Journal of Physics Condensed Matter **32** (2020) 355503.

2. **Elongation of Fe-Fe atomic pairs in the Invar alloy Fe65Ni35**

   Naoki Ishimatsu, Shun Iwasaki, Miu Kousa, **Seiya Kato**, Nobuo Nakajima, Naoto Kitamura, Naomi Kawamura, Masaichiro Mizumaki, Sho Kakizawa, Ryuichi Nomura, Tetsuo Irifune, and Hitoshi Sumiya

   Physical Review B **103** (2021) L220102.

主論文

Doctoral Thesis

Electric-field Dependence of Local Structure in $BaTiO_3$ Probed by X-ray Absorption Spectroscopy and Reverse Monte Carlo Calculations

Graduate School of Advanced Science and Engineering,
Hiroshima University
Seiya Kato

Abstract

Barium titanate ($BaTiO_3$) is a prototypical ferroelectric material, exhibiting the spontaneous electric polarization reversal under electric fields. This reversible polarization is caused by atomic displacements with asymmetrical distributions of positive and negative charges. The charge distributions are affected by not only atomic positions but also covalent bonds, producing a charge transfer from one atom to the other. Therefore, atomic-scale structure and electronic properties are crucial for understanding the dielectric properties of ferroelectric materials and controlling the functionality utilized in their practical applications.

In this thesis, the atomic structure and electronic states in $BaTiO_3$ under applied electric fields were investigated by X-ray absorption spectroscopies (XAS). The experimental spectra were supported by the reverse Monte Carlo (RMC) calculations combined with *ab initio* multiple-scattering calculations. The XAS is a useful technique to obtain information on electronic states and local structure around a specific element. The Ti K-edge spectra were analyzed to probe the Ti electronic state, whereas the Ba K-edge spectra were used to determine the local structure.

The detection of atomic displacements enhanced by applied electric fields remains a challenge because atomic displacements are small and of order 0.1 pm. The RMC refinements fully utilize structural information acquired from XAS, which are sufficient to detect atomic perturbations. Further, the obtained structure model also reflects the electronic states under electric fields, providing a unified interpretation of both structural and electronic information.

The obtained results indicate the Ba–O hybridization is enhanced as well as the well-known Ti–O covalency when picometer-scale Ti displacements are induced by applied electronic fields. The Ti displacements relative to oxygen and Ba atoms were separately estimated by analyzing Ba K-edge and Ti K-edge spectra. The observed difference between the two types of Ti displacements implies the coexistence of displacive and order-disorder characters. These results and analytical schemes will aid the understanding of local structures related to macroscopic phenomena such as the electromechanical properties of ferroelectric materials.

Contents

List of Figures

Chapter 1

Introduction

1.1 General introduction and motivation

Atomic-scale structures and electronic properties are crucial in materials science because functions of materials, including electric/thermal conductivities and magnetism, are realized by electrons. Although atomic structures and electronic properties are in microscopic perspectives, macroscopic properties can be also predicted by utilizing theoretical and computational calculations such as density functional theory and molecular orbital method. Therefore, the investigation of atomic structural information is the first step to understand a wide variety of microscopic/macroscopic properties of functional materials including the mechanical, thermal, optical, and electromagnetic properties.

The most common method to investigate atomic structure is the diffraction method. This method is sensitive to the symmetry in the lattice structure of crystalline materials since it is based on Bragg's law to determine the long-range order in atomic structure. Diffraction techniques can provide excellent information on average atomic structure, whereas it is difficult to observe local atomic structure.

Local structure is a significant factor in functional materials due to the recent development of nano-scale devices. Nanotechnology has tremendously increased the demand for local structural analysis because short-range interaction is more dominant in smaller materials. Therefore, it is essential to investigate the local structure as well as the average structure for the progress in materials science and future applications to electronic devices.

One of the attractive research targets is a dielectric/ferroelectric material, which has been widely used in electronic devices, including multilayer ceramic capacitors, actuators, and memory cells. A prototypical ferroelec-

tric $BaTiO_3$ system markedly changes dielectric behaviors with small atomic perturbations, which induces no changes in the lattice symmetry.

For example, the piezoelectric characteristics, the Curie temperature, and the frequency dependence of dielectric constants can be tuned using chemical substitutions. The Curie temperature of a $BaTiO_3$-based system can be tuned using Sr, Ca, and other substituent ions [1, 2, 3, 4]. Sr, Ca, or Sn substitutions induce diffuse phase transition behaviors [5, 6, 7], which are characterized by the strong frequency dependence of the dielectric permittivity. The piezoelectricity can also be tuned using doping ions; notably, the piezoelectricity is enhanced by doping Li^{+}–Al^{3+} ionic pairs [8] and co-doping Co/Nb [9].

These variations of the dielectric properties occur even if the lattice symmetry remains unchanged after the chemical substitutions, indicating the importance of local atomic displacements. Further, in a $BaTiO_3$-based system, the displacement of Ti ions is critical to the ferroelectric behavior, because the spontaneous polarization is reversible upon exposure to external electric fields is mainly caused by Ti displacement [10]. Thus, $BaTiO_3$ is a suitable material for testing the efficacy of the determination of atomic perturbations caused by external fields.

The electronic properties also play an important role in the ferroelectricity in $BaTiO_3$. Although the electric polarization can be explained qualitatively by the Ti displacement, it is insufficient to describe the magnitude of the electric polarization only by the atomic structure. Since there are covalent bonds such as Ti–O hybridization, the electric polarization is underestimated by using a simple point-charge model, where all atoms are completely ionic. Hence, it is necessary to probe electronic states and the atomic structure for the investigation of ferroelectric/dielectric behaviors in the $BaTiO_3$ system.

X-ray absorption spectroscopy (XAS) is a powerful tool to obtain information on the electronic states and local atomic structure around a specific element. XAS spectrum is commonly divided into two parts: X-ray absorption near edge structure (XANES) and extended X-ray absorption fine structure (EXAFS). The XANES region is sensitive to the electronic states, whereas the EXAFS region mainly contains local structural information. In many cases, these two parts have been analyzed individually for practical reasons.

The recent development of theoretical analysis might open new possibilities for integration of XANES and EXAFS results in a unified model. Reverse Monte Carlo (RMC) techniques are one of the advanced data analysis approaches to improve the amount of structural information that can be extracted from experimental EXAFS spectra. RMC provides a natural way to apply static and dynamic disorder effects into the structural model because

EXAFS signals are results as averaged over a number of atomic configurations, in each of which all atoms are slightly displaced from their equilibrium positions. Obtained structural models can be directly used for theoretical XANES calculations. In this thesis, a unified interpretation of EXAFS and XANES spectra for a prototypical ferroelectric $BaTiO_3$ is provided by this methodology.

1.2 Aim of this work

The aim of this study is to investigate the electronic states and local structure in $BaTiO_3$ using XAS techniques. In addition, the relationship between these two factors and ferroelectric properties are to be explained. The objectives of the study are:

- to measure electric-field dependent XAS spectra at Ba K-edge and Ti K-edge in $BaTiO_3$;
- to analyze experimental XAS spectra using modern theoretical approaches including *ab initio* calculations and RMC refinements;
- to estimate the local Ti displacement quantitatively by the combination of XANES and EXAFS results;
- to understand responses of the electronic states and local structure in $BaTiO_3$ under electric fields.

Chapter 2

Physical properties of $BaTiO_3$

2.1 Ferroelectricity

Generally, functional materials are classified by means of electric conductivity: a conductor such as a metal with high electric conductivity, and an insulator such as a dielectric with low conductivity. When an electric field is applied to a dielectric material, the electric current does not flow through the material due to the absence of free electrons, unlike a metal. Although electrons are bound around atoms or molecules in a dielectric material, electrons are slightly shifted from their equilibrium positions under applied electric fields, causing dielectric polarization. This electric polarization reduces the electric fields within the material.

A ferroelectric material is one of the dielectric materials and has an electric polarization, which exists even without external electric fields. This permanent electric polarization is called spontaneous polarization. The direction of the spontaneous polarization can be switched by applying electric fields beyond a certain magnitude of electric fields, so-called the coercive electric field E_c. Thus, a ferroelectric material shows an open loop in polarization-electric field (P–E) measurements, as shown in Fig. 2.1.

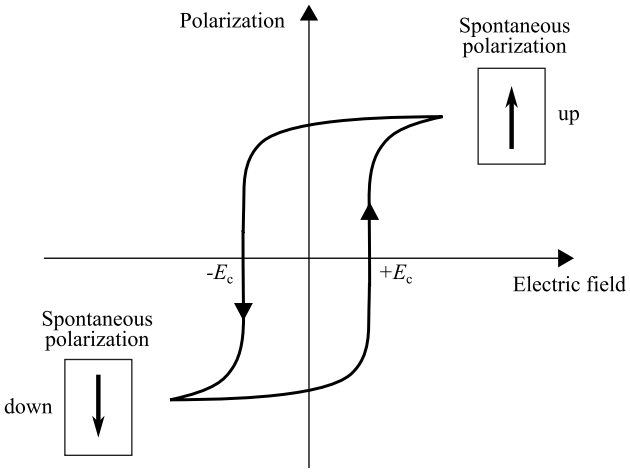

Fig. 2.1: Schematic diagram of P–E hysteresis loop in a ferroelectric material.

$BaTiO_3$ is one of the most famous ferroelectric materials, discovered in the 1940s [11, 12, 13]. The ferroelectric properties of $BaTiO_3$ have been widely studied because of its simple crystal structure and many practical applications for electronic devices. The details of the crystal structure are described in the following section.

2.2 Crystal structure

Fig. 2.2 shows a crystal structure of $BaTiO_3$. $BaTiO_3$ is a perovskite oxide, represented as the chemical formula of ABO_3, where A and B are two cations. The ideal cubic-symmetry perovskite structure has the B-site ion in 6-fold coordination, surrounded by an octahedron of oxygen atoms.

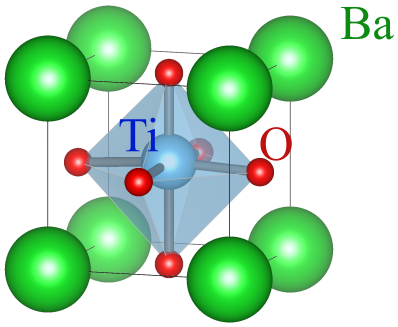

Fig. 2.2: Crystal structure of $BaTiO_3$ at room temperature.

Temperature dependence of lattice structure

A bulk $BaTiO_3$ material exhibits phase transitions with temperature. Fig. 2.3 shows the temperature-dependent lattice constants of $BaTiO_3$. $BaTiO_3$ is in a cubic phase at high temperature above the Curie temperature. This structure is centrosymmetric with no existence of spontaneous polarization. As the temperature is lowered, it goes through three phase transitions to different ferroelectric phases. The cubic-tetragonal phase transition, i.e., paraelectric to ferroelectric transition, is occurred at around 400 K. When the temperature is around 280 K, $BaTiO_3$ shows the tetragonal-orthorhombic phase transition. Further, an orthorhombic-rhombohedral phase transition occurs below around 180 K.

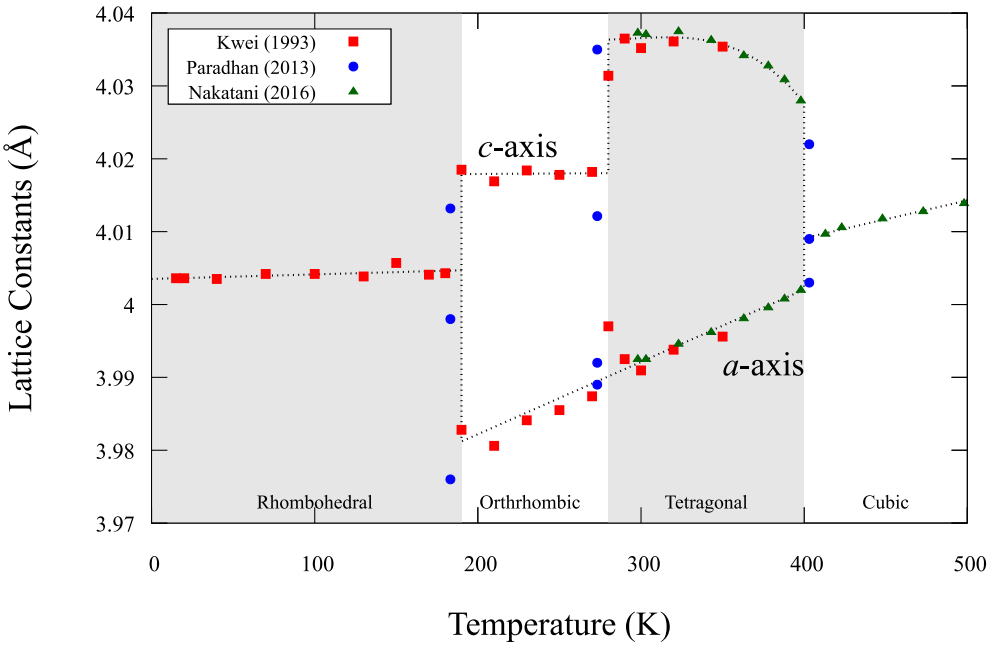

Fig. 2.3: Temperature dependence of the crystal structure of $BaTiO_3$, determined by diffraction studies [14, 15, 16].

The phase transitions are accompanied by drastic changes in ferroelectric properties, such as the magnitude of the spontaneous polarization, as can be seen in Fig. 2.4. Three ferroelectric phases have different small distortions from the cubic symmetry. The lattice distortions in the tetragonal, orthorhombic, and rhombohedral phase can be regarded as expansions of the cubic unit cell along [001], [011], and [111] directions, respectively. These distortions result in displacements of Ti atoms from the center of TiO_6 octahedra along these directions. These Ti off-center displacements primarily

give rise to the spontaneous polarization.

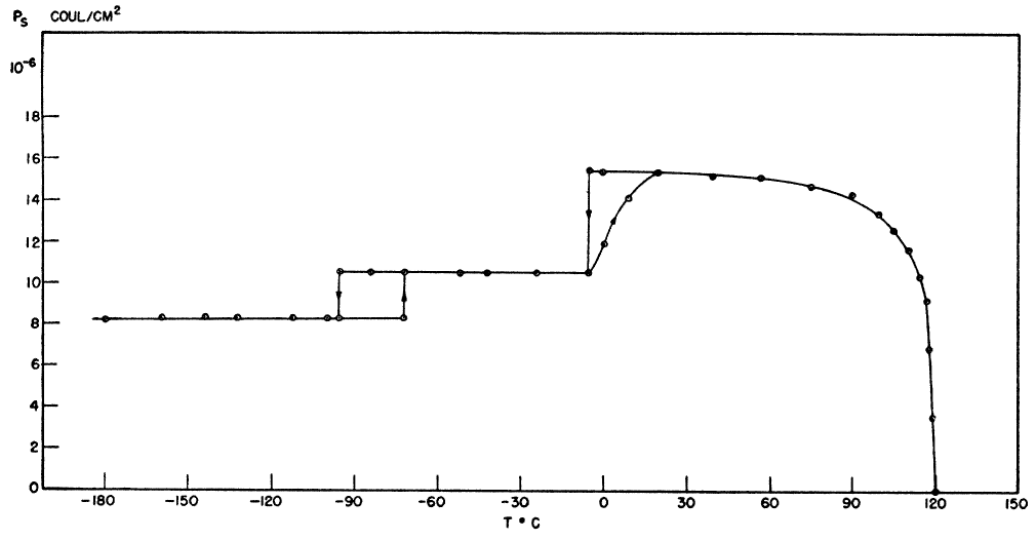

Fig. 2.4: Temperature dependence of the spontaneous polarization of $BaTiO_3$ along the [001] direction [17].

Electric-field dependence of lattice structure

The reversible polarization in $BaTiO_3$ indicates variations of the Ti displacements under applied electric fields. Although it is insufficient to experimentally analyze the Ti displacements under electric fields, the lattice distortions induced by applied electric fields have been observed in the previous studies [18, 19]. Fig. 2.5a and b show the lattice constants under static and dynamical electric fields, respectively. In both cases, the c/a ratio increases as the magnitude of applied electric fields increases. Because of these elongations along the [001] direction, one can expect an enhancement in the Ti displacements. In this study, the Ti displacements under electric fields were investigated using X-ray absorption techniques, as described later in Chapter 5 and Chapter 6.

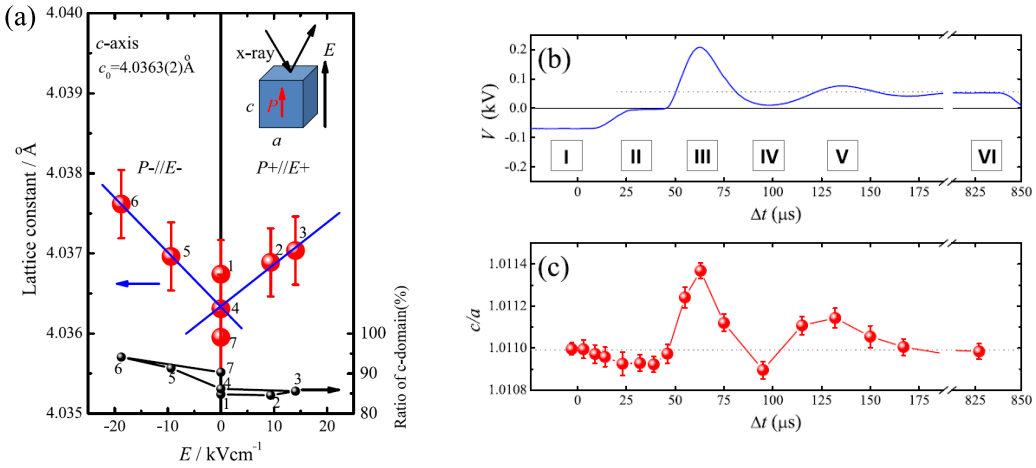

Fig. 2.5: Lattice constants of $BaTiO_3$ under applied electric fields. The left and right panels show the lattice distortions under static and dynamic electric fields, respectively. (a) The lattice consists c under static electric fields [18]. (b) The applied voltage to $BaTiO_3$. (c) The c/a ratio under applied electric fields [19].

2.3 Electronic states

As mentioned in the previous section, the spontaneous polarization in $BaTiO_3$ can be primarily explained by the Ti displacements relative to the center of TiO_6 octahedra. The polarization direction is simply estimated using atomic positions. In the theory of electrostatics, the electric dipole moment $\vec{p}$ in a collection of point charges is defined as

$$\vec{p} = \sum_i Q_i \vec{r}_i, \tag{2.1}$$

where Q_i and $\vec{r}_i$ are the charge and position of the particle i, respectively. This expression can be straightforwardly extended for the case of a continuous charge density $\rho(\vec{r})$:

$$\vec{p} = \int \rho(\vec{r})\vec{r}\ d\vec{r}. \tag{2.2}$$

As can be revealed from Eq. (2.1), the direction of the spontaneous polarization is consistent with the direction of the Ti displacement.

However, it is insufficient to describe the magnitude of the polarization only by the atomic positions. The magnitude is underestimated by an ionic model consisting of ions with nominal charges: Ba^{2+}, Ti^{4+}, and O^{2-}. This underestimation indicates the importance of electronic properties including

covalent bonds in materials. The presence of covalent bonds induces charge transfers between constituent atoms, exhibiting the charge density $\rho(\vec{r})$ away from the ionic model.

The existence of the covalency in $BaTiO_3$ has been verified by experimental and theoretical studies. Fig. 2.6 shows the charge density distributions obtained using the maximum entropy method for the X-ray diffraction [20]. It is clear to observe the covalent bond between Ti and O. This Ti–O covalency is also supported by the theoretical calculations by Cohen *et al.*, which has predicted the presence of Ti $3d$–O $2p$ hybridization [21, 22]. If the Ti–O hybridization is inhibited, the cubic phase is most stable [23]. Therefore, these experimental and theoretical results demonstrate the significance of electronic states for understanding the ferroelectricity.

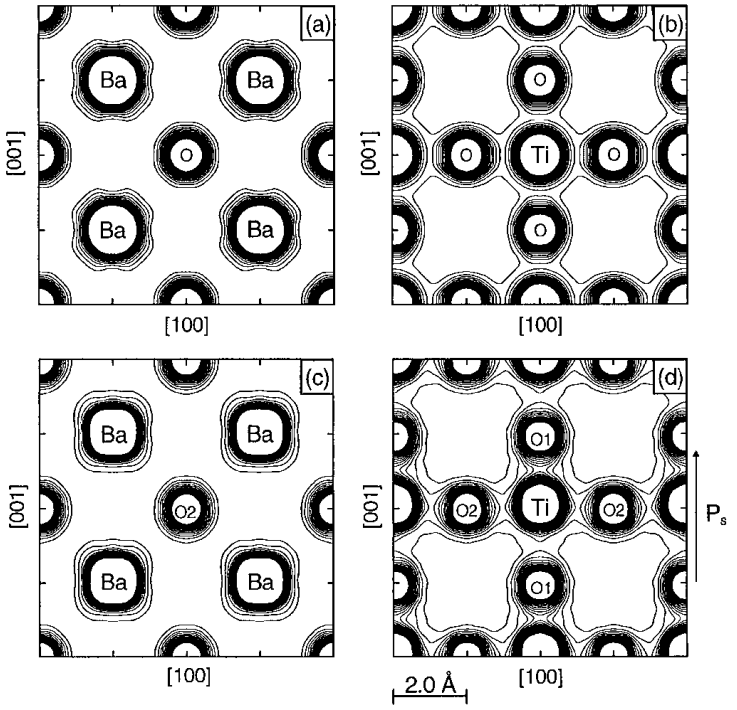

Fig. 2.6: Charge-density distributions of $BaTiO_3$ in (a) and (b) cubic phase at 573 K, (c) and (d) tetragonal phase at 300 K. The left and right panels show the Ba–O plane and the Ti–O plane, respectively. These results were obtained from X-ray diffraction measurements [20].

Because of the covalency, the nominal charges are less able or no longer able to reflect ferroelectric features. Instead, the Born effective charge is a useful quantity taking account of the chemical bonding. Provided that the polarization varies by $\partial\vec{P}$ when the ion cores move by $\partial\vec{u}$, the Born effective

charge Z^* can be represented by

$$\partial \vec{P} = Z^*(\vec{u})\partial \vec{u}. \tag{2.3}$$

$Z^*(\vec{u})$ is a dynamical quantity in distinct from the static charge like Q in Eq. (2.1). In general, the Born effective charge is a tensor. When the ion moves in direction i, the polarization in the other direction j can change. Thus, the Born effective charge Z^*_{ij} is defined as

$$Z^*_{ij} = \frac{\partial P_i}{\partial u_j}. \tag{2.4}$$

Fig. 2.7 shows schematic representations of two cases with different effective charges. As presented in Fig. 2.7a, the effective charge is close to the nominal charge when the electrons move by the same amount as the displacement of ionic cores. On the other hand, in the case as shown in Fig. 2.7b, the electrons shifted to the left as the positive cation moves to the right. The contributions of these electrons to the polarization are larger than the nominal charges, indicating the large Born effective charge.

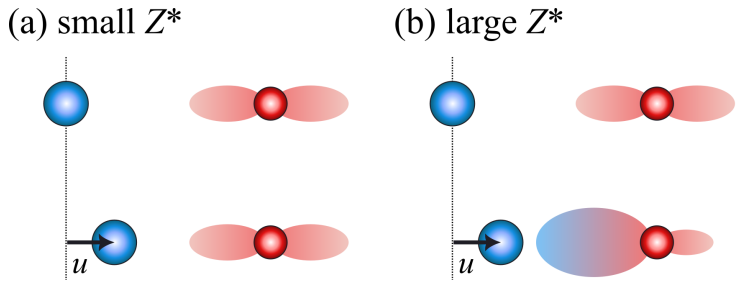

Fig. 2.7: Concept of Born effective charges. (a) the Born effective charge is close to the nominal value when electrons move by the same amount as ion cores. (b) the Born effective charge is large when electrons move in different amounts from ion cores.

The Born effective charges tend to be larger than nominal charges for materials that are ferroelectric or close to ferroelectric phases. In $BaTiO_3$, the anomalous large effective charges have been reported in various theoretical calculations [24, 25, 26, 27]. For instance, Ghosez *et al.* calculated the Born effective charges in $BaTiO_3$ using the framework of the density functional formalism within the local density approximation [25]. While the nominal charge of Ti is +4, the obtained Born effective charge is +7.25, indicating the large contributions of the Ti displacement to the polarization.

Ghosez *et al.* also identified the contributions of each electronic band structure to the effective charges [26]. It was revealed that the anomalous

charge of Ti essentially comes from the O $2p$ (+2.86). This O contribution corresponds to the O $2p$–Ti $3d$ hybridization, producing a charge transfer from O to Ti. Moreover, the non-negligible contributions of Ti $3p$, O $2p$, and Ba $5p$ bands are observed. These features suggest the existence of other hybridizations involving Ba. The Born effective charge of Ba was calculated to be +2.77, larger than the nominal value +2. The anomalous effective charge (+0.77) is smaller than that of Ti (+3.25) because Ba has more ionic character than Ti, as already seen in Fig. 2.6. However, the large anomalous charges of the O $2s$ and $2p$ are +0.73 and +1.50, respectively. They are mainly compensated by Ba $5s$ (−0.11) and $5p$ (−1.38) contributions. This result predicts that there are dynamic changes in the Ba–O hybridization as well as the Ti–O hybridization.

It should be emphasized that large contributions to effective charges are not related to strong hybridizations but to the rate of changes in these hybridizations when atoms move. That is, the Ba–O hybridization is much weaker than the Ti–O hybridization, however, large anomalous contributions of Ba and O are produced by the high sensitivity of the relatively weak covalency under atomic displacements. Therefore, it is essential to observe the electronic states with conditions where atomic displacements occur. Because of the anomalous large effective charges of Ti and Ba, one can expect the enhancement in orbital hybridizations under applied electric fields. In this study, the responses of Ba–O and Ti–O hybridization under electric fields were investigated using XANES spectra, as described later in Chapter 4.

2.4 Local structure

It is doubtless that the macroscopic spontaneous polarization in $BaTiO_3$ is primarily dominated by the average crystal structure. However, several aspects of local atomic displacements and phase transition mechanisms still remain uncertain. Previous reports state two phase-transition mechanisms: displacive and order-disorder types. These two types propose different local structures, which exhibit the same average atomic structure as mentioned in Section 2.2.

In a displacive model [10, 28, 29], the local structure is equal or close to the average structure. The long-range ferroelectric distortion arises from the concerted off-centering of Ti atoms within TiO_6 octahedra [28]. This Ti off-center displacement disappears in a paraelectric phase, where Ti atoms are located in the center of TiO_6 octahedra. The phase transition mechanisms can be explained by anharmonic lattice dynamics. A ferroelectric phase occurs because a certain normal mode of vibration becomes unstable

around the phase transition temperature. This unstable mode is called a soft mode, resulting in static atomic displacements. The eigenvector of the soft mode corresponds to the crystal structure in the low-temperature ferroelectric phase. Cochran theoretically demonstrated the instability of transverse optic modes [29].

Order-disorder type is a well-known concept of a statistical approach, represented by the Ising model. Fig. 2.8 shows schematic diagrams of the order-disorder (eight-site) model. In contrast to the displacive type, even the paraelectric cubic phase exhibits local Ti off-center displacements along ⟨111⟩ directions. According to a classical model, Ti atoms are randomly distributed among the eight split sites. Hence, the average position of Ti atoms is on the center of the lattice in the cubic phase. The tetragonal, orthorhombic, and rhombohedral phase has four, two, and only one possible position for the off-centered Ti atoms, respectively. Note that the existence of short-range orders between neighboring atoms is a key to phase transitions. If distributions of Ti atoms are completely randomized without short-range orders, a transition entropy is inappropriate [30]. Takahasi and Comes *et al.* proposed local order effects in disorder phases, where nanometer-scale structures with off-centered Ti atoms exist [31, 32].

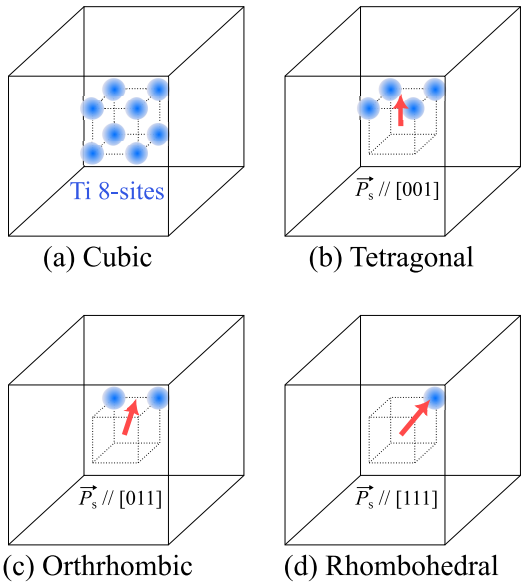

Fig. 2.8: Concept of order-disorder (eight-site) model. The probability of Ti atoms varies in (a) cubic, (b) tetragonal, (c) orthorhombic, and (d) rhombohedral phases. For simplicity, unit cells are described as pseudo-cubic. The average spontaneous polarizations $\vec{P}_s$ are represented as red arrows in three ferroelectric phases.

It is difficult to examine the displacive character or order-disorder character distinctly, because there is a lot of experimental evidence for both two types of phase transitions. Inelastic neutron scattering [33, 34] and Raman measurements [35] have revealed the softening of a transverse optic phonon, supporting the displacive phase transitions. On the other hand, the existence of an order-disorder character has been reported by various experiments [36, 37, 38], such as diffuse scattering [32, 39] and convergent-beam electron diffraction measurements [40, 41]. Therefore, the phase transition of $BaTiO_3$ has been understood as the coexistence of both displacive and order-disorder characters [42, 43, 44].

This study also supports the coexistence behavior by investigating the local Ti displacements under electric fields. In contrast to a simple displacive model, the obtained Ti displacements indicate the existence of $\langle 111 \rangle$ components along with the enhancement in the magnitude of Ti displacements. The structural model under applied electric fields is described later in Chapter 6.

Chapter 3

X-ray absorption spectroscopy (XAS)

3.1 General aspects of XAS spectrum

X-rays are electromagnetic waves with a wavelength in the range of 0.01-10 nm, corresponding to the energy from 0.1-100 keV. The energy of an X-ray is high enough to excite an electron in a core level such as K, L, or M shell. Such a photoelectric X-ray absorption process provides various microscopic information including the binding energy of electrons and the local environment around an atom.

X-ray absorption spectroscopy (XAS) is an experimental method for measuring the energy (E) dependence of absorption coefficient $\mu(E)$ as described in Eq. (3.1).

$$I(E) = I_0(E)e^{-\mu(E)x}, \tag{3.1}$$

where $I(E)$ and $I_0(E)$ are intensities of transmitted and incident X-ray, respectively, and x is the thickness of a material.

Schematic energy dependence of X-ray absorption coefficient is described in Fig. 3.1. Although $\mu(E)$ decreases as X-ray energy E increases generally, there are rapid increases in the absorption at specific energies, the so-called absorption edge. The energies of absorption edges are characteristics of an element because absorption edges occur when the incident X-ray energy is equal to the binding energy of an electron. Therefore, it is possible to select the element to probe by choosing the X-ray energy to the desired absorption edge.

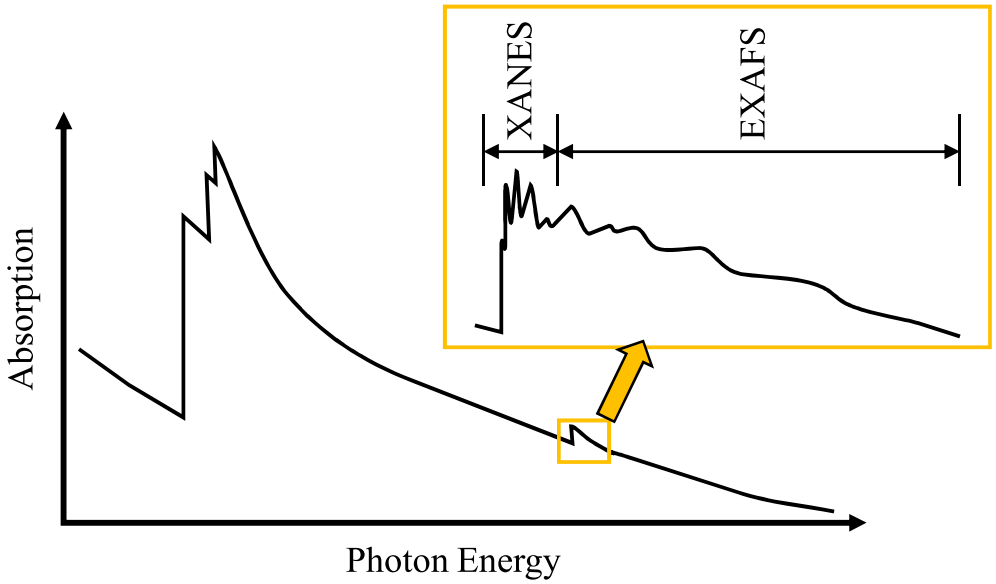

Fig. 3.1: Schematic view of X-ray absorption coefficient.

The XAS spectrum is usually divided into two regions: X-ray absorption near edge structure (XANES) and extended X-ray absorption fine structure (EXAFS). The XANES part is located around the absorption edge up to ∼50 eV and the EXAFS part extends up to thousands of electron volts beyond the absorption edge. Although the physical origin of both features is the same, analytical treatments are different between the two regions because some approximations can be applied to the EXAFS part of the spectrum.

3.2 X-ray absorption near edge structure (XANES)

The XANES part is mainly due to the direct transition of an electron from core-level states to unoccupied states. The density of unoccupied states is sensitive to the local environment around the absorbing atom such as the local symmetry of the probed element and the oxidation state.

An example of the Ti K-edge X-ray absorption spectra of various titanates is shown in Fig. 3.2. The absorption edge corresponds to the excitation of the 1s electron to the unoccupied 4p states of Ti atoms. As can be seen in the Fig. 3.2, the energy positions of absorption edges are different when the oxidation states of Ti are different; The absorption edge of Ti^{2+}, Ti^{3+}, and Ti^{4+} are located at 4975, 4979, and 4982 eV, respectively. Therefore, the XANES reflects the local electronic states of the absorbing element.

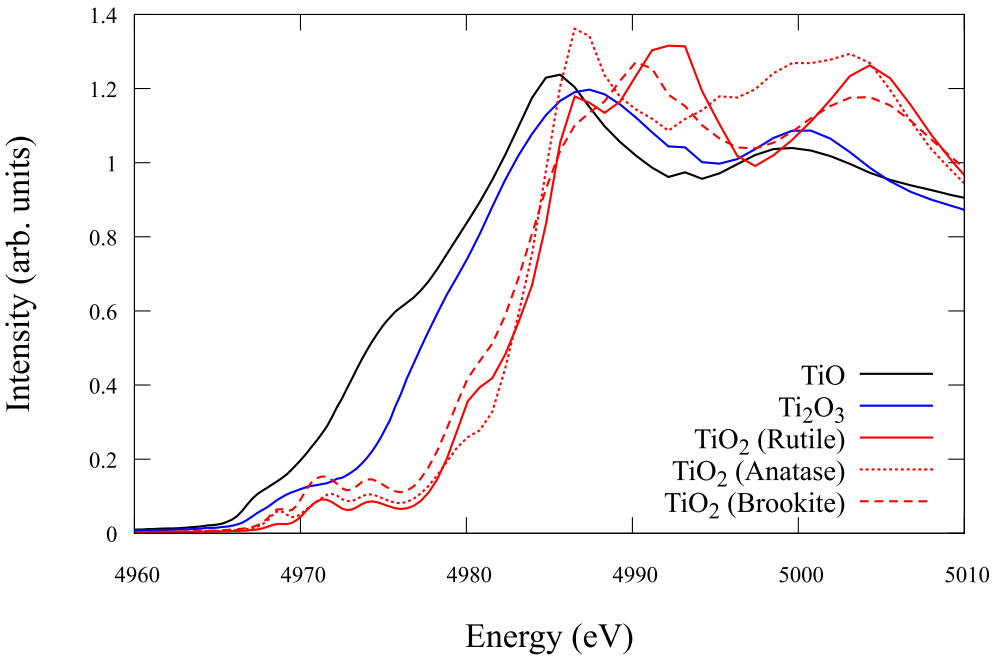

Fig. 3.2: Ti K-edge XANES spectra for various titanates at room temperature.

3.2.1 XANES data analysis

Fitting and modeling for XANES features can be challenging because there are a tremendous number of scattering events due to the large mean-free path of the photoelectron. Therefore, XANES features are commonly utilized as a fingerprint. The XANES spectrum for the investigated material is compared with some references with well-known atomic and electronic structures.

For instance, linear combination analysis is a semi-quantitative method. In this method, the investigated spectrum is fitted by a linear combination of reference spectra. It is a useful technique to quantify the relative amount of chemical species in mixtures and compounds, where the absorber atoms are in different local environments or chemical states.

The theoretical calculation for XANES spectra has been significantly developed over the past few decades. It is possible to simulate XANES spectra for a given structure model within *ab initio* calculations, implemented in calculational packages such as FEFF [45] and FDMNES [46, 47]. This *ab initio* XANES calculation has strongly promoted the development of advanced XANES analysis including machine learning for extracting structural parameters from XANES features. In this thesis, the interpretation of Ti K-edge XANES spectra was combined with EXAFS results through *ab initio*

XANES calculations.

3.3 X-ray extended absorption fine structure (EXAFS)

The EXAFS part is mainly due to the interference between the excited photoelectron and the photoelectron waves scattered by atoms surrounding the absorbing atom. The effect of the interference can be extracted by subtracting the absorption coefficient $\mu_0(E)$ of an isolated atom as described in Eq. (3.2) or presented in Fig. 3.3.

$$\chi(E) = \frac{\mu(E) - \mu_0(E)}{\mu_0(E)}. \tag{3.2}$$

The energy of EXAFS oscillation $\chi(E)$ is relative to the electron binding energy E_0, where the kinetic energy of the photoelectron is zero. It is common to convert the energy to the wave number k of the photoelectron using the relationship:

$$k = \sqrt{\frac{2m_e}{\hbar^2}(E - E_0)}, \tag{3.3}$$

where m_e is the mass of the electron and $\hbar = h/2\pi$ is the reduced Plank constant.

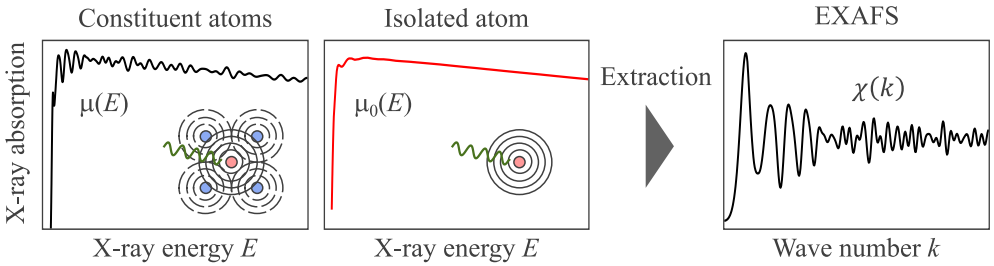

Fig. 3.3: Schematic diagram on the extraction of the EXAFS oscillation $\chi(E)$.

This photoelectron scattering process contains information on the local atomic structure around the absorbing atom such as coordination numbers, atomic distances, and their variations including thermal vibrations. An example of the temperature dependence of the Ba K-edge EXAFS oscillation is provided in Fig. 3.4. The amplitude of EXAFS oscillation decreases as temperature increases, indicating the large thermal vibrations with high temperature.

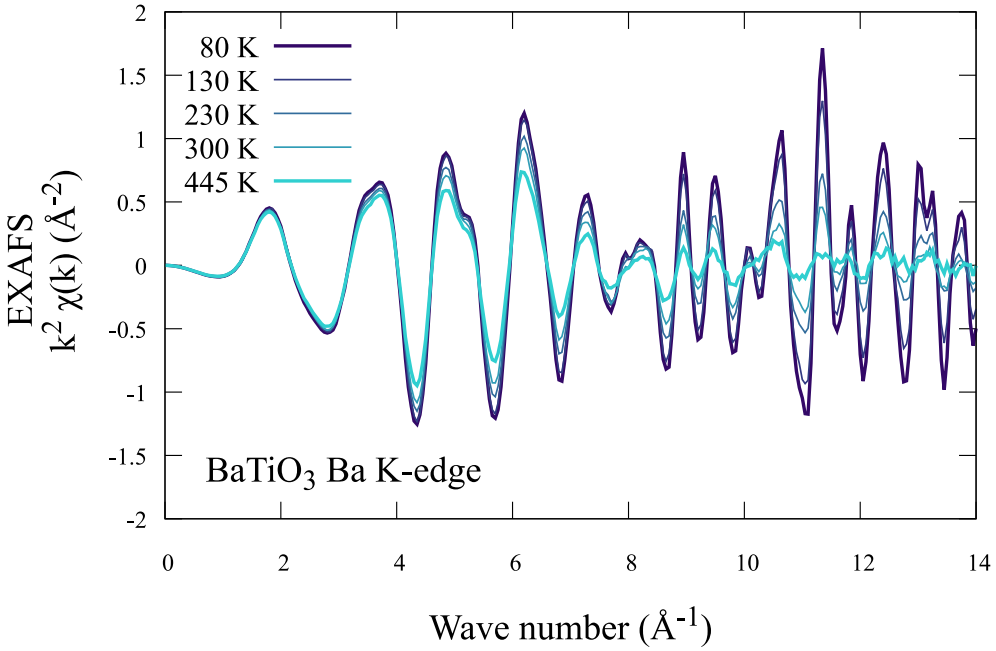

Fig. 3.4: Temperature dependence of EXAFS oscillation for a powder $BaTiO_3$.

3.3.1 EXAFS data analysis

The conventional EXAFS analysis is based on a nonlinear least-square curve fitting of experimental spectra. Unlike the XANES part, some important approximations can be applied to the EXAFS part of spectra. An EXAFS spectrum can be described within the multiple scattering approximation as a sum of contributions of photoelectron scattering paths:

$$\chi(k) = S_0^2 \sum_i \frac{N_i}{kR_i^2} F_i(k) \sin\left[2kR_i + \phi_i(k)\right] e^{-2k^2\sigma_i^2}, \tag{3.4}$$

where S_0^2 is an amplitude reduction factor due to the multi-electron effects, N_i is the number (degeneracy) of scattering paths, R_i is the half length of the scattering path, $F_i(k)$ is the back-scattering amplitude of the photoelectron, $\phi_i(k)$ is a phase shift, and σ_i^2 is called the Debye-Waller factor or the mean-square relative displacement (MSRD). The structural parameters can be obtained by using this EXAFS equation.

The $F_i(k)$ and $\phi_i(k)$ are non-structural functions and depend on the type of neighboring atoms around the absorber. These parameters are calculated theoretically for each scattering path or extracted from a reference spectrum.

The R_i, N_i, and σ^2 are structural factors. The R_i and N_i equal to the interatomic distance and the coordination number, respectively, when the scattering process is a single scattering. The σ_i^2 is the parameter for disorder effects, reducing EXAFS amplitude. It can be described as thermal atomic vibrations σ_T^2 and static disorder σ_{static}^2:

$$\sigma^2 = \sigma_T^2 + \sigma_{static}^2. \tag{3.5}$$

It is difficult to obtain the correct structural parameters when a large disorder exists in a material and atomic distances cannot be approximated with a Gaussian distribution. Cumulant decomposition is a mathematical model for the analysis of anharmonic effects. Reverse Monte Carlo (RMC) refinements, as described in the next section, are also advantageous analyses for disorder effects.

3.3.2 Reverse Monte Carlo (RMC) refinements

Reverse Monte Carlo (RMC) method is an iterative calculation approach for atomic structural optimization in a random process. RMC is not limited to analyzing EXAFS signals and can be applied to any other experimental data containing structural information. The first RMC refinement was introduced to diffuse scattering measurements by McGreevy *et al.* in 1980s [48]. Although the RMC method was originally developed for building models of disordered materials such as amorphous and liquids, this technique has also been applied to crystalline and nano-crystalline materials.

The RMC calculation starts with an arbitrary initial atomic configuration. The initial structure for a crystalline material is usually a supercell, composed of several unit cells, constructed from an average structure obtained by diffraction measurements. The supercell size should be large enough to obtain theoretical spectra including structural information to be extracted. In the case of EXAFS analysis, the size should be larger than the longest distance of the scattering paths used in the fitting. Although a huge supercell provides good statistics, the computational time is too long for practical analysis. A finite supercell size may result in a calculational spectrum including surface-related effects. Periodic boundary conditions are sometimes applied to avoid surface-related effects.

The theoretical EXAFS spectrum corresponding to an atomic configuration is the average EXAFS over all absorbing atoms in the configuration. It is a natural way to apply static and dynamic disorder effects to the structural model. The absorbing atom is in an excited and unstable state after absorption events. The lifetime is the excited state is $\sim 10^{-15}$ s and shorter

than the time scale of thermal vibrations ($\sim 10^{-13}$ – 10^{-15} s). Thus, the position of all atoms does not change during the absorption process. It is possible to analyze disorder effects through each atomic displacement from the equilibrium position in the optimized atomic configuration.

The atomic configuration is optimized through each iteration process. At each iteration, a new atomic configuration is generated by randomly displacing atoms. Two theoretical EXAFS signals $\chi_{calc}^{old}(k)$ and $\chi_{calc}^{new}(k)$ are calculated from the old and new atomic configurations, respectively. The new atomic configuration is either accepted or discarded, depending on the agreement between the calculated and experimental spectra $\chi_{exp}(k)$ such as follows:

$$\xi = \frac{\|\chi_{calc}(k) - \chi_{exp}(k)\|^2}{\|\chi_{exp}(k)\|^2}. \tag{3.6}$$

The simplest way to reduce the residual is to accept the new atomic configuration when $\xi_{new} < \xi_{old}$, where ξ_{new} and ξ_{old} are the residuals corresponding to the new and previous atomic configurations, respectively. However, this simple method is hardly implemented in RMC calculations because it gets stuck in local minima.

Metropolis algorithm

The Metropolis algorithm is a common acceptance/rejection algorithm, based on the acceptance probability for a new state generated in an iteration process. If a random number r is less than the acceptance probability, the new state is accepted even when the residual becomes larger than the previous one:

When $\xi_{new} < \xi_{old}$, the new atomic configuration is accepted.

When $\xi_{new} > \xi_{old}$, the new atomic configuration is accepted, if

$$\exp\left[-\frac{\xi_{new} - \xi_{old}}{\Theta}\right] > r, \tag{3.7}$$

and discarded otherwise, where Θ is a scaling factor and is also called a "temperature" parameter.

It is required to set the Θ parameter appropriately for finding the global minimum. If the Θ is large, the system will fluctuate with a large amplitude. On the other hand, if the Θ is small, the system will get stuck in local minima. The Θ value should be proportional to the noise level of experimental data when the Θ is a fixed value.

Instead of using a fixed Θ value, an alternative solution is the so-called simulated annealing approach. In this approach, the Θ decreases slowly as

the iteration count increases. The RMC starts with a large Θ value to stimulate a fast approach to the global minimum. Then, Θ is reduced so that the fluctuations are suppressed and the acceptance probability is finally equal to zero. The simulated annealing scheme, implemented in RMC calculations reported in this thesis, resembles a Boltzmann annealing schedule. The acceptance probability p decreases linearly during RMC calculations. At the beginning of the calculation, all proposed atomic displacements are accepted, but the probability equals zero when the iteration number n is larger than a "Froze in" parameter n_{max}: $p(n) \propto 1 - n/n_{max}$.

Evolutionary algorithm (EA)

The evolutionary algorithm (EA) is a technique widely used for solving parameter optimization problems in computational science. The basic idea is to mimic genetic processes in ecosystems. A set of all parameters to be optimized (i.e., an atomic configuration) is regarded as an "individual" in EA. An ensemble is prepared for EA; it consists of many individuals (many atomic configurations) having different parameters. Some manipulations with this ensemble are performed during the EA process.

There are three manipulations applied in EA;

1. Selection
2. Crossover
3. Mutation

In the selection process, some individuals are picked up and used again for the next iteration, that is, 'good' atomic configurations are selected. An atomic configuration in better agreement with experimental data has a larger probability to get into the new ensemble. In the crossover process, parameters of two randomly selected individuals ("parents") are exchanged for obtaining new individuals ("children"). That is, some atoms of an atomic configuration are replaced with atoms of another atomic configuration. In the mutation process, all atoms in all atomic configurations are randomly displaced.

The EA provides significant efficiency in exploring the possible configuration space. Thus, the iteration count required for the convergence in calculations is reduced compared to the conventional RMC process in many cases. For instance, an RMC structural refinement with the EA using 64 individuals was converged more quickly than that without the EA, as shown in Fig. 3.5.

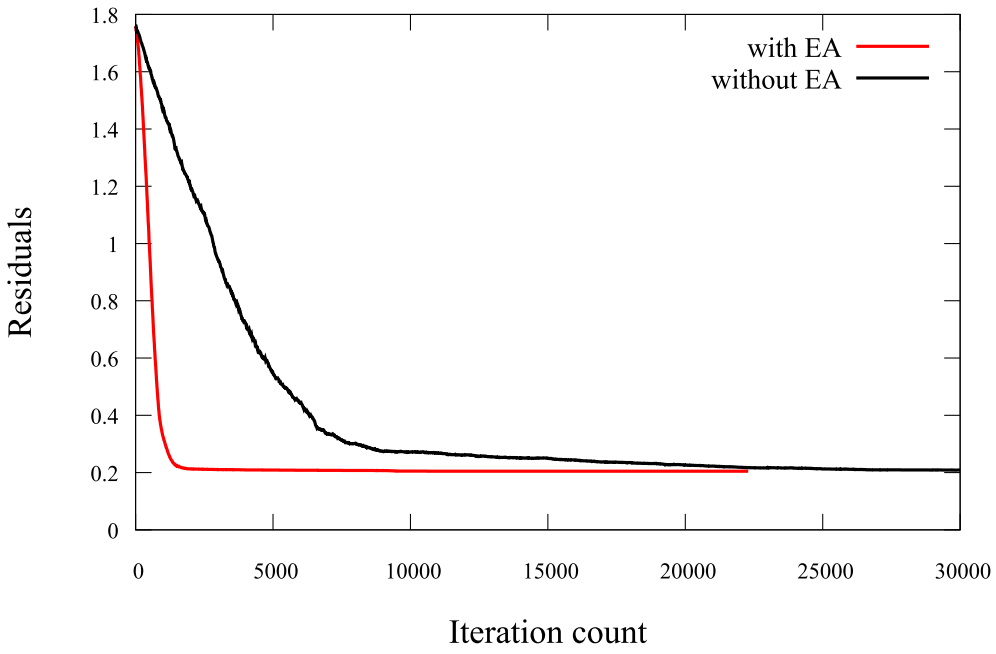

Fig. 3.5: Improvement in residuals between experimental and calculated EXAFS spectra through the RMC iterative process, with or without EA.

3.4 XAS experiment

3.4.1 Synchrotron radiation

A synchrotron radiation source is suitable for XAS measurements because it provides X-ray beams with high intensity in a broad range of energies. Synchrotron radiations are electromagnetic waves, generated by charged particles, i.e., electrons, with relativistic velocities (a speed close to the speed of light) in a circular path. Electrons are injected into a closed orbit, so-called a storage ring. The storage ring has straight sections alternating with curved sections. In curved sections, the trajectories of electrons are bent by magnetic fields. Insertion devices, such as undulator and wiggler, are arranged between these bending magnets for producing additional sources of X-rays. The generated X-rays are channeled down to experimental end stations known as beamlines, including a monochromator to select distinct X-ray energies for XAS measurements.

XAS measurements, reported in this thesis, were performed at two synchrotron radiation facilities: the Photon Factory of the High Energy Research Organization (KEK-PF) and SPring-8. KEK-PF is the first dedicated synchrotron light source in Japan, which supplies X-rays. The 2.5-GeV PF Ring

has been operated since 1982. Several improvements in accelerators have been made and resulted in a high-brilliant light source with the capability to perform experiments in material/biological science. SPring-8 is a large synchrotron radiation facility with an 8-GeV storage ring in Japan. This facility is designed especially for installing many insertion devices in a dedicated storage ring. It is available to use collimated X-ray beams ranging from the soft X-ray (300 eV) to the hard X-ray region (300 keV).

3.4.2 XAS measurement modes

There are three common methods to measure the amount of X-ray absorption by a target material as follows:

1. Transmission mode
2. Fluorescence mode
3. Electron-yield mode

In transmission mode, intensities of the incident and transmitted X-rays are measured. Absorption coefficient $\mu(E)$ for a sample is obtained by using Eq. (3.1):

$$\mu(E)x = \ln \frac{I_0}{I}, \tag{3.8}$$

where I_0 and I are the incident and transmitted intensities, respectively.

X-ray intensities are commonly measured by ion chambers. An ion chamber is filled with inactive gas such as N_2 and Ar. The X-rays ionize some of the gas and released electrons and ions. Applied electric fields across the ion chamber move these charged particles, resulting in a current that is proportional to the X-ray intensity.

In fluorescence mode, the X-ray absorption coefficient $\mu(E)$ is obtained by measuring the fluorescence intensity. X-ray absorption by a material occurs in the removal of an electron in an atom. This excited state with a vacancy in a core orbital is unstable, and an electron in a higher orbital intends to fill the core hole. In this process, an X-ray photon is emitted with an energy equal to the energy difference between two orbitals. The fluorescence intensity is proportional to the amount of X-ray absorption:

$$\mu(E) \propto \frac{I}{I_0}, \tag{3.9}$$

where I_0 and I are intensities of the incident and fluorescence X-ray, respectively.

An ion chamber detects X-rays with every energy, however, it is required in fluorescence mode to count photons with specific energies corresponding to fluorescence from the specified absorption edge. Other X-rays such as elastic scattering are undesirable backgrounds. A silicon drift detector (SDD) is one of the energy-dispersive X-ray detectors, commonly used for XAS measurement in fluorescence mode. SDD measures the energy of a photon by the amount of ionization produced in the detector material: high-purity silicon with a very low leakage current. Transversal fields generated by a series of ring electrodes causes charge carriers to drift to a collection electrode. In the SDD, the photon energy is determined by the detected charge amount because different ionization produces different charges.

In electron-yield mode, photoelectrons induced by the X-ray absorption are measured. The number of electrons, such as photoelectrons, Auger electrons, and secondary electrons, is proportional to the X-ray absorption intensity. Electrons near the surface of the sample can be emitted from a material because the mean free path of electrons is less than 100 nm in the soft X-ray region. Thus, electron-yield techniques are highly sensitive to the sample surface.

Chapter 4

Ti K-edge XANES for $BaTiO_3$ thin film

4.1 Introduction

In this chapter, the electronic states in $BaTiO_3$ under electric fields were investigated by Ti K-edge XANES measurements. The electronic states play an important role in ferroelectric behaviors as well as the crystal structure. Many previous literatures primarily focused on the crystal structure in ferroelectric materials because space-inversion symmetry is required to be broken for the occurrence of a spontaneous polarization. In the case of perovskite titanates, the Ti off-center displacement in the TiO_6 octahedra is a major cause of the spontaneous polarization [10, 49, 50, 51, 52, 53]. Electric polarizations are due to the dipole moment induced by Ti displacements, however, the magnitude of the spontaneous polarization is inconsistent with the polarization calculated with a simple-charge model, where all atoms are completely ionic and there is no covalent bond. It is necessary to include covalent bonds and dynamic charge effects such as the Born effective charge so that one can calculate dielectric properties precisely.

Cohen was the first to theoretically demonstrate the existence of Ti $3d$ and O $2p$ hybridization in ferroelectric $BaTiO_3$ and $PbTiO_3$ [21, 22]. Moreover, Pb $6s$ and O $2p$ hybridization also exists and contributes to the spontaneous polarization in $PbTiO_3$. These predictions were experimentally verified by Kuroiwa *et al.* via high-precision X-ray diffraction analysis, which revealed the electron density distribution [20]. Recently, Anspoks *et al.* reported the correlation effects of A-site ions in O and Ti based on the RMC method applied to EXAFS data [54]. Therefore, it is quite evident that orbital hybridization between constituent atoms is closely linked to the dielectric

properties of perovskite titanates.

Hence, direct observation of the electronic states under the applied electric fields is an appropriate approach to investigate the dielectric properties in ferroelectric materials. Here, time-resolved X-ray absorption spectroscopy (TR-XAS) was employed. Combined with the TR approach, XAS can be utilized for the investigation of the polarization reversal response of the atomic bonds in $BaTiO_3$. It was observed that intensities of the pre-edge e_g peak and shoulder structure just below the main absorption edge increase as the electric polarization increases, whereas that of the main edge decreases oppositely. This observation indicates that in addition to Ti $3d$–O $2p$ hybridization, a correlated effect of Ba ions on Ti electronic states also contributes to polarization reversal in $BaTiO_3$.

4.2 Experimental

4.2.1 Sample preparation

The schematic diagram of the sample composition is provided in Fig. 4.1. The sample is an epitaxial $BaTiO_3$(001) film with a thickness of 650 nm. It was prepared using pulsed laser deposition on a 0.5 mm-thick $(LaAlO_3)_{0.3}$-$(SrAl_{0.5}Ta_{0.5}O_3)_{0.7}$(001) substrate along with a 100 nm thick $SrRuO_3$(001) buffer layer, which also acted as the bottom electrode. The top electrode is a 50 nm-thick Pt with a diameter of 100 μm, evaporated on the $BaTiO_3$ film.

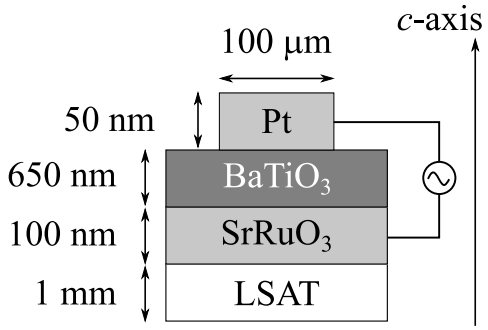

Fig. 4.1: Schematic diagram of the sample composition used for Ti K-edge XANES measurements under electric fields.

Film growth was verified via X-ray diffraction, as shown in Fig. 4.2. It was confirmed that all layers had a preferred (001) orientation normal to the surface of the film. The lattice constant c of the $BaTiO_3$ film was 4.136 Å, calculated from the (002) peak. This c-axis is longer than that of a standard powder ($c = 4.018$ Å) [55], indicating a compressive strain due to the lattice mismatch between the $BaTiO_3$ and substrate [56]. The preferred orientation of the c-axis is also reported in $BaTiO_3$ thin films with $SrTiO_3$ substrates, where a misfit strain is smaller than the sample in this study [57]. This result guarantees that the influence of a domain and the domain wall motion under electric fields are negligible in this case.

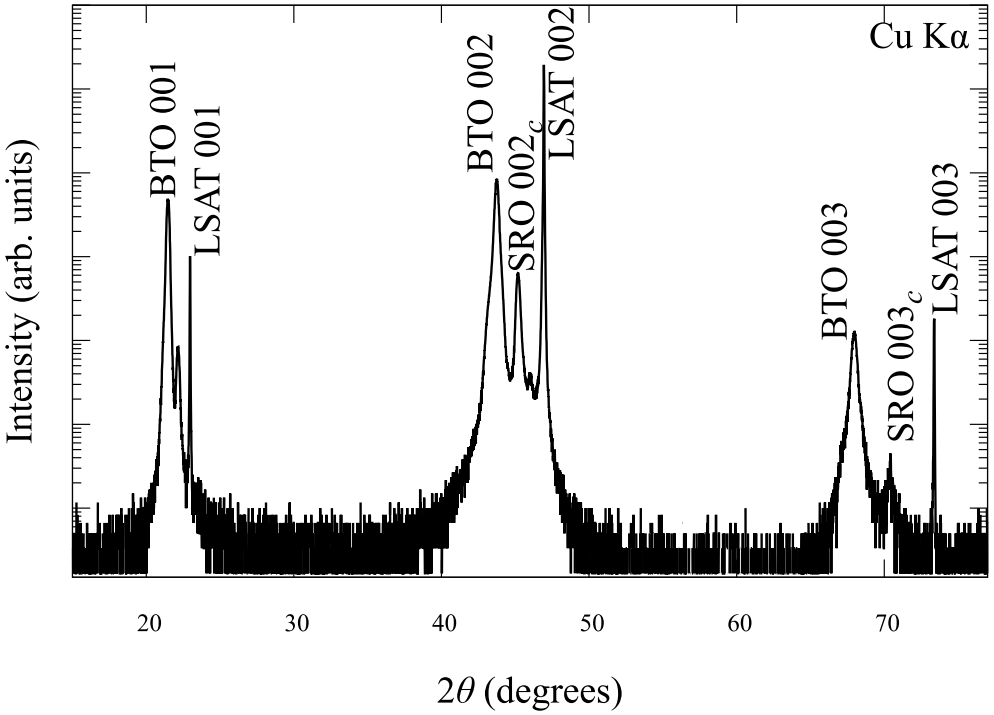

Fig. 4.2: X-ray diffraction of the $BaTiO_3$(001) thin film sample grown on a $SrRuO_3$(001)/$(LaAlO_3)_{0.3}$-$(SrAl_{0.5}Ta_{0.5}O_3)_{0.7}$(001) substrate.

The ferroelectricity was verified by measuring polarization-electric field (P–E) hysteresis using a ferroelectric tester (FCE-fast, Toyo Corporation, Japan) with a triangular electric field of 1 kHz. The P–E hysteresis loops are shown in Fig. 4.3. The open loops demonstrate the ferroelectricity in the $BaTiO_3$ thin film both before and after TR-XAS measurements. These loops are shifted in the positive electric-field direction indicating a preferred downward polarization [58, 59]. This effect is called an imprint effect due to the extrinsic interface effect, including the asymmetric properties of top and bottom electrodes [60].

Whereas the saturation polarization decreased, the magnitude of the negative coercive field increased after the XANES measurements. These observations might be attributed to the fatigue effect caused by domain pinning and microcracking [61]; however, the dielectric properties remain even after experiments because the hysteresis loop is closed as shown in Fig. 4.3, indicating low leakage current density. The currents at the maximum electric field before and after the XANES measurements were 1.1 μA and 1.2 μA, respectively. The difference is below the experimental error. Therefore, it does not produce any detectable change in the XANES spectra.

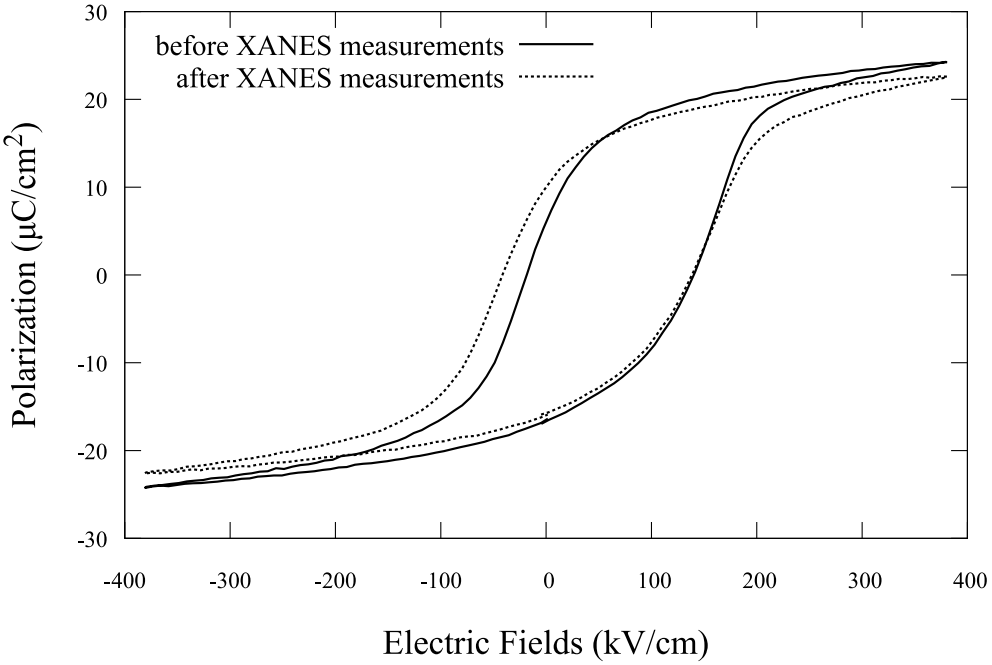

Fig. 4.3: $P-E$ hysteresis loop for the $BaTiO_3$ thin film before and after Ti K-edge XANES measurements.

4.2.2 Time-resolved XAS measurement system

A time-resolved X-ray absorption spectroscopy (TR-XAS) measurement is required for the direct observation of electronic states under the condition of polarization reversal. Among the several TR-XAS methods that have been developed previously, there are two common methods to measure time-resolved XAS spectra: pump-probed XAS and quick-scanning XAS.

The pump-probe method can achieve excellent time resolution with an order of femtosecond ($\sim 10^{-12}$ s) using two or more optical pulses with a time delay between them. The first pulse (pump) initiates the reaction, and the second pulse (probe) is used to observe the progress of the reaction after initiation. Despite the high time resolution, pump-probe methods are not compatible with conventional equipment because the equipment needs to synchronize with the synchrotron X-ray bunch modes. Moreover, this method can only be used to investigate reactions induced by optical pulses.

The quick-scanning XAS method is compatible with conventional XAS measurements. In this method, the monochromator rotates quickly for a reduction in the collection time for spectra; it usually takes minutes or seconds. Although this method is compatible with various sample conditions, it is difficult to achieve high time resolution.

A TR-XAS system has been introduced using Si drift detector (SDD) time stamps. There are two main advantages of the proposed system:

1. It is independent and transferable to other beamlines.

2. It is easily combined with various sample conditions, and the time resolution is in the sub-microsecond range.

This system is applied to ferroelectric materials under triangular AC electric fields, which is difficult to achieve using pump-probe methods.

TR-XAS system was realized using time stamp information based on the conventional step-scan method. Fig. 4.4 shows the block diagram of the signal processing system that is employed in this study. The detected X-rays were converted to digital signals using a digital signal processor (DSP; Techno-AP, APU101) with the addition of a time stamp for each signal. The internal time of the DSP was repeatedly reset to zero, using a clear pulse generated by a delayed pulse generator (SRS, DG645). Additionally, the same clear pulse was input into the wave generator as a trigger pulse, to apply external stimuli such as electric fields to the sample. These two clear pulses were used to synchronize the internal times of the DSP and applied fields. It is possible to assign a timing to the detected X-ray signals in response to the applied fields, thereby enabling TR measurements.

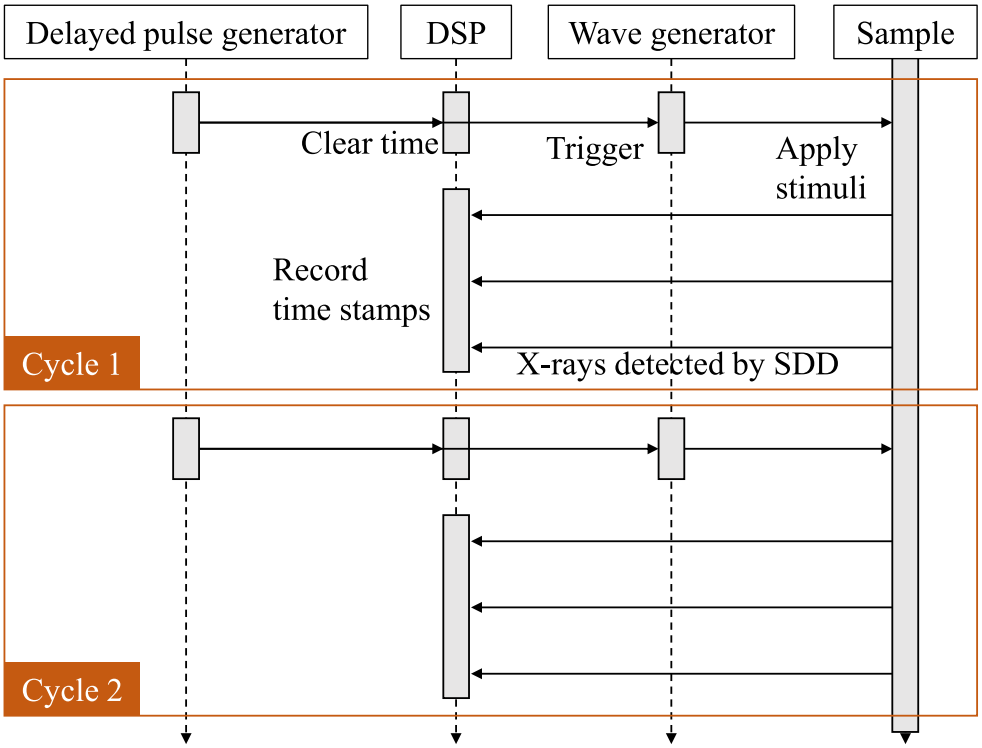

Fig. 4.4: Block diagram of the signal processing system employed.

Two types of waveform shaping filters were used to process X-ray signals, as shown in Fig. 4.5. In the slow mode filter, the signal height was acquired, which corresponds to the X-ray energy. In the fast mode filter, the time stamp was acquired when the signal arrived at the DSP. The time stamp corresponds to the X-ray detection time. The fast-mode signal returned to the baseline quickly enough to extract the time stamp accurately. The time stamp was recorded as the internal time in the DSP. By acquiring the processing time stamps appropriately for all detected signals, it is possible to investigate the time dependence of the X-ray intensity.

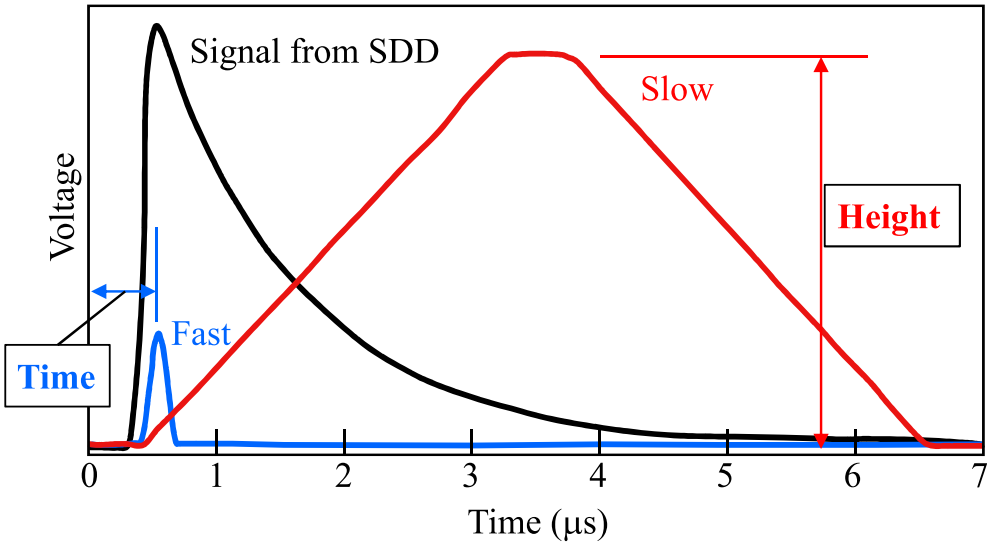

Fig. 4.5: Two types of waveform shaping filters (fast and slow mode) processed in the DSP.

The processing time in the fast-mode filtering should be analyzed for the precise determination of the X-ray detection time. If it takes non-negligible time, the time stamp is delayed for the processing time. The processing time was estimated using a test circuit, wherein the DG645 generates test pulses at a frequency of 50 kHz. Clear pulses that reset the internal time in the DSP are input at a frequency of 49.7 kHz, which has a slightly longer period than those of test pulses. If the processing time is sufficiently short, the detection time of a test pulse is zero. However, as shown in Fig. 4.6, test signals were detected at 530 and 540 ns, indicating that the processing time of the DSP is 530–540 ns. This time delay can be ignored in the case of microsecond TR measurements.

A few test signals at 20660 ns were also detected. It is assumed that the internal time in the DSP is not reset in rare cases, as the difference between 20660 ns and 540 ns is 20120 ns, which coincides with the period of 49.7 kHz. These inappropriate signals, with time stamps exceeding one cycle of clear pulses, can be discarded through data analysis.

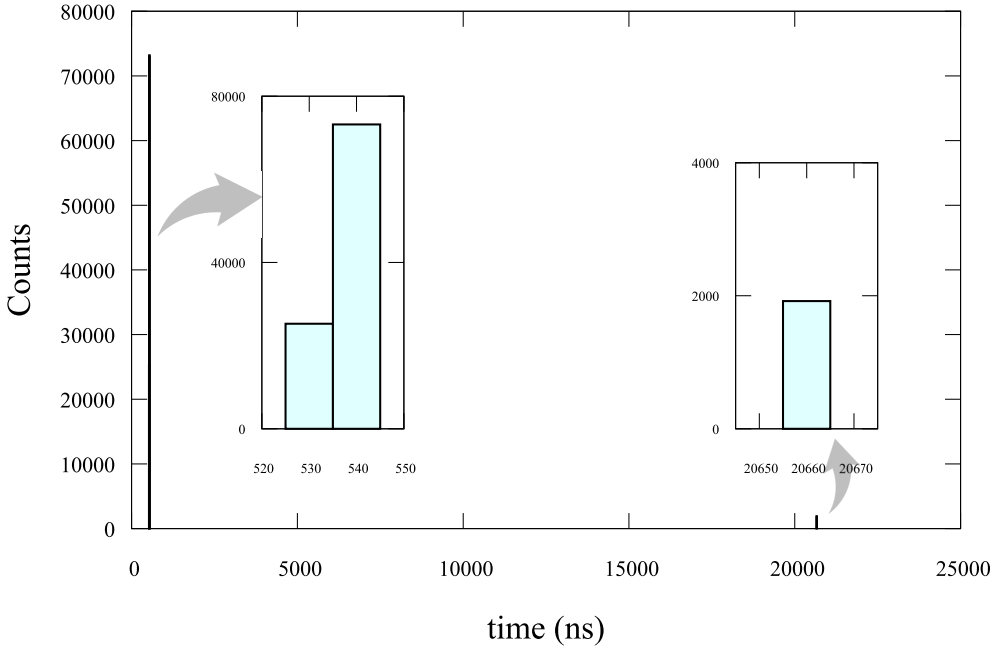

Fig. 4.6: Detection time distributions of test signals.

The time resolution of TR-XAS measurements depends on the performance of the DSP. The DSP used in this study records the time stamps in 10 ns steps, and test signals were detected at 530 and 540 ns, as can be seen in Fig. 4.6. Thus, the time resolution is approximately 20 ns.

4.2.3 Time-resolved XANES measurements

XANES experiments were performed on the beamline BL-15A1 equipment at the Photon Factory of the High Energy Research Organization (KEK-PF) using a Si (111) liquid-nitrogen-cooled double-crystal monochromator. The X-ray beam was focused to 20 μm (Horizontal) $\times$ 20 μm (Vertical) at the sample, which ensured the inclusion of the entire beam on a top electrode. Ti K-edge spectra were recorded in partial fluorescence yield mode using SDD. X-rays were incident on the top electrode of the film at an angle of 45° from the surface normal. Fig. 4.7 shows the energy distribution of the detected signals. Ti K_α fluorescence and elastic scattering were observed in this experiment. Signals only in the Ti K_α region are counted to measure partial fluorescence spectra.

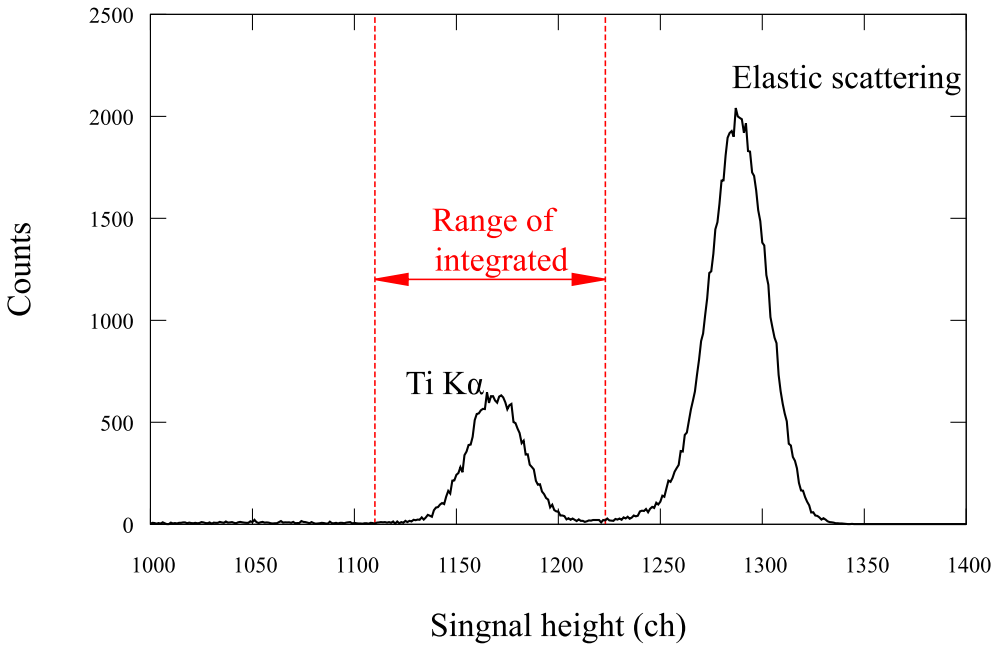

Fig. 4.7: Energy distribution at Ti-K edge of the $BaTiO_3$. The horizontal axis corresponds to the X-ray energy.

The internal time in the DSP was repeatedly reset to 0 every 3 ms using a clear pulse generated by DG645. In addition, the same clear pulse was also input into the wave generator as a trigger pulse to apply the electric field to the film. In particular, one cycle of the applied voltage consisted of a single triangular pulse (±25 V, 1 kHz) and null voltage for 2 ms. Using this cycle, it was possible to assign a timing to the detected X-ray signals in response to the applied voltage, thereby enabling TR measurements. Several scans were summed to obtain the final Ti K-edge spectra with sufficient statistics. Because TR-XAS measurements require a long duration—e.g., 8 hours for one spectral region— only three spectral features were focused on in this study: namely e_g peak, shoulder structure, and main peak.

4.3 Results and discussion

4.3.1 Ti K-edge XANES without electric fields

A non-TR Ti K-edge spectrum of the $BaTiO_3$ thin film is shown in Fig. 4.8, along with that of a standard $BaTiO_3$ powder as a reference. The absorption profile above a sharp main peak at 4985 eV corresponds to the density of states of the unoccupied Ti 4*p* states, whereas small features in a pre-edge region (4965–4975 eV) represent the Ti 3*d* states.

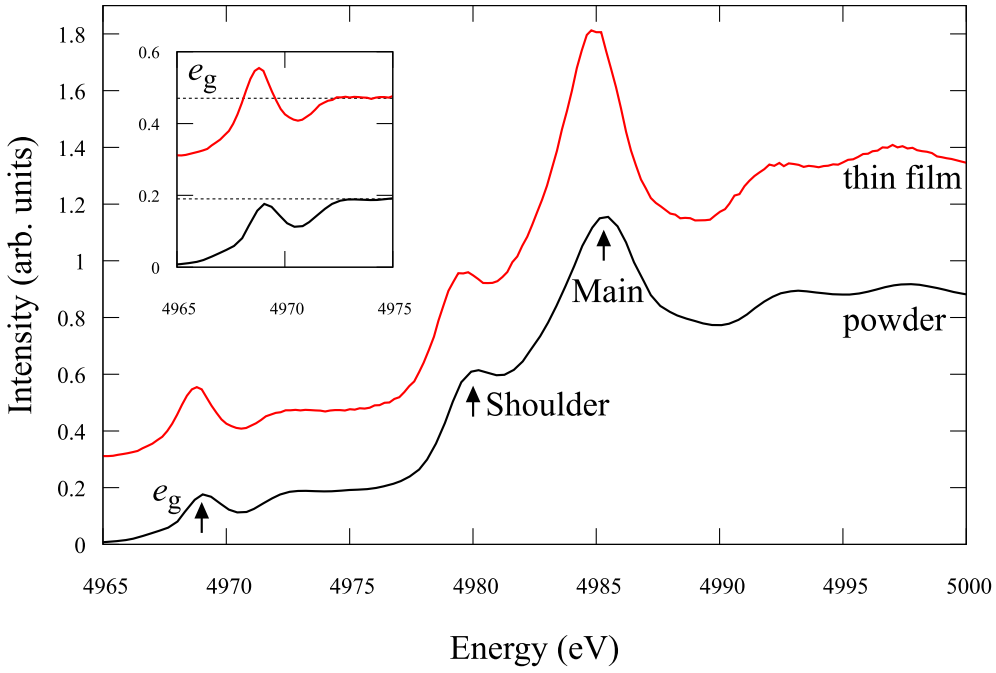

Fig. 4.8: Ti K-edge XANES spectra for the $BaTiO_3$ thin film and a standard powder at room temperature.

In the case of an octahedral symmetry, the five-fold degenerate 3*d* orbitals split into three-fold and two-fold degenerate states with t_{2g} and e_g symmetries, respectively. A tiny hump at 4967 eV corresponds to the t_{2g} peak, whereas clear peaks at 4969 eV can be attributed to the e_g peak. The reason why t_{2g} peak intensity is very weak is mainly because it is forbidden in a dipole and is allowed in quadrupole approximation. In the K-edge spectra, the probability of the 1*s* to 3*d* transition is much lower than that of the dipole transition. This effect can be observed in other bulk materials [62, 63]. The intensity of the e_g peak increases as the local distortion in the TiO_6 octahedron increases, because the $pd\sigma$ hybridization between the Ti-3*d* e_g orbitals

and O $p\sigma$ orbitals becomes more pronounced, resulting in a relatively large dipole component. It has been reported that the intensity of the e_g peak is proportional to the mean-square displacement of a Ti ion from the center of the TiO_6 octahedron [62, 64].

As shown in the inset of Fig. 4.8, the e_g peak of the $BaTiO_3$ thin film is larger than that of the standard powder. In addition, the t_{2g} hump of the thin film almost flattens out. This observation can be attributed to the compressive strain resulting from the lattice mismatch between the $BaTiO_3$ film and the underlying substrate. Because the $BaTiO_3$ film has a preferred orientation of the c-axis with enhanced tetragonality, a distinct dielectric response can be expected.

The shoulder structure at 4980 eV is a characteristic of $BaTiO_3$. Though the electronic states responsible for this structure have not been identified yet, the shoulder structure indicates the contribution of the A-site ions in perovskite titanates; the room-temperature spectra of commercial $ATiO_3$ powders (A = Pb, Ba, and Sr) are shown in Fig. 4.9. In contrast to paraelectric $SrTiO_3$ with the cubic symmetry for which no shoulder structure is observed in its spectra, ferroelectric $BaTiO_3$ and $PbTiO_3$ with the tetragonal symmetry do exhibit shoulder structures. Differences in near edge structure between $BaTiO_3$ and $PbTiO_3$ may be due to differences in the hybridization of Ti $4p$ states with the states of A-site ions (i.e., Ba $6p$ vs Pb $6p$) [65]. Moreover, the intensity of these structures seems to depend on the degree of ferroelectricity; accordingly, $PbTiO_3$ has a more prominent shoulder structure compared with $BaTiO_3$.

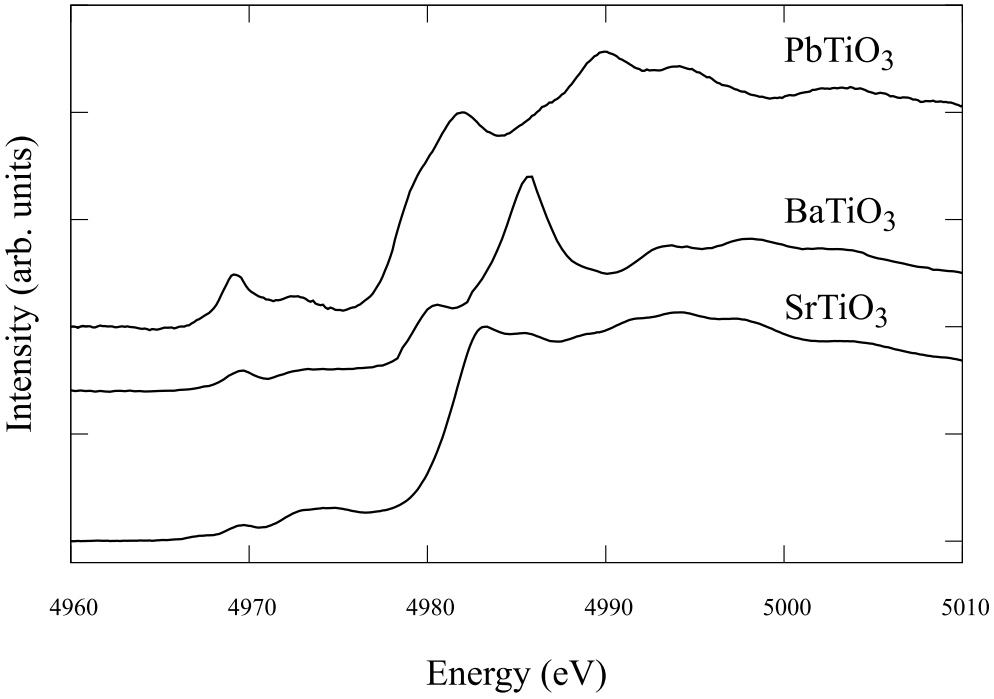

Fig. 4.9: Ti K-edge XANES spectra for standard $ATiO_3$ (A = Pb, Ba, Sr) powders at room temperature.

This trend can also be confirmed based on a series of Ti K-edge spectra of $(Ba_{1-x}, Ca_x)TiO_3$ (x = 0, 0.1, 0.18, 0.233, and 0.3), which are shown in Fig. 4.10. In particular, $(Ba_{1-x}, Ca_x)TiO_3$ stays in the tetragonal phase within the considered x range, and therefore, ferroelectricity remains stable [66, 67]. As can be seen in Fig. 4.10, the intensity of the shoulder structure decreases monotonically with increasing x, i.e., decreasing Ba concentration. Similar results have been reported for $Ba(Zr_x, Ti_{1-x})O_3$ [68, 69]. Likewise, the intensity of the shoulder structure decreases with an increase in x, i.e., a decrease in the Ti content. From these results, it can be concluded that the intensity of the shoulder structure in $BaTiO_3$ spectra reflects the electronic hybridization between Ti and Ba. This seemingly implausible claim has a theoretical background proposed by Ghosez *et al.* based on the Born effective charges of each constituent atom [25].

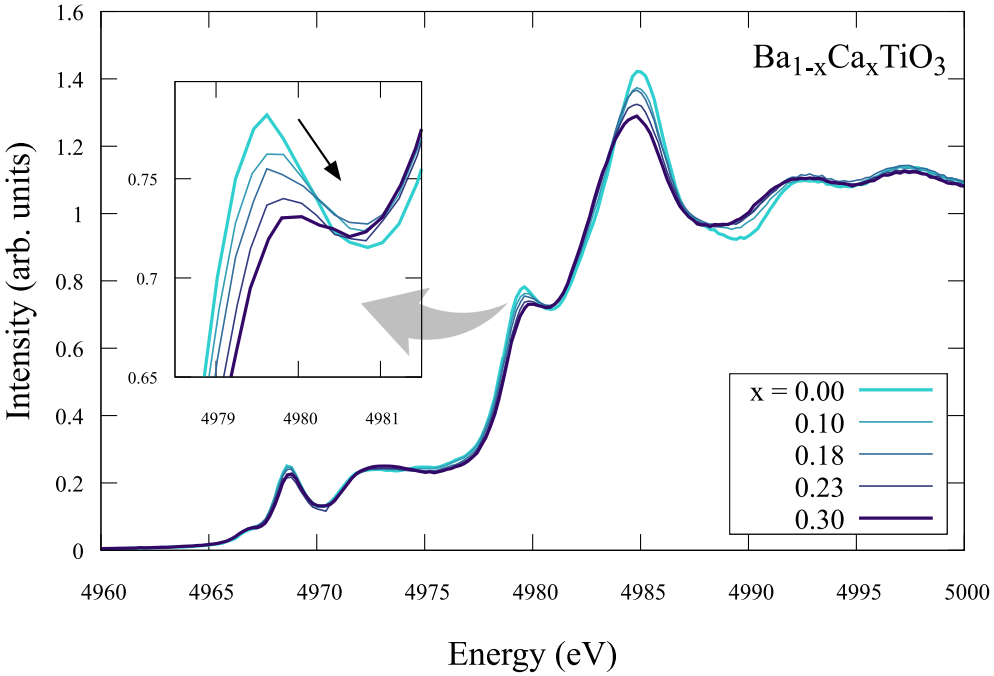

Fig. 4.10: Ti K-edge XANES spectra for $(Ba_{1-x}, Ca_x)TiO_3$ powders at room temperature.

As discussed above, because the e_g peak and shoulder structure directly reflect the ferroelectricity of perovskite titanates, These spectral features are focused as well as the main peak in the TR experiments. The time variation of the applied electric field (E) for one cycle is shown in Fig. 4.12(d); a symmetric positive-and-negative triangular field for 1 ms and a field-free duration time of 2 ms was applied in sequence. The time variation of the triangular pulse corresponds to 1 kHz, which is the same frequency as that used for the hysteresis measurements. It should be noted that the field-free region is included to prevent Joule heating as well as to provide the field-free condition. In addition, not static but AC electric field is utilized to eliminate any undesired influence from fatigue, which ensures that the relative change in a short time frame is detectable. No measurable drift of the observed signals dependent on time has been observed.

4.3.2 Electric-field dependence of Ti K-edge XANES

The maximum variation of spectra with electric fields is shown in Fig. 4.11. The increase of e_g peak intensity is 0.6 % and the peak shifts are not observed. These tiny changes are due to a small distortion caused by electric fields [18, 19]. The unchanged Ti oxidation state before and after experiments is verified

by seeing peak positions in XAS spectra. If the valence number of Ti or its local structure changes, the chemical shifts will occur, as described in Section 3.2. In this case, any changes in the peak positions were not observed with and without electric fields.

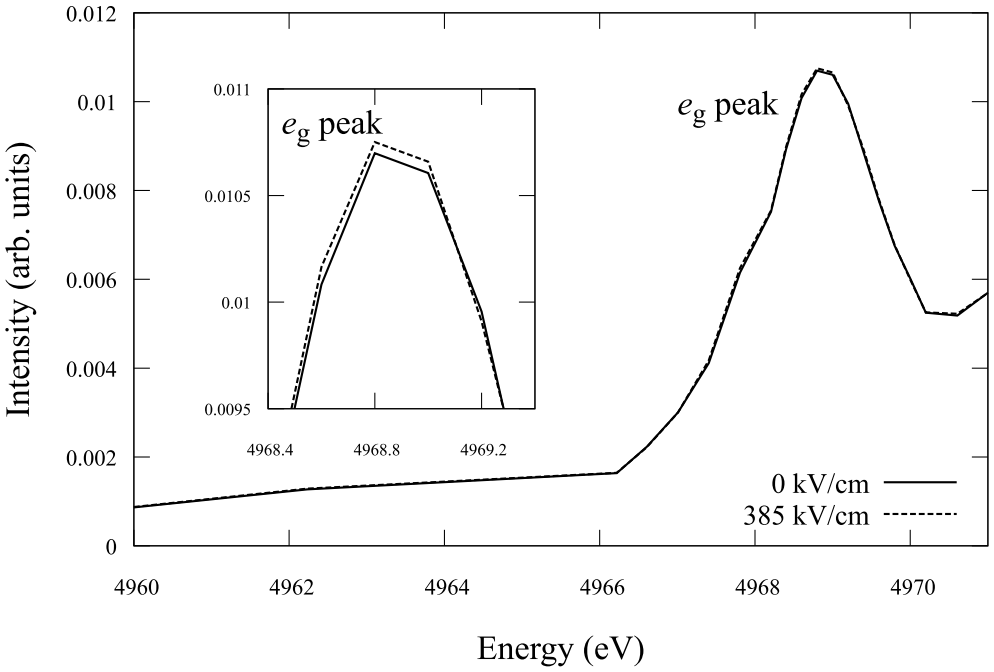

Fig. 4.11: Ti K-edge XANES spectra for the $BaTiO_3$ thin film with and without electric fields.

The time variation of the area-integrated intensities of the e_g peak, shoulder structure, and main peak are presented in Fig. 4.12a, b, and c, respectively. The integration area is set to ± 1 eV around the local maxima of each spectral feature, and the integrated intensity is normalized to the unity by the average intensity around an applied field of 0 kV/cm for 1–2 ms. The width of the time window (τ_w) for each plot is 80 μs. The signal-to-noise ratio can be estimated in the region from 1–2 ms. Intensities in this region should be constant but there is still noise left.

It is obvious that the intensities of the e_g peak and shoulder structure are synchronized with the magnitude of the applied electric field $|E|$ beyond the noise level of $\sim$0.05%. The intensities of both features increase as the magnitude of the applied field increases. The interaction of X-rays with the electronic states of $BaTiO_3$ is dependent not on the polarity of the electric polarization but on the magnitude of polarization; therefore, one-half period of the applied field was observed. This result confirms that not only the e_g

peak but also the shoulder structure is associated with the ferroelectricity of $BaTiO_3$. In contrast, the intensity of the main peak changes in the opposite manner, i.e., its intensity decreases with increasing $|E|$. A naive interpretation of this opposite trend is the broadening of the $4p$ electronic states because of the reduction in the coordination symmetry of the Ti ion under the applied electric field.

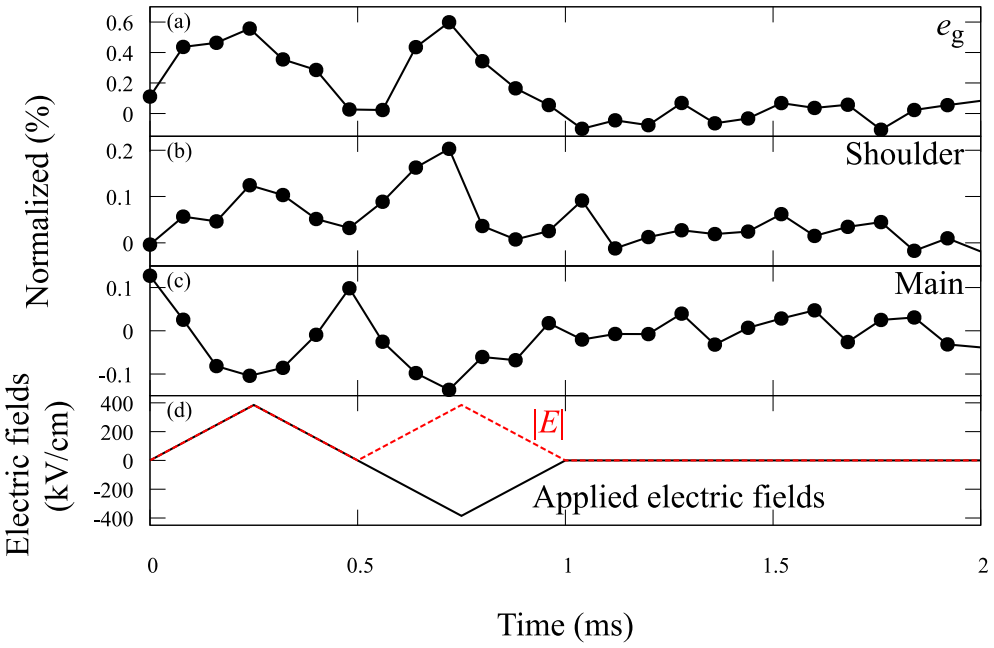

Fig. 4.12: Time-dependence of integrated intensities for (a) e_g peaks, (b) shoulder structure, and (c) main peak under (d) applied electric fields.

To better understand the time variation of the spectral features, the time variations of the e_g-peak intensity for various τ_w are presented in Fig. 4.13. Because of the detection of all SDD signals using the time stamp information, it is possible to change the τ_w to any period longer than the minimum interval of the DSP-processed signals, which is typically around 0.1 μs and depends on the setting of the instrument. The time variation of the e_g-peak intensity is evident at any τ_w, even though the noise level increases as the τ_w becomes smaller. In general, the response of the electronic states to the applied electric field is instantaneous; therefore, the time variation of spectral features shows the same trend regardless of τ_w.

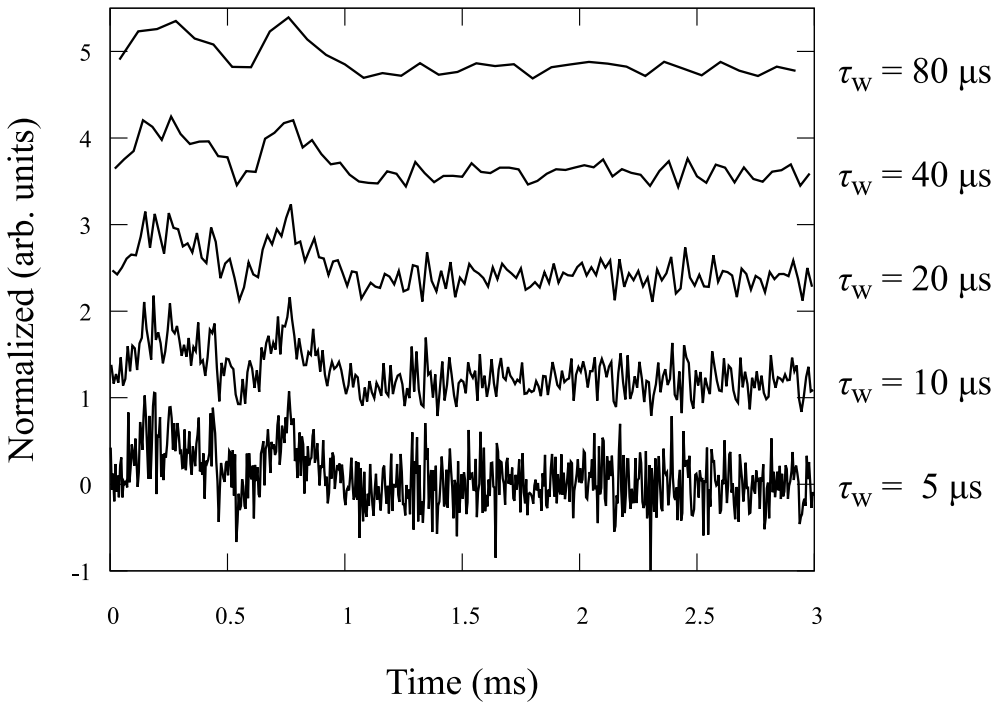

Fig. 4.13: Temporal variation of e_g peaks for various time windows τ_w.

4.3.3 Theoretical calculation

To provide a theoretical background for the interpretation of the observed spectral features, the experimental spectra were compared with the simulated spectra obtained using the FEFF 9.6 program, which is based on the multiple scattering theory [45].

An example of structural parameters used for XANES calculations is shown in Table 4.1. These values are based on a diffraction result reported by Yashima *et al.* [70]. The atomic clusters with a radius of approximately 12 Å were generated from the unit cell. Self-consistent muffin-tin potentials for all atoms were calculated. The cluster radius for the self-consistency loop is 5 Å. All multiple scattering paths up to 6.7 Å, including the 2nd nearest Ti–Ba atomic pairs, are summed to infinite order. The dipole and quadrupole transitions were taken into account.

Table 4.1: Basic structural model for $BaTiO_3$ spectra calculation [70]

Lattice		Atomic positions	
Formula	$BaTiO_3$	Ba	(0, 0, 0)
Space group	P4mm	Ti	(1/2, 1/2, 0.4876)
$a = b$	3.999 Å	O1	(1/2, 1/2, 0.0237)
c	4.03265 Å	O2	(1/2, 0, 0.5163)

Fig. 4.14 shows the simulated Ti K-edge spectrum with structural parameters presented in Table 4.1. The e_g peak, shoulder structure, and main peak are successfully reproduced by the simulation. It should be noted that the energy positions of these features are inconsistent with experimental results. In general, it is difficult to obtain the correct energy values by simulations. because it would be required to include electron correlation effects appropriately, such as the core-hole effects generated by the electron excitation, and the many-body effects beyond the single electron approximation. In this study, relative changes in spectral features are focused when structural parameters are changed.

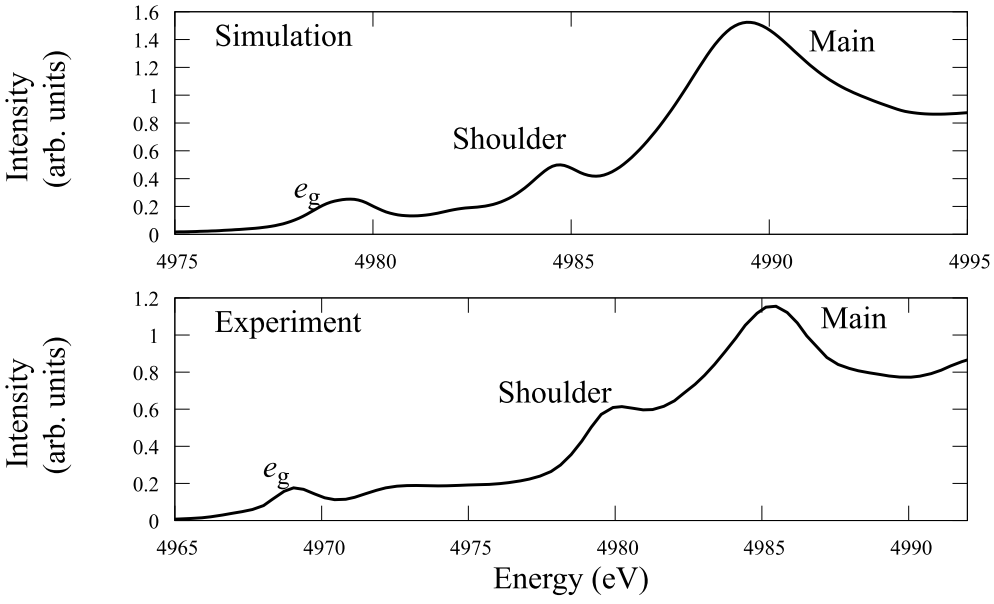

Fig. 4.14: Simulated Ti K-edge spectrum of $BaTiO_3$. (a) Calculated XANES spectrum obtained by FEFF. (b) Experimental XANES spectrum for a standard $BaTiO_3$ powder.

Effects of Ti displacement

The simulation results are shown in Fig. 4.15, wherein the Ti off-center displacement (δ_{Ti}) was varied from $\delta_{\mathrm{Ti}} = 0$ (body-center) to 0.04 in atomic units. The atomic positions in this model are provided in Table 4.2. Though $\delta_{\mathrm{Ti}} = 0.04$ is large compared to the experimental one, this magnified model makes the spectral changes clear. As already discussed in the literature [62]. the intensity of the e_{g} peak increases with increasing δ_{Ti}, which reflects the enhanced Ti $3d$ e_{g}–O $2p$ hybridization. In contrast, the intensity of the main peak decreases oppositely. The simulated results suggest that not only the effect of broadening the Ti $4p$ states but also the compensation for the number of unoccupied states would be a plausible reason for the observed spectral features.

Table 4.2: Ti off-center model

	Atomic positions
Ba	(0, 0, 0)
Ti	(1/2, 1/2, $1/2 + \delta_{\mathrm{Ti}}$)
O1	(1/2, 1/2, 0)
O2	(1/2, 0, 1/2)

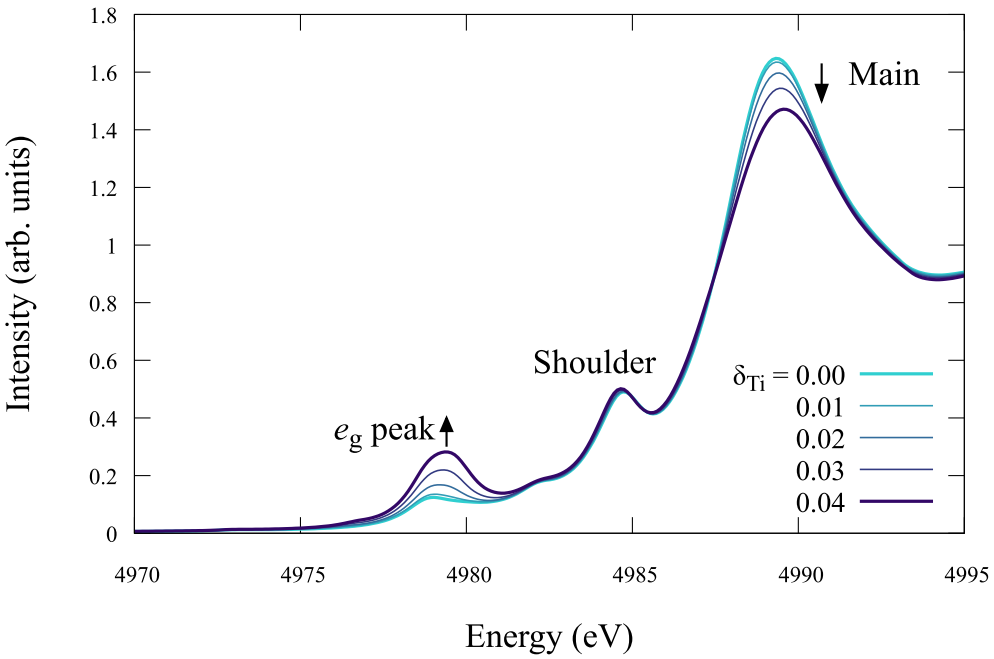

Fig. 4.15: Calculated Ti K-edge XANES spectra for several Ti off-center displacements.

The relationship between Ti off-center displacement and the e_g peak intensity is obtained through the XANES calculation. As can be seen in Fig. 4.16, The integrated intensity of the e_g peak is proportional to the square magnitude of the Ti displacement δ_{Ti}. These results agree well with the previous theoretical study reported by Vedrinskii *et al.*; the proposed equation for a cubic model is as follows [62]:

$$I \propto \frac{\langle \delta_{Ti}^2 \rangle}{c^{5.5}}, \tag{4.1}$$

where I is the pre-edge peak intensity and c is the lattice constant. This relationship can be utilized to estimate the enhancement in the Ti displacement induced by electric fields from variations of the e_g peak intensity, observed in the TR experiments. However, the quantitative analysis would be challenging because I is not zero in $BaTiO_3$ even without electric fields. The TR-XANES results are combined with EXAFS results and the determination of Ti displacements is described in Chapter 6.

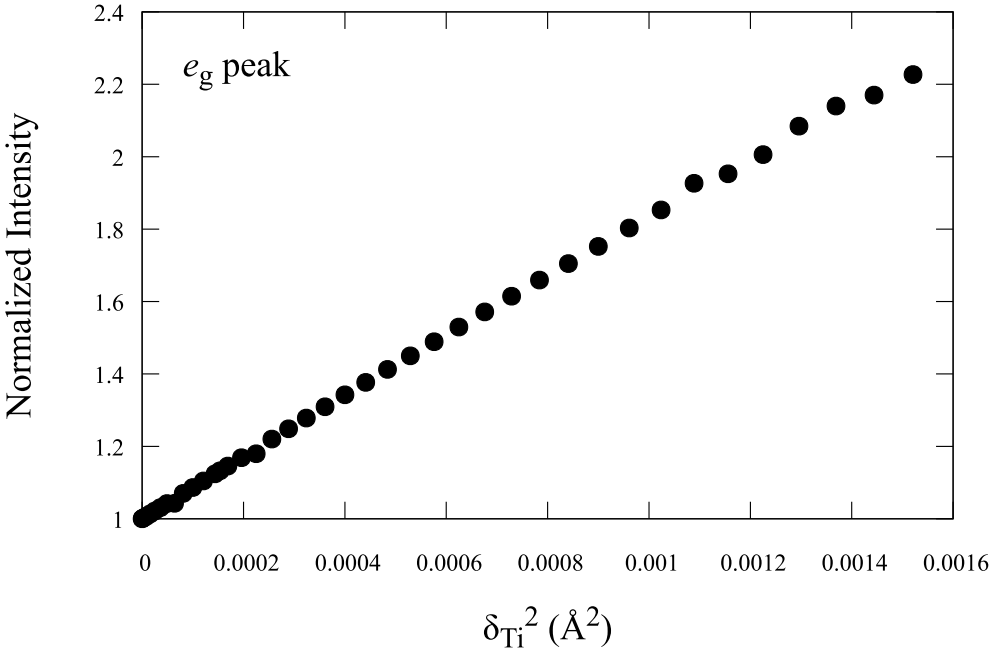

Fig. 4.16: Integrated intensities of e_g peaks obtained from calculated Ti K-edge XANES spectra.

It can be inferred from the molecular orbital theory that the binding energy is changed by the enhancement of Ti $3d$ e_g–O $2p$ hybridization, that is, an energy shift of the e_g peak would be induced by applied electric fields. However, no energy shift has been observed in the TR measurements. This is because the expected energy shift is tiny. The e_g peak shift was estimated from XANES calculations, as shown in Fig. 4.17. When Ti is displaced 0.05 Å from the center, the e_g peak position shifts by ≈ 0.5 eV. The lattice distortion induced by electric fields is an order of ~ 0.001 Å, reported by Tazaki *et al.* [18]. Therefore, the energy shift is estimated to be an order of 10 meV; it cannot be observed by conventional XAS measurements, the energy resolution of which is commonly ~ 0.1 eV.

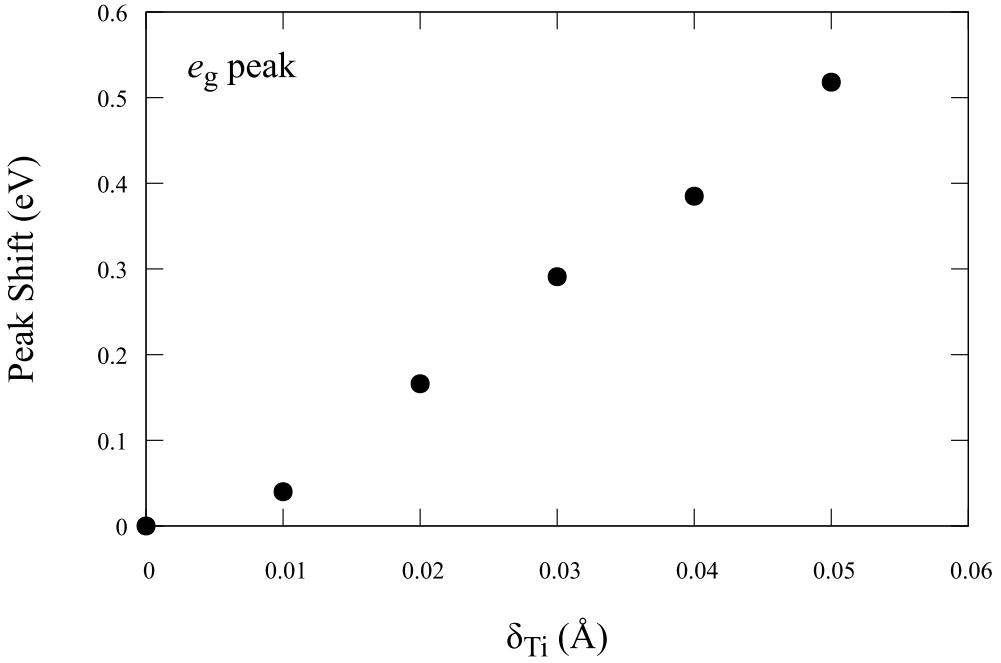

Fig. 4.17: Peak shifts of e_g peaks obtained from calculated Ti K-edge XANES spectra.

Effects of lattice distortion

In contrast to the e_g peak and main peak, the shoulder structure is less sensitive to the Ti off-center displacements, clearly indicating the existence of a different contribution to the shoulder structure. As mentioned in Section 4.3.1, the shoulder structure is attributed to the A-site contribution to Ti as per several experimental results.

One possible reason for variations in the shoulder structure under electric fields is due to lattice distortion. The lattice distortion is induced by applied electric fields because of the piezoelectricity in $BaTiO_3$, as experimentally observed in previous studies [18, 71, 19]. The tetragonality (the c/a ratio) is also changed in the case of (Ba, Ca)TiO_3 [66, 67], where the shoulder structure intensity decreases with Ca substitutions in A-site (Fig. 4.10). Thus, it can be inferred that the tetragonality affects the shoulder structure.

Simulated spectra for several c/a ratios with a constant volume were calculated. The structural parameters for these calculations are shown in Table 4.3. The Ti off-center displacement in this structural model is fixed to be 0.05 Å, which agrees with the diffraction result without electric fields reported by Yashima *et al.* [70]. Fig. 4.18 shows the calculated results. Though all spectral features are less sensitive to the lattice distortion compared to

the Ti off-centering effects, the intensity of the shoulder structure increases as the c/a ratio increases. The c/a ratio is correlated to the atomic distance between Ba and Ti atoms. Hence, the shrinkage of Ba–Ti pairs would enhance Ba contributions into Ti electronic states.

Table 4.3: Lattice distortion model

Unit cell volume	64.49 Å^3
Ti off-center displacement	0.05 Å
Ba position	(0, 0, 0)
O1 position	(1/2, 1/2, 0)
O2 position	(1/2, 0, 1/2)

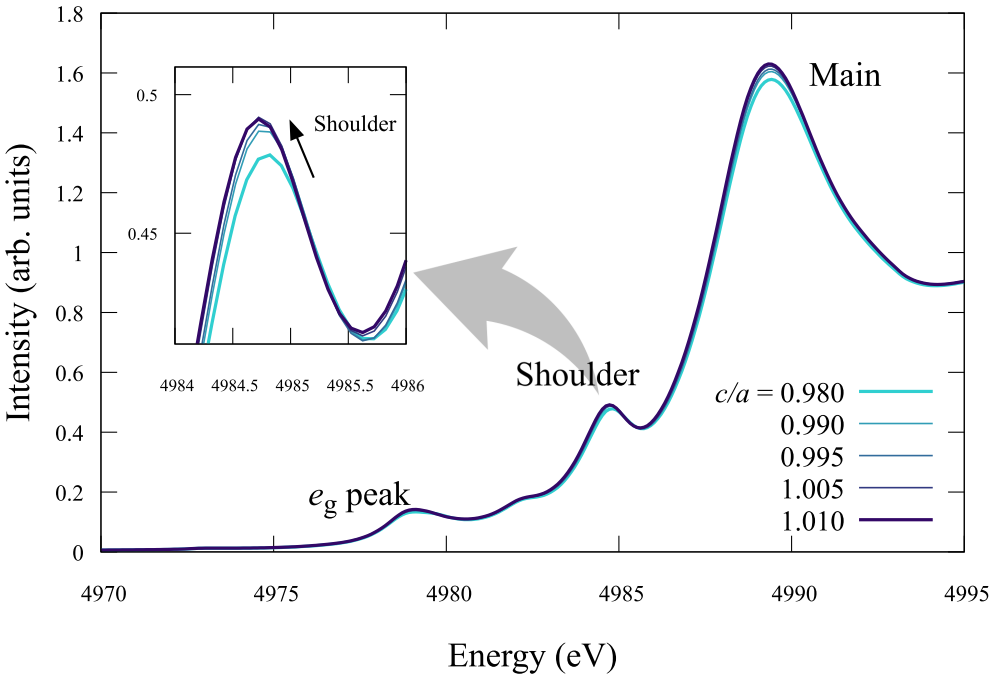

Fig. 4.18: Calculated Ti K-edge XANES spectra for several tetragonality (c/a).

It might be noted that the Ba–Ti atomic pair is the closest at $c/a = 1$ without Ti off-center displacements. However, the Ba–Ti distance is the shortest when $c/a > 1$ with any Ti off-center displacement. It can be verified

by a simple equation. A Ba–Ti distance, where Ba is located at $(0, 0, 0)$ and Ti is displaced δ_{Ti} from the center $(1/2, 1/2, 1/2)$, is obtained by

$$\sqrt{\frac{1}{2}a^2 + \left(\frac{1}{2}c - \delta_{\mathrm{Ti}}\right)^2}, \tag{4.2}$$

where, a and c are the lattice constants. This is a function of the c/a ratio within the constraints of the constant lattice volume: $V = a^2 c = const.$ By putting $x = c/a$, it gives

$$r_{\mathrm{Ba-Ti}}(x) = \sqrt{\frac{1}{2}\left(\frac{V}{x}\right)^{\frac{2}{3}} + \left[\frac{1}{2}(x^2 V)^{\frac{1}{3}} - \delta_{\mathrm{Ti}}\right]^2}. \tag{4.3}$$

When the Ba–Ti atomic distance $r_{\mathrm{Ba-Ti}}$ is a minimum, the first derivative $\partial r_{\mathrm{Ba-Ti}}/\partial x$ is zero:

$$x^2 - 2\delta_{\mathrm{Ti}} V^{-\frac{1}{3}} x^{\frac{4}{3}} - 1 = 0. \tag{4.4}$$

It is obvious that $x = c/a = 1$ satisfies this equation if $\delta_{\mathrm{Ti}} = 0$, otherwise $c/a \neq 1$ at the minimum. This feature is presented in Fig. 4.19 by plotting Eq. (4.3). The c/a ratio at the minimum Ba–Ti distance increases as δ_{Ti} increases.

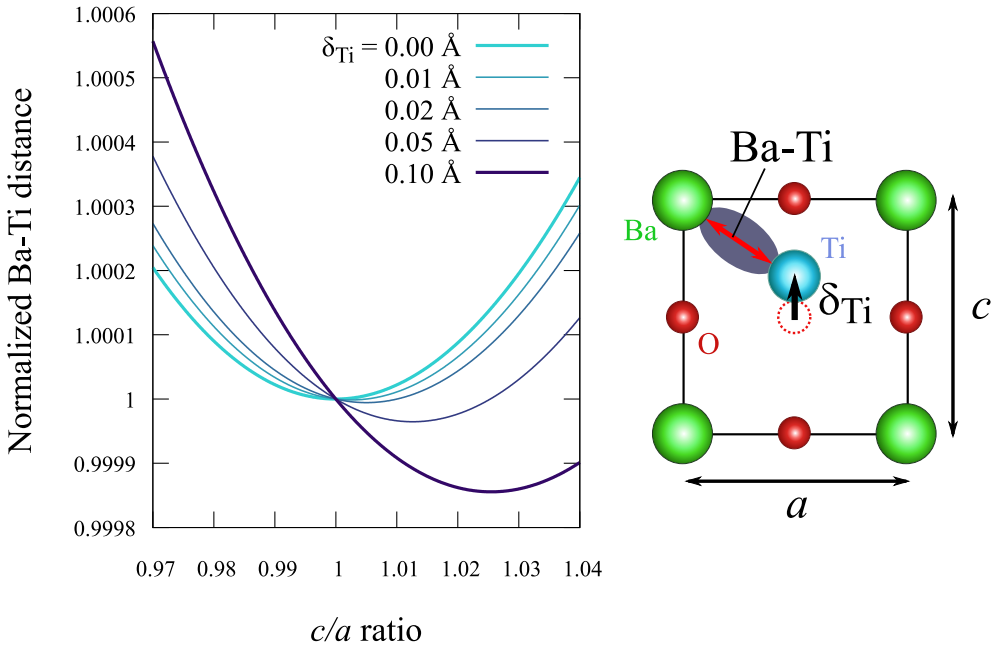

Fig. 4.19: Dependence of the c/a ratio on a Ba–Ti atomic distance for several δ_{Ti} values. The distance is normalized to one at $c/a = 0$.

There is a 0.05 Å displacement of a Ti atom in $BaTiO_3$ even without electric fields. When $\delta_{\mathrm{Ti}} = 0.05$ Å, the Ba–Ti distance is the minimum with $c/a = 1.0126$, which is less than the c/a ratio under electric fields, observed by diffraction studies [18, 71, 19]. Hence, the Ti–Ba distance increases with the increase in the c/a ratio within the experimental conditions.

4.3.4 Responses of electronic states under electric fields

In this section, an interpretation is provided for experimental spectra under electric fields. Observed variations in the intensity of spectral features are summarized in Table 4.4.

The e_{g} peak corresponds to the Ti $3d$ e_{g} – O $2p$ hybridization. The intensity of the e_{g} peak is proportional to the square magnitude of Ti off-center displacements. Thus, the observed variations in the e_{g} peak intensities demonstrate the enhancement in the Ti displacements and Ti–O hybridization under applied electric fields.

The main peak corresponds to the Ti $4p$ states. Simulated spectra indicated that the main peak intensity decreases with the enhancement in the Ti displacement. On the other hand, the lattice distortion increases the main peak intensity. The experimental results show a small decrease in the main peak intensity under external electric fields, indicating that effects of Ti off-center are greater than those of the lattice distortion in this case.

The shoulder structure corresponds to A-site contributions to Ti electronic states. Though the shoulder structure is rather insensitive to atomic structures compared to the e_{g} peak intensity, the shoulder structure intensity is related to the atomic distance between Ba and Ti atoms; It was observed that the intensity was enhanced as the Ba–Ti distance decreases. In this study, the Ti displacement and lattice distortion caused the shrinkage of Ba–Ti pairs and the enhancement in the Ba contribution.

Table 4.4: Comparison between experimental results under applied electric fields and two structural models for Ti K-edge spectra.

Spectral features	Experimental results	Simulation models	
		Ti off-center	Lattice distortion
e_g peak	+ 0.6 %	++	+
Shoulder	+ 0.2 %	+	+
Main peak	− 0.1 %	−−	+

++: strongly increased, +: increased, −−: strongly decreased

Any Ba–Ti covalency are not observed by diffraction measurements [20], however, the anomalous large Born effective charge of Ba has been reported in theoretical calculations [25, 26], indicating the existence of Ba–Ti interaction. These theoretical calculations demonstrate that Ba $5p$ are hybridized with O $2p$, which is also hybridized with Ti $3d$. Thus, one possible explanation for the variations in the shoulder structure is due to the Ba–Ti interaction through oxygen orbitals. because of the anomalous large Born effective charges of Ba atoms. Although this hybridization is much weaker than the Ti–O hybridization, the comparable variations in the Ba–Ti interactions are expected It can be assumed that the shoulder structure is derived from three-body interactions involving Ba, Ti, and O atoms. Since it is difficult to obtain the Ba–O relationship only from Ti K-edge spectra, it is required to probe the local environment around Ba atoms. Ba K-edge spectra under electric fields are presented in Chapter 5.

4.4 Conclusions

For the first time, Ti K-edge TR-XAS measurements for a $BaTiO_3$ thin film were performed under the application of a triangular AC electric field. This technique enables to detect tiny changes in spectra and observe electronic states under electric fields. Three characteristic features in Ti K-edge spectra were studied, namely the pre-edge e_g peak, shoulder structure, and main peak. Using structural model simulations, it was confirmed that Ti off-center displacements affect the increase in the e_g-peak intensity and decrease in the main peak intensity. Moreover, it was observed that the shoulder structure intensity was enhanced by the Ti off-center displacement and the lattice distortion. Both two structural variations should shorten the Ba–Ti atomic distance, resulting in the enhancement of A-site contributions into Ti

electronic states. Therefore, the Ba contribution to the ferroelectric property of $BaTiO_3$ via electronic hybridization is concluded experimentally using the novel TR-XAS technique.

Chapter 5

Ba K-edge EXAFS for $BaTiO_3$ single crystal

5.1 Introduction

Average structures under electric fields have been observed for $BaTiO_3$ with both bulk crystals [18, 19] and thin films [71], as well as for another prevalent piezoelectric material, Pb(Zr, Ti)O_3 [72, 73]. However, the detection of changes in atomic displacement is extremely difficult because the electric-field-induced structural change is generally very small; the change of the lattice constants under electric fields is on the order of 0.1 pm [18, 19, 71].

In this chapter, extended X-ray absorption fine structure (EXAFS) measurements were performed to investigate the atomic displacements of $BaTiO_3$ under applied electric fields. EXAFS is an element-specific technique and is sensitive to the local geometric structures around the absorbing atoms. This is advantageous for investigating the Ti off-center displacements, which cause changes in the Ba–Ti bond lengths. Moreover, EXAFS can detect atomic motion on the order of femtometers by comparing differences in the EXAFS signals, such as those caused by magnetostriction [74] and isotopic effects [75]. The reverse Monte Carlo (RMC) refinements for Ba K-edge spectra enable to analyze Ba K-edge spectra with sufficient precision to detect such a small variation in atomic distances.

The RMC refinements with tetragonal constraints, describable by displacive models, revealed the systematic change in the Ba–Ti bond lengths and the angles between Ba–Ti–Ba under electric fields. The enhancement of the Ti off-center displacements relative to those in the absence of electric fields is ~ 0.5 pm; this study provides unprecedented quantitative and experimental evidence for the enhancement of Ti off-center displacements. These

findings develop an in-depth understanding of how the local structure is related to the macroscopic properties, such as the electromechanical properties of ferroelectric materials.

5.2 Experimental

5.2.1 Sample preparation

A single crystal $BaTiO_3$ (001) sample used in this study was purchased from Crystal Base Co. Ltd, Japan. The sample, as received, was polished to a thickness of 120 μm, which is appropriate for X-ray transmission. Au electrodes were evaporated on the sample for the EXAFS measurements under external electric fields.

The ferroelectricity of the sample was verified by measuring the polarization-electric field ($P - E$) hysteresis using a ferroelectric tester (FCE-fast, Toyo Corporation, Japan) with a triangular electric field of 1 kHz, as presented in Fig. 5.1. The open loops indicate the ferroelectricity of the sample. Ba K-edge EXAFS spectra were measured at 7.7, 11.5, and 15.4 kV/cm; these are larger than the coercive field, and the sample is less sensitive to extrinsic effects such as *a*-*c* domain switching.

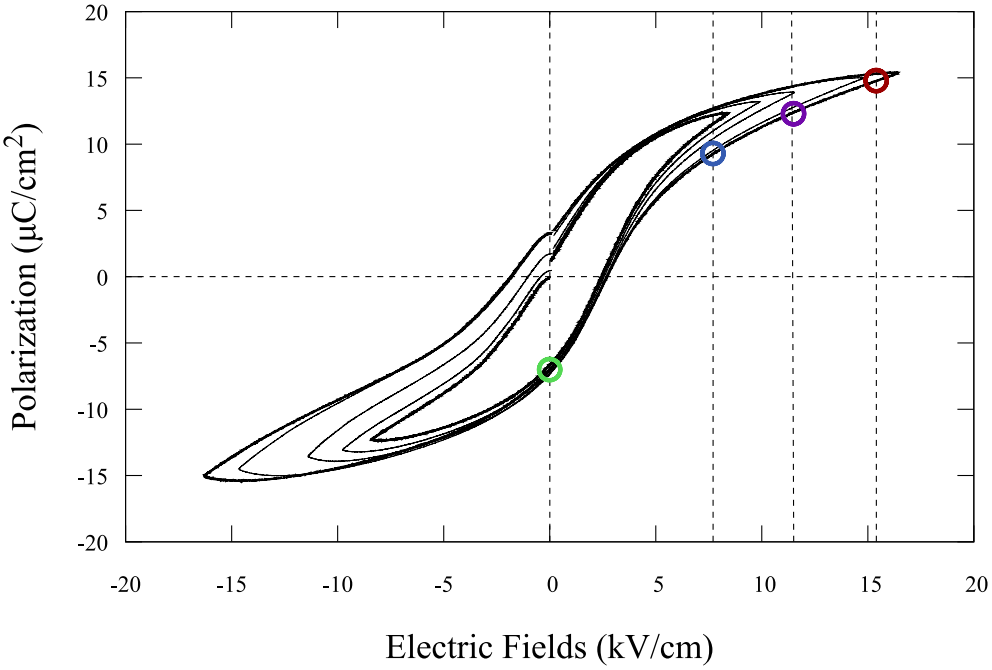

Fig. 5.1: $P - E$ hysteresis loops of a single crystal $BaTiO_3$ sample with amplitude from 0.77 kV/cm to 15.4 kV/cm and frequency of 1 kHz. Open circles represent the points for Ba K-edge EXAFS measurements.

5.2.2 EXAFS measurements

The transmission EXAFS measurements at the Ba K-edge of $BaTiO_3$ were performed at the beamline BL01-B1 at SPring-8 (Hyogo, Japan). The direction of the incident X-ray was perpendicular to the sample (001) surface, and parallel to the direction of the applied electric fields. The applied electric fields are static unlike the TR-XANES experiments in Chapter 4, because no significant dynamical effect was detected in Fig. 4.12. A systematic electric-field dependence was observed in the EXAFS spectra and those Fourier transform spectra (Fig. 5.2). The variation of the amplitudes in the presence of electric fields can be detected, indicating that the electric fields cause static and dynamic disorder effects, such as local atomic displacements and thermal atomic vibrations. The RMC techniques provide quantitative information on these disorder effects. Thus, it is possible to extract static disorder effects regarding the enhancement of the Ti off-center displacements caused by electric fields.

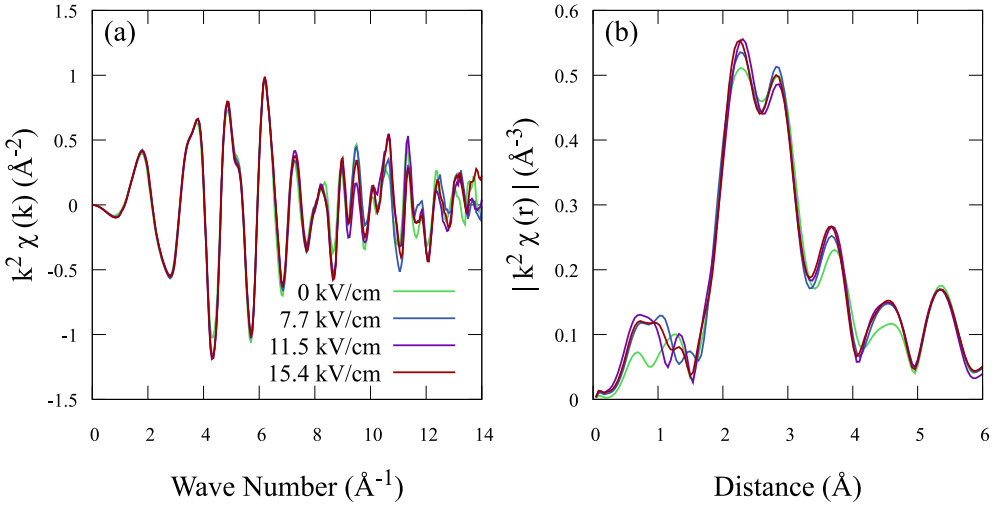

Fig. 5.2: Experimental Ba K-edge EXAFS spectra for a monocrystal $BaTiO_3$ sample. (a) Reciprocal k-space signals and (b) Fourier transform of EXAFS signals.

5.2.3 EXAFS signal processing

General aspects of wavelet transform

The RMC refinements fitted the Morlet wavelet transform (WT) of EXAFS signals. The WT is a signal-processing method, widely used in various applications such as sound and image processing. It provides two-dimensional information on the periodic signal with simultaneous localization in the reciprocal k and real R space. The WT of a given EXAFS signal $\chi(k)$ is defined as

$$WT(k,R) = \sqrt{\frac{R}{R_0}} \int_{-\infty}^{\infty} k'^n \chi(k') \phi \left[\frac{R}{R_0}(k'-k) \right] dk', \tag{5.1}$$

where R_0 is the parameter of a characteristic length, determining the k- and R-space resolutions, and $\phi(k)$ is a function called the "mother wavelet". The function $\phi(k)$ for the Morlet WT is defined as

$$\phi(k) = \exp(-2iR_0k)\exp(-k^2). \tag{5.2}$$

The WT is the inner product of the analyzed spectrum $\chi(k)$ and the translated and scaled mother wavelet $\phi(k)$. The inner product of two functions is large when these functions have similar shapes.

A simple model case is provided to demonstrate the advantage of the WT. Fig. 5.3 shows two wave functions. These two signals generate the same modulus of the Fourier transform (FT). Thus, it is impossible to distinguish

two signals using the FT modulus unless including the additional information such as the real and imaginary parts of the FT. Opposite to the FT, the WT moduli shown in Fig. 5.4 reveal the difference between these two signals more clearly.

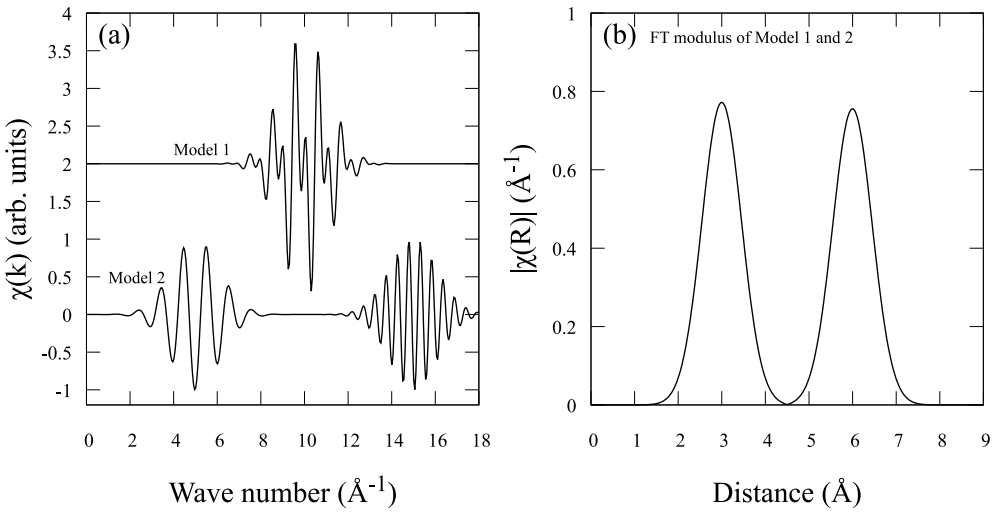

Fig. 5.3: Two model signals generating the same Fourier transform (FT) modulus. (a) Two different model signals with (b) the same FT modulus.

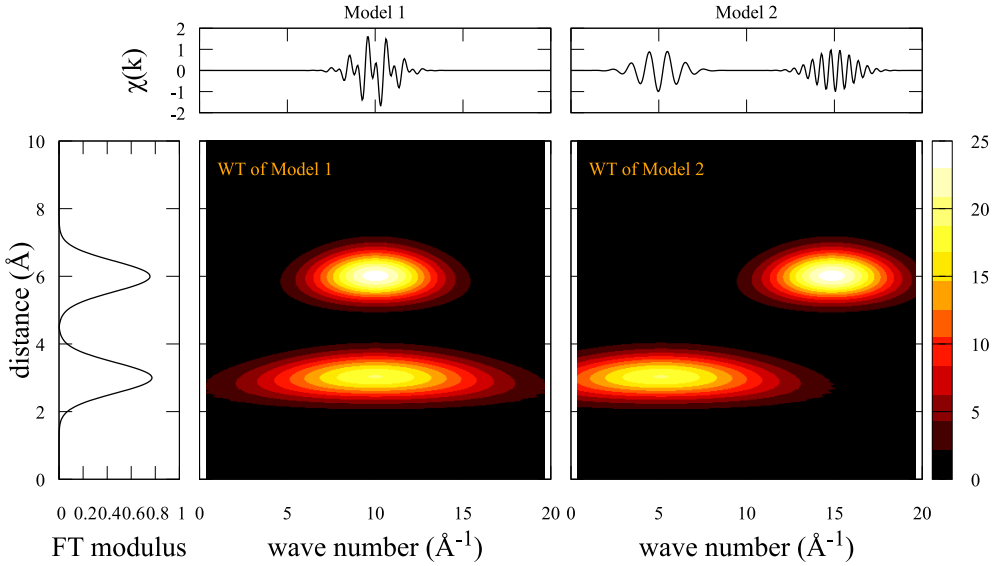

Fig. 5.4: Wavelet transform (WT) of two model signals, shown in Fig. 5.3. Signals in k space and their same FT modulus are also provided.

In a practical case, the WT is helpful for the separation of scattering-path contributions by their elemental nature. EXAFS signals are derived from the interference between the excited photoelectron and the photoelectron waves scattered by surrounding atoms. The back-scattering amplitudes depend on their elements, hence, the maximum amplitudes occur at different k values with two different types of atoms. For example, Fig. 5.5 shows the FT and WT of experimental Fe K-edge spectra for $Fe_{65}Ni_{35}$ and $Fe_{72}Pt_{28}$ alloys. The FT moduli have similar shapes in both alloys because the lattice symmetry of these two materials is the same face-centered cubic (fcc). Despite the similarity in the lattice structure, $Fe_{72}Pt_{28}$ has more prominent WT features than $Fe_{65}Ni_{35}$ in the high k-region ($k > 9$ Å^{-1}) due to the large atomic number of Pt. As is the same with this example, the WT is a useful tool to extract information including multiple-scattering paths in the case of $BaTiO_3$.

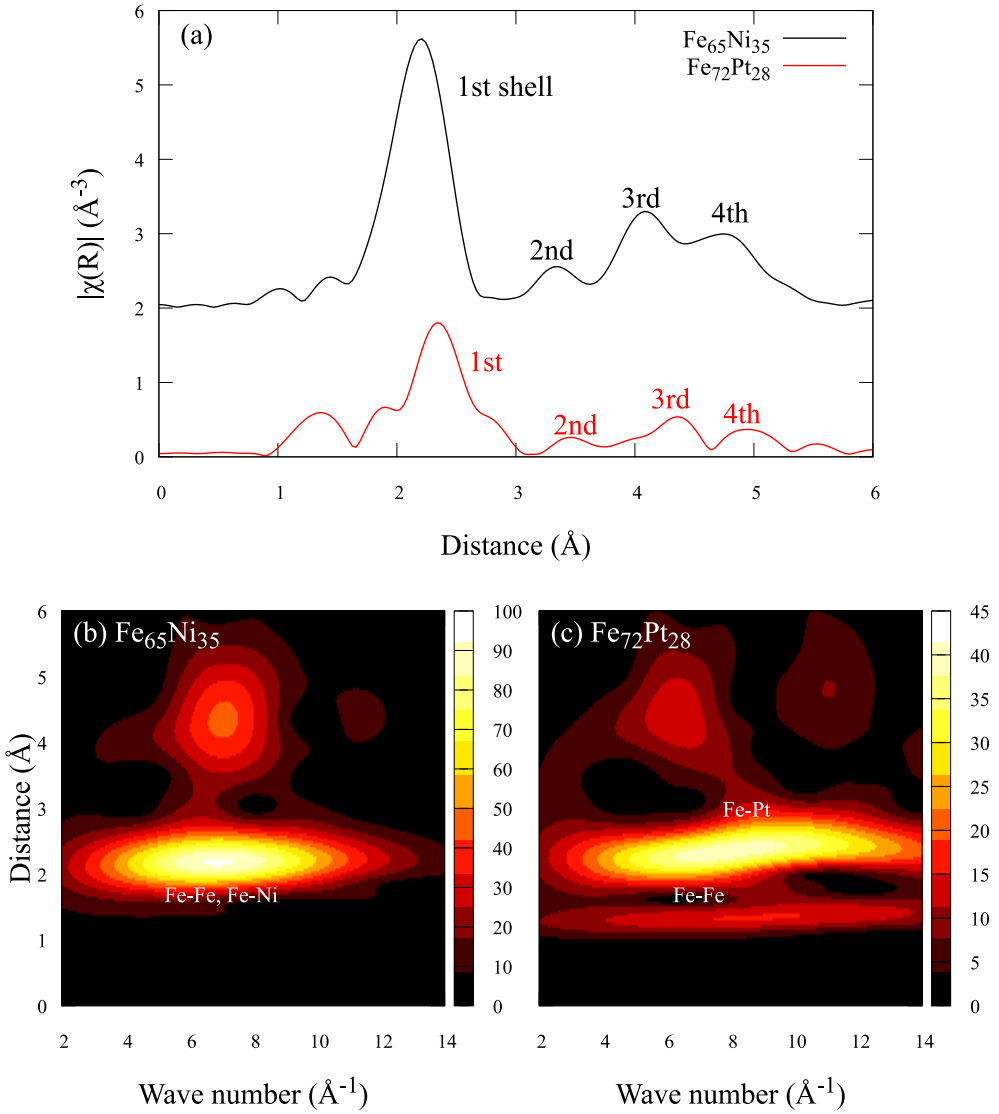

Fig. 5.5: Fourier transform (FT) and wavelet transform (WT) of experimental Fe K-edge spectra for two alloys: $Fe_{65}Ni_{35}$ and $Fe_{72}Pt_{28}$. (a) The FT moduli for $Fe_{65}Ni_{35}$ and $Fe_{72}Pt_{28}$. The WT moduli for (b) $Fe_{65}Ni_{35}$ and (c) $Fe_{72}Pt_{28}$. Sample preparations are described in detail elsewhere [76].

Wavelet transform of Ba K-edge EXAFS

Not only single-scattering (SS) paths but also multiple-scattering (MS) paths have significant contributions to EXAFS signals in perovskite materials. SS and MS effects can be distinguished by the WT as well as the path extraction mentioned in the previous section. Fig. 5.6 shows examples of the theoretical

WT of $BaTiO_3$ Ba K-edge EXAFS spectra. Some spectral features in the WT in Fig. 5.6a, especially in $8 < k < 12$ Å^{-1} and $5 < R < 7$ Å, correspond to the MS effects.

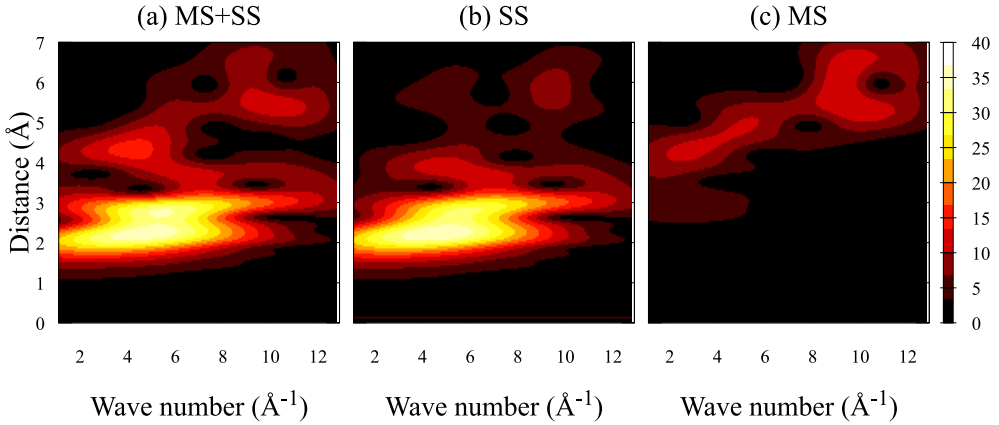

Fig. 5.6: Wavelet transform (WT) of theoretical $BaTiO_3$ Ba K-edge spectra (a) including single-scattering (SS) and multiple-scattering (MS) contributions, (b) only with SS effects, and (c) only with MS effects.

It is possible to fit EXAFS signals in comparison between the experimental and theoretical spectra in k and R space simultaneously. Fig. 5.7 provides an example of the fitting quality of RMC refinements for the data without electric fields. The theoretical spectra agree well with the experimental data in both the k and R space. The distinct MS feature, shown in Fig. 5.6c, is also reproduced by the theoretical WT. These MS effects include Ba–Ti–Ba scattering paths, thus RMC refinements are capable to extract information on the angle between Ba–Ti–Ba.

The WT is also utilized for noise reduction such as de-glitching. Fig. 5.7c shows the residuals between experimental and theoretical WT results, as calculated by

$$\frac{|WT_{exp}(k,R) - WT_{theory}(k,R)|}{|WT_{exp}(k,R)|}, \tag{5.3}$$

where $WT_{exp}(k,R)$ and $WT_{theory}(k,R)$ are the experimental and theoretical WT, respectively. The region below 0.5 Å in R range and some small spots in Fig. 5.7c imply the large residual due to the noise contamination in experimental EXAFS signals because the correct scattering paths have finite-extent contributions in both R and k region.

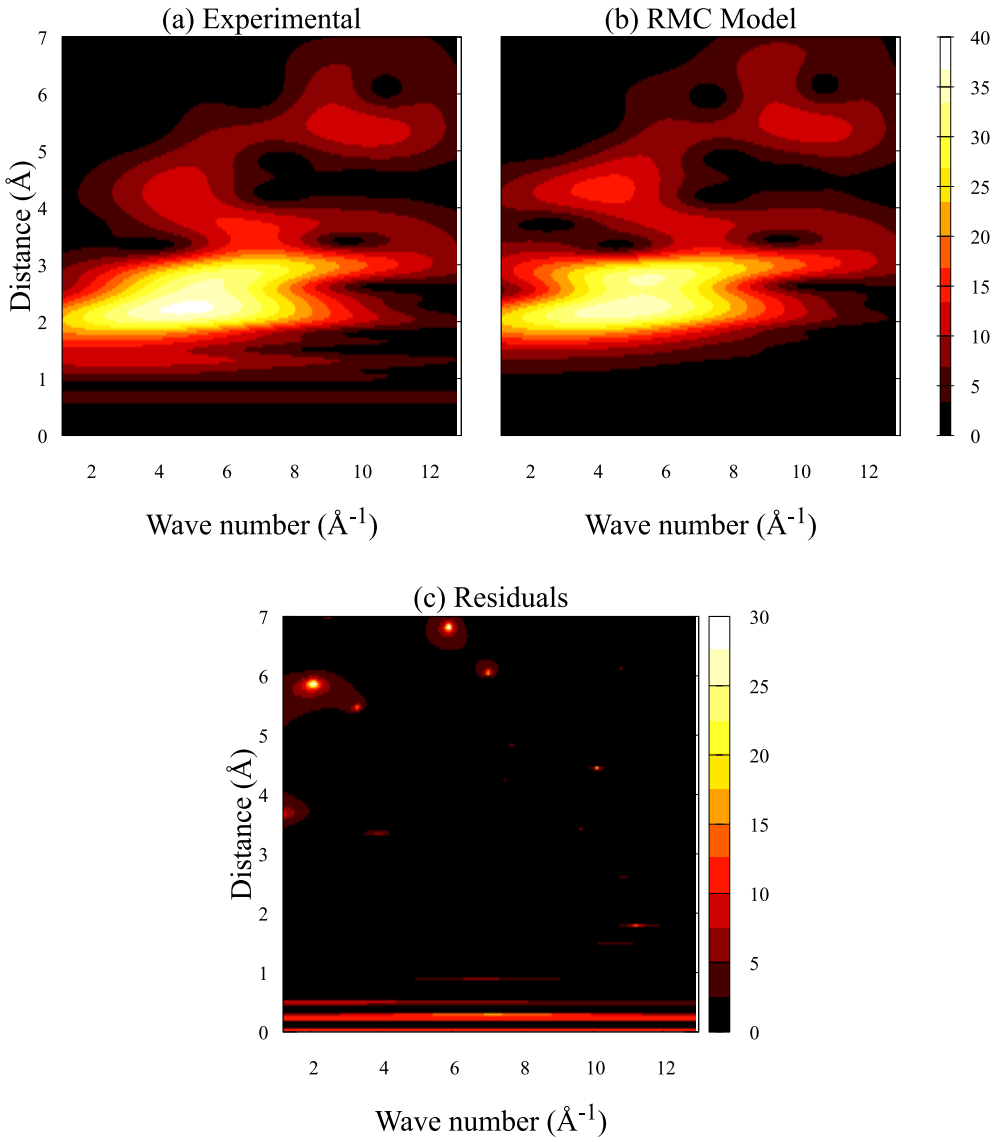

Fig. 5.7: Example of the fitting quality in RMC refinements using the wavelet transform (WT) of $BaTiO_3$ Ba K-edge EXAFS signals. (a) The experimental WT without electric fields, (b) the theoretical WT obtained by RMC refinements, and (c) residuals between (a) and (b).

For verifying the fitting quality in a familiar way, using FT, Fig. 5.8 shows examples of comparison between FT/back-FT of the experimental and theoretical spectra. The theoretical spectra agree well with the experimental data in both the k and R space. Hence, the obtained 3D structural model successfully reproduced the experimental EXAFS signals.

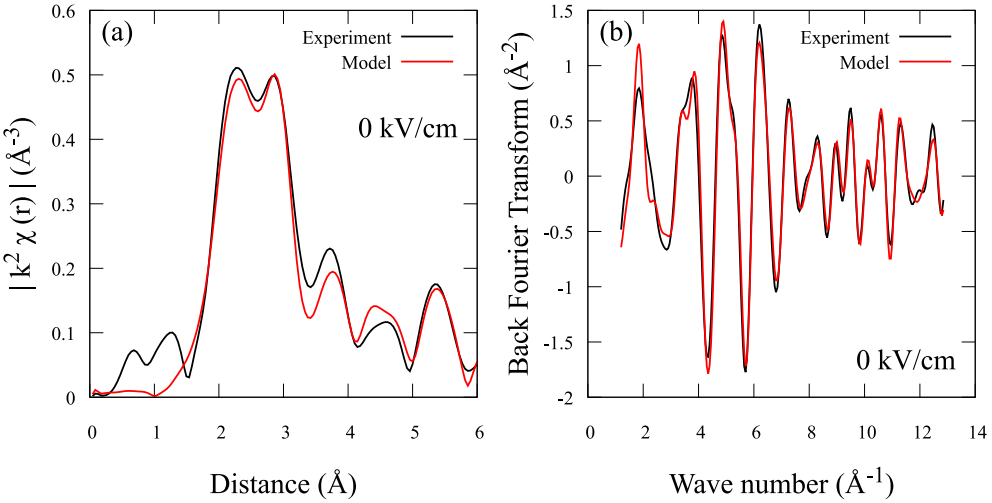

Fig. 5.8: Example of fitting by the RMC refinement. (a) Fourier transform of EXAFS signals (FT) and (b) Back Fourier transform of FT.

5.2.4 RMC calculations

The EXAFS spectra were analyzed using reverse Monte Carlo (RMC) refinements, as implemented in the EvAX code [77], with simulated annealing optimization methods to avoid entrapment in local minima. An evolutionary algorithm method is also employed for an effective exploration of the large space of possible atomic configurations. An explanatory description of these algorithms is provided in Section 3.3.1. A final optimized structure is obtained as a single supercell or a set of atomic configurations.

A supercell used in this study is generated from $6 \times 6 \times 6$ unit cells, containing 1,080 atoms. The initial structural parameters, including the lattice constants and atomic positions, were obtained from previous reports [14, 16]. The lattice constants $a = 3.9921$ Å and $c = 4.0366$ Å were used for the data without electric fields, and were estimated by interpolating the diffraction data [14, 16]. For the data under electric fields, a and c were calculated using the piezoelectric coefficients $d_{33} = 149$ pm/V and $d_{31} = -82$ pm/V, as reported by a diffraction study [18]. The initial fractional coordinates of the atomic positions for all data analysis are shown in Table 5.1, obtained by Kwei *et al.* [14] at 300 K.

Table 5.1: Initial atomic positions used in RMC refinements [14]

Atom	fractional coordinates
Ba	(0, 0, 0)
Ti	(1/2, 1/2, 0.482)
O1	(1/2, 1/2, 0.016)
O2	(1/2, 0, 0.515)

The theoretical spectra obtained from the supercell were calculated using FEFF8.5L code [45], which is based on the multiple-scattering (MS) theory. Scattering paths up to 7.0 Å, including Ba–Ti–Ba paths, were used in the calculations. The MS effects up to the 4th order were considered. Some multiple scattering paths were ignored to reduce the computational time. The contribution of the ignored paths to the EXAFS spectrum is smaller than 0.2% of that of the shortest Ba–O single scattering path that contributed the most to the spectrum.

The displacement of an atom in the supercell is limited to a maximum of 0.15 Å. These constraints keep the average structure with tetragonal symmetry, observed in the diffraction studies. This model is similar to a displacive model since Ti atoms are not allowed to move largely and relocate to the position along the ⟨111⟩ direction. As previous mentioned in Chapter 4, the enhancement in the Ti displacements under electric fields is revealed. Thus, one can expect detectable changes by using tetragonal constraints. Despite the limitation of Ti movements, the disorder characters in an order-disorder model were also obtained, as described later in Chapter 6. Although other constants with large allowable displacement were also applied, obtained results were unphysical due to artifacts in the data analysis. This artifact problem is described in the next section.

5.2.5 Statistical analysis

It should be emphasized that the final atomic configurations, optimized by RMC refinements, is not unique. A different set of atomic coordinates is obtained by repeating the calculation with the same condition or constraints but with different pseudo-random numbers. However, the statistical characteristics, such as average and deviation values of atomic distances and bond angles, are close in both calculations, and agree with their experimental results. While the exact positions of atoms in the supercell are 'meaningless', average atomic positions are meaningful information. This situation also

occurs in experimental observations. The 'true' structure, i.e., the exact positions of all atoms in a material, can be never reached. The atomic structure is not 'static', even in a simple case, due to atomic vibrations; There is a difference between the time-average positions and the positions at an instant of time. Therefore, the statistical information obtained from RMC models is essential and should be discussed when using RMC calculations.

It is safe to validate whether radial or angle distribution functions (RDF or angleDF) represent plausible features because RMC models are statistical. Generally, average values accurately reflect the actual properties when a histogram is symmetrical. The calculated RDF and AngleDF with/without electric fields are presented in Fig. 5.9 and Fig. 5.10, respectively. The RDF and AngleDF have symmetric shapes and agree well with the sum of several Gaussian peaks. The number of Gaussian peaks is the same as the number of groups separated using diffraction results. For example, the Ba–Ti bond lengths in the tetragonal phase can be grouped into two groups: 4 × 3.43 Å, and 4 × 3.51 Å. The positions and widths of these Gaussian peaks were the average of the bond lengths and their deviations, respectively. The good accordance of this model guarantees the validity of the statistical analysis.

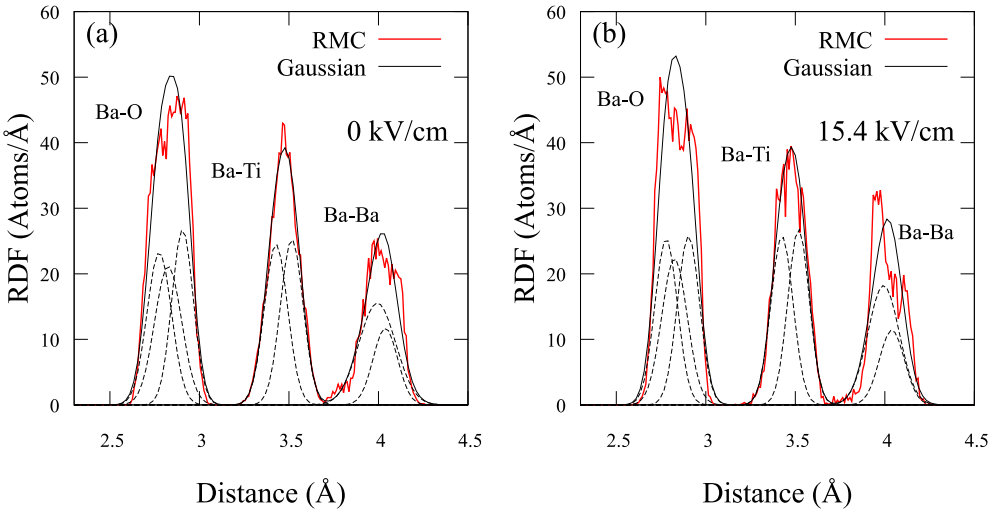

Fig. 5.9: Radial distribution function (RDF) for obtained RMC refinements at (a) 0 kV/cm and (b) 15.4 kV/cm. The solid black line implies the sum of several Gaussian peaks (dashed line). The positions and widths of the Gaussian peaks were calculated from the RMC results.

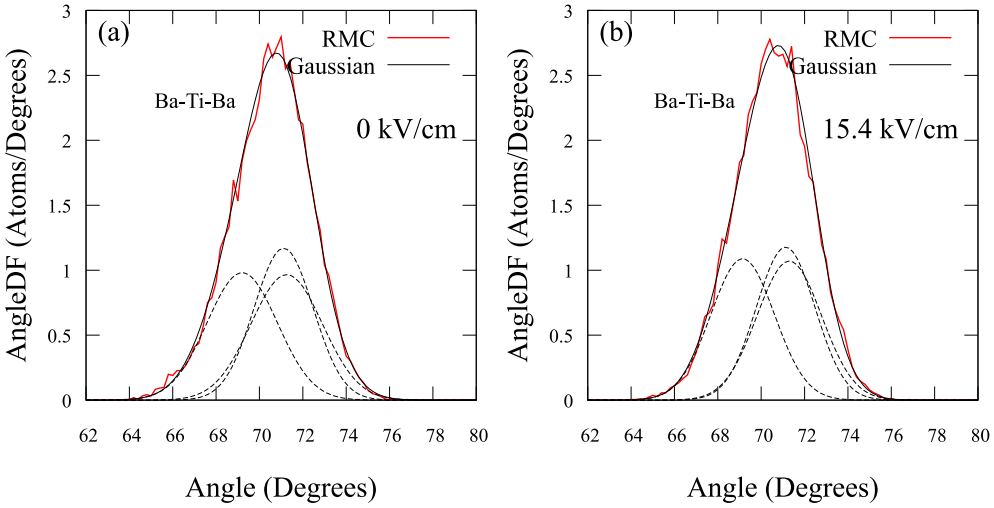

Fig. 5.10: Angle distribution function (angleDF) for obtained RMC refinements at (a) 0 kV/cm and (b) 15.4 kV/cm. The solid black line implies the sum of several Gaussian peaks (dashed line). The positions and widths of the Gaussian peaks were calculated from the RMC results.

The limitation of atomic movements in RMC processes is sometimes required to obtain proper results. In this study, overfitting was found to occur when large atomic displacements were allowed. Fig. 5.11 shows the RDF obtained from RMC refinements with a maximum displacement $d_{max} = 0.40$ Å. Unlike the RDF with $d_{max} = 0.15$ Å, the Ba–Ti and Ba–Ba small peaks appear around 3.0 and 3.6 Å, respectively. These artifacts are due to overfitting the experimental data including noises. The average bond length is underestimated in this case. Hence, the average structure is inconsistent with the diffraction data. For this reason, $d_{max} = 0.15$ Å was employed in RMC calculations.

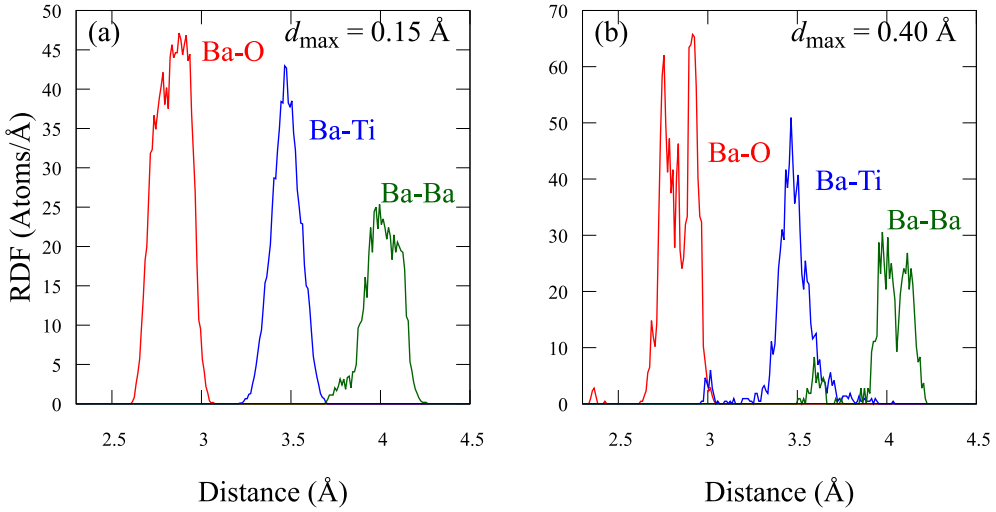

Fig. 5.11: Radial distribution function (RDF) without electric fields obtained from RMC calculations using constraints with a maximum atomic displacement of (a) 0.15 Å and (b) 0.40 Å.

The local structural parameters such as bond lengths, angles, and Ti displacements were analyzed statistically from the atomic coordinates of the 3D structure model obtained from the RMC calculations. According to the diffraction data, the Ba–Ti atomic pairs can be grouped into two groups: 4 long bonds and 4 short bonds. This information was used to average the bond lengths in the local structure around the Ba atoms, and compare the obtained values to the global structure (the initial structure of calculations).

The parallel mean-square relative displacement (parallel MSRD) was calculated by

$$\langle u_{\parallel}^2 \rangle = \frac{1}{N} \sum_{(i,j)} \left\| (\boldsymbol{u}_i - \boldsymbol{u}_j) \cdot \hat{\boldsymbol{R}} \right\|^2, \tag{5.4}$$

and the perpendicular MSRD was calculated by

$$\langle u_{\perp}^2 \rangle = \frac{1}{N} \sum_{(i,j)} \left\| (\boldsymbol{u}_i - \boldsymbol{u}_j) - \hat{\boldsymbol{R}} \left[(\boldsymbol{u}_i - \boldsymbol{u}_j) \cdot \hat{\boldsymbol{R}} \right] \right\|^2, \tag{5.5}$$

where $\boldsymbol{u}_i$ is the relative displacement from the average position of atom i, $\hat{\boldsymbol{R}}$ is the direction of relative displacement between average positions of the absorber and scattering atoms, and N is the number of atomic pairs.

5.3 Results and discussion

5.3.1 Bond lengths and angles

Fig. 5.12 shows the electric-field dependence of the obtained Ba–Ti bond lengths compared with those in the global structure (the initial structure of RMC calculations). The Ba–Ti bond length in the absence of electric fields is consistent with that obtained from the diffraction data within an experimental error of ~ 0.003 Å, as reported by G. H. Kwei *et al.* [14]. As revealed, the presence of electric fields causes the shrinkage of the Ba–Ti bond lengths. This shrinkage is more prominent than the lattice distortion (the dashed line and shaded area in Fig. 5.12) that is calculated from the piezoelectric coefficients, $d_{33} = 149 \pm 54$ pm/V and $d_{31} = -82 \pm 61$ pm/V, reported in a previous diffraction study [18]. Therefore, the electric-field dependence of the Ba–Ti bond length is clearly due to the displacement of the Ti atoms.

The RMC schemes revealed bond-length variations of less than 1 pm. In previous studies, accuracy on the order of femtometers was achieved using differential methods for simple metals, such as FeCo and Ge [74, 75]. Unlike these metals, it is impossible to isolate a single-shell contribution to the EXAFS signals in the present study. There are several short lengths corresponding to the 1st (Ba–O), 2nd (Ba–Ti), and 3rd (Ba–Ba) coordination shells, and all three contributions overlap in the R space of the EXAFS signals. To overcome this difficulty, the RMC refinement was fully utilized; An excellent accuracy (< 1 pm) was achieved when determining the change in the interatomic distances under the tetragonal constraints.

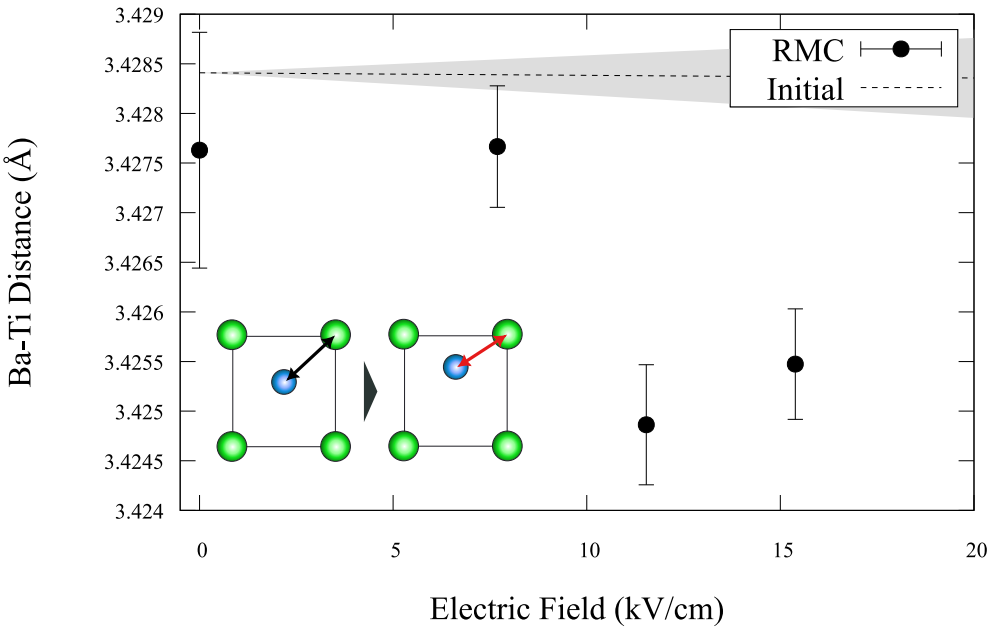

Fig. 5.12: Electric-field dependence of Ba–Ti bond lengths obtained from RMC results. Dashed line with a barely discernible slope shows bond lengths calculated from the initial structure of RMC refinements. The initial structure was estimated from diffraction data. Shaded area represents the estimated uncertainty calculated from experimental error in diffraction data. Error bars indicate the standard deviations obtained from five RMC calculations with different random seeds.

The bond angle is also a good indicator of the Ti displacements because any Ti displacement, relative to the Ba atoms, changes the angle between Ba–Ti–Ba. In the RMC analysis, not only single-scattering but also multiple-scattering (MS) signals were taken into account. The MS signals contain information about multi-atom distribution functions including the angle information around scattering atoms such as Ba. The RMC refinements can reproduce MS features using the tetragonal structural model, as mentioned above in Section 5.2.3, thus the angle information is accessible as well as bond lengths. As shown in Fig. 5.13, the angle decreases with an increase in the magnitude of the electric field. The trend of the electric-field dependence of the Ba–Ti–Ba angle is very similar to that exhibited by the Ba–Ti bond lengths, indicating the enhancement of the Ti off-center displacements under electric fields.

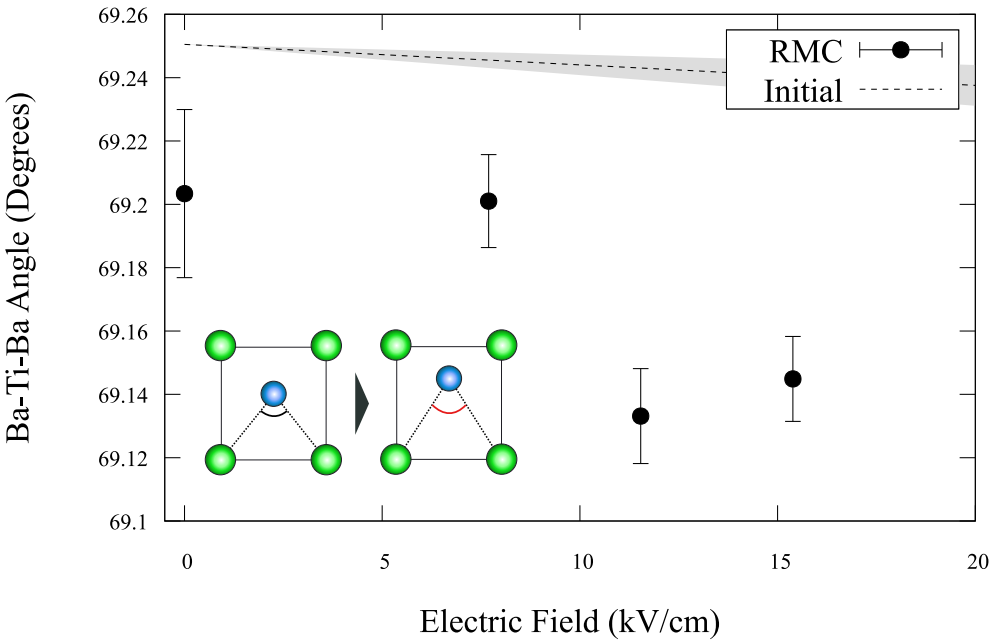

Fig. 5.13: Electric-field dependence of angle between Ba–Ti–Ba obtained from RMC results. Dashed line shows angles calculated from the initial structure of RMC refinements estimated from diffraction data. Shaded area represents the estimated uncertainty calculated from experimental error. Error bars indicate the standard deviations obtained from five RMC calculations for each point.

The difference between the interatomic distances obtained using diffraction (R) and EXAFS (r) measurements should be noted. It is due to the atomic vibrations in the direction perpendicular to the interatomic direction [78]:

$$r \approx R + \frac{\langle u_{\perp}^2 \rangle}{2R}, \tag{5.6}$$

where $\langle u_{\perp}^2 \rangle$ is the perpendicular component of the mean squared relative displacements (MSRD). As can be observed from Eq. (5.6), the bond lengths obtained from the EXAFS data are longer than those obtained from the diffraction data due to MSRD. However, the effects of MSRD on the Ba–Ti bond lengths in the presence of electric fields are almost negligible in this instance, because the variation of both $\langle u_{\parallel}^2 \rangle$ and $\langle u_{\perp}^2 \rangle$ of Ba–Ti is insensitive to the presence of electric fields, as presented in Fig. 5.14. Thus, one can expect the enhancement of the local Ti displacements.

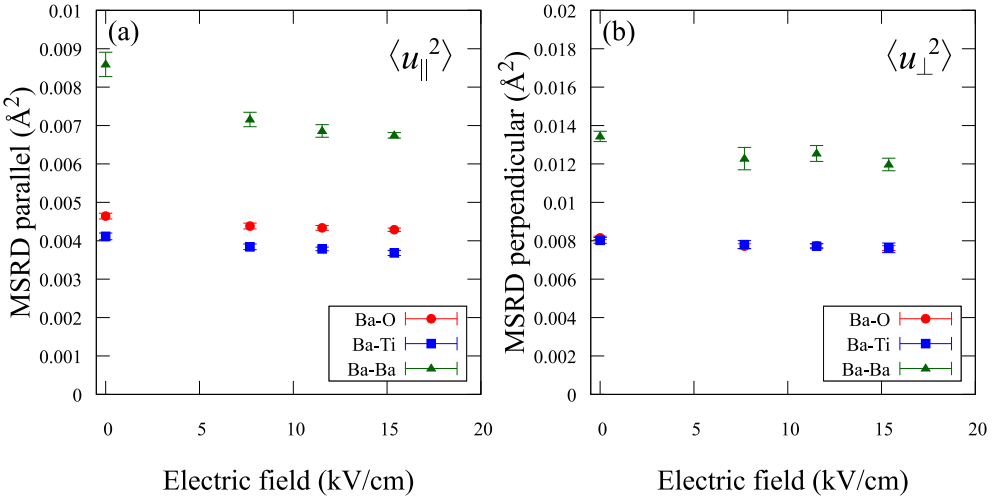

Fig. 5.14: Mean squared relative displacements (MSRD), obtained from RMC refinements: (a) parallel MSRD $\langle u_{\parallel}^2 \rangle$, (b) perpendicular MSRD $\langle u_{\perp}^2 \rangle$. Error bars indicate the standard deviations obtained from five RMC calculations for each point.

5.3.2 Titanium displacements

The magnitude of the Ti displacements was calculated from the RMC results, by using the average positions of Ba and Ti atoms. The magnitude of displacements increases as the magnitude of the applied electric field increases, as presented in Fig. 5.15a. The displacement at 15.4 kV/cm is 0.5 pm larger than that in the absence of an electric field and is of the same order of magnitude as the lattice distortion caused by the applied electric field [18]. These results support the displacive characters, where the electric polarization is mainly determined by the enhancement in the local Ti displacements [10].

The obtained direction of the Ti displacements is approximately along the [001] direction in the tetragonal phase (Fig. 5.15b). Although this result is due to the limitation of atomic movements in RMC calculations, it might show the variations in the angle of Ti displacements under electric fields, implying the order-disorder characters. Since this angle was obtained from the average positions in the supercell, the obtained results are close to the average structure. However, the clear tendency is revealed by the local structural analysis on Ti displacements from the center of TiO_6 octahedra, as presented in Chapter 6.

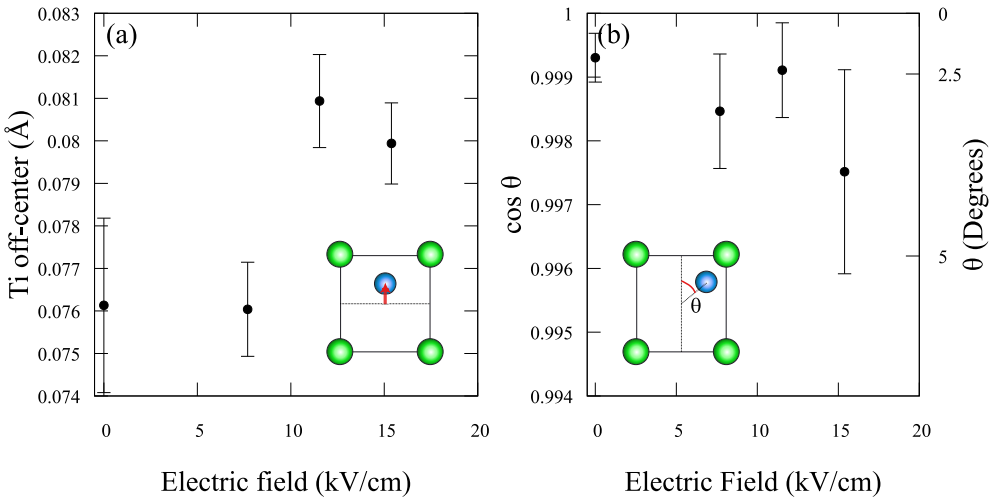

Fig. 5.15: Ti off-center displacements from the body center of lattice, obtained from RMC refinements. (a) magnitude of Ti displacements. (b) angle of Ti displacements along to *c*-axis.

Under external electric fields, thermal effects would be induced by Joule heating or electrocaloric effects [79]. The Ti displacements of $BaTiO_3$ are temperature-dependent due to pyroelectricity. To consider the thermal effects, the analysis that was used for the electric-field-dependent EXAFS spectra was employed for the temperature-dependent spectra of a single crystal, $BaTiO_3$. As observed in Fig. 5.16, the enhancement of the Ti displacements under electric fields is larger than the variation in the temperature in the tetragonal phase. Thus, electric-field effects, not thermal effects, cause the enhancement of Ti displacements.

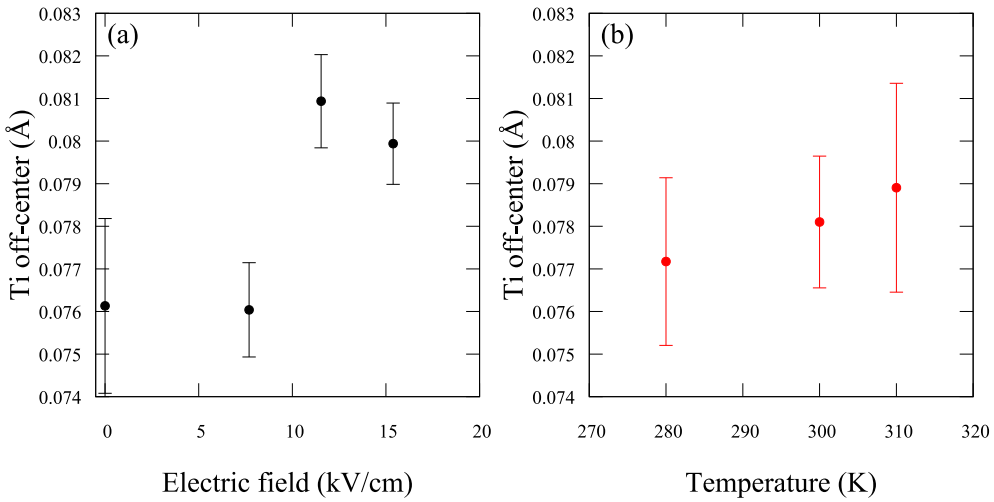

Fig. 5.16: (a) Temperature dependence and (b) Electric-field dependence of Ti displacements within single crystal $BaTiO_3$. Error bars indicate the standard deviations obtained from five RMC calculations for each point.

Although RMC refinements can determine the changes in the interatomic distance at an order of 0.1 pm, they do not suggest the absolute value of atomic displacements. The accuracy of RMC structural refinements depends on the experimental limitations of EXAFS measurements. As with traditional EXAFS analysis, the precision of the obtained Ti displacement is $\sim$ 0.01 Å. Here, absolute values depend on the initial structures used in the RMC refinements. A Ti displacement at 0 kV/cm calculated from another set of RMC refinements with a Ti atom at a different initial position is $\approx$ 0.0824 Å, which is 0.006 Å larger than that at 0 kV/cm shown in Fig. 5.15a. However, the enhancement of Ti displacements under electric fields obtained from these additional calculations is $\approx$ 0.5 pm, which is identical to that shown in Fig. 5.15a.

The use of EXAFS analysis in determining relative changes enables a high precision of less than sub-picometers, as reported in a previous study, where differential atomic motion of $\sim$ 1 fm could be detected in FeCo and Ge [74, 75]. In these studies, this degree of precision was achieved for metals, which are rather simple compared to perovskite oxides.

The RMC refinements fully utilize structural information acquired from EXAFS, which are sufficient to detect atomic perturbations. Therefore, the RMC scheme is an effective tool to investigate the relative atomic displacements from a well-known structure. Another example that would benefit from this technique is the local structural distortion induced by doping ions without any changes in the average structure.

5.3.3 Titanium K-edge XANES simulation

By analyzing the Ba K-edge EXAFS spectra, it was found that the local Ti off-center displacement increased by an order of sub-picometers in the presence of an electric field. Unlike previous RMC-EXAFS studies with multiple-edge EXAFS spectra [80, 81, 82], The results obtained in this study were derived from the single-edge fitting. It is difficult to discuss Ti off-center displacements using the Ti K-edge EXAFS spectra because the Ti K-edge EXAFS can only be measured to 250 eV above the absorption edge; this restriction is due to the existence of the Ba L_3-edge. Although the Ti K-edge EXAFS signals were not available in the RMC schemes, the simulation of the Ti K-edge spectra from the obtained 3D structure can reproduce the pre-edge XANES structure, if the 3D structure is well reconstructed using RMC simulations. Therefore, the simulation of the Ti K-edge XANES spectra and comparisons with the experimental spectra are useful in scrutinizing the RMC configurations and facilitate the validation of the Ti atomic displacements.

The Ti K-edge XANES spectra were simulated by the multiple scattering theory as implemented in the FEFF codes. The atomic clusters of a radius of approximately 12 Å were generated from each Ti atom in the simulated supercell with periodic boundary conditions. Multiple-scattering paths were considered to ~ 6.7 Å including the 2nd nearest Ba shells. The self-consistent potentials for all the atoms were calculated only at the initial structure, because the calculation for a disordered system requires extensive potential calculations for all the atoms. The final results of the Ti K-edge spectra were obtained by averaging 216 spectra for each RMC supercell containing 216 Ti atoms.

Fig. 5.17 shows the features in the calculated Ti K-edge XANES spectra. The three features (main edge, shoulder structure, and e_g peak) represent different electronic states. The main absorption edge at 4990 eV corresponds to the density of states of the unoccupied Ti $4p$ states. The intensity of the main edge is related to the disorder in the environment of Ti [83]. The shoulder structure at 4985 eV is characteristic of $BaTiO_3$ and corresponds to the hybridization of the Ti $4p$ states with the states of the Ba ions, as described in Section 4.3.1. The e_g peak at 4979 eV represents the Ti $3d$ states hybridized with O $2p$ states. This hybridization can be observed as the Ti–O covalency, supported by theoretical calculations [21, 22] and X-ray diffraction measurements [20]. The intensity of the e_g peak is a good indicator for the RMC calculations, because the peak intensity increases with an increase in the Ti off-center displacements [62].

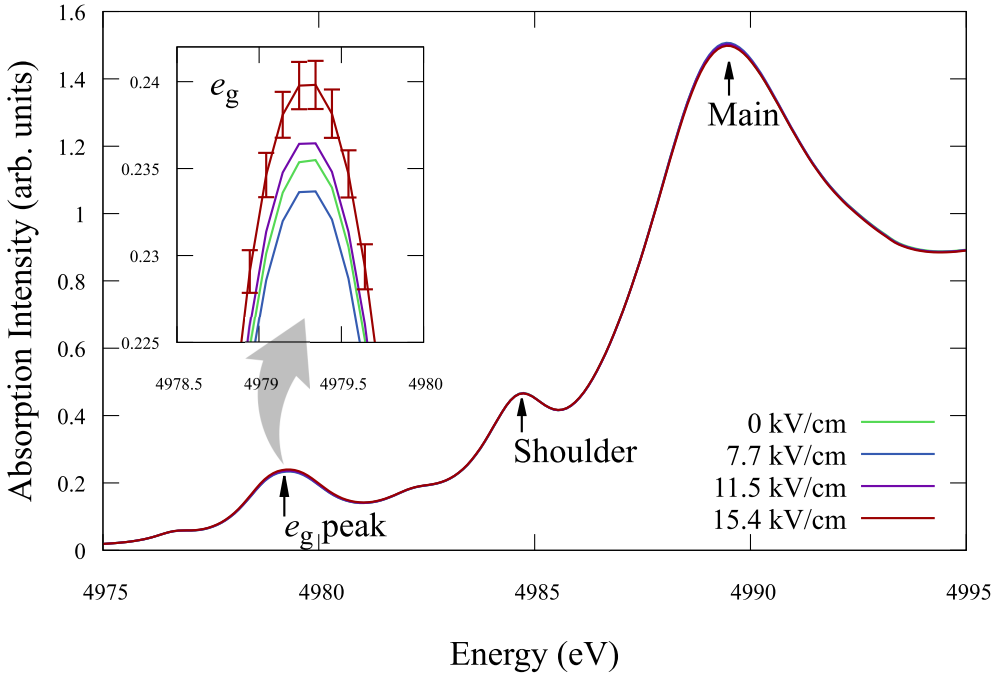

Fig. 5.17: Calculated Ti K-edge XANES spectra for obtained atomic configurations by RMC refinements.

Compared with the Ti K-edge experiments in Chapter 4, the e_g peak was successfully reproduced and included the effects of the electric fields, as shown in Fig. 5.18; however, it was difficult to reproduce the shoulder structure and main edge. The variation of the shoulder and main edge is approximately 5 times smaller than those of the e_g peaks, as presented in Fig. 4.12. For the reproduction of these two features, a multiple-edge fitting would be required to obtain well-reconstructed 3D structures, including the Ti–O bond. The RMC calculations use single Ba K-edge EXAFS and it is difficult to determine the Ti–O bond lengths and MSRD. Therefore, the obtained results are inconsistent with those obtained from the Ti K-edge XANES experimental spectra. Despite these limitations, the pronounced intensity variations of the e_g peak, simulated from the RMC configurations, reflect the enhancement of the Ti displacements under electric fields.

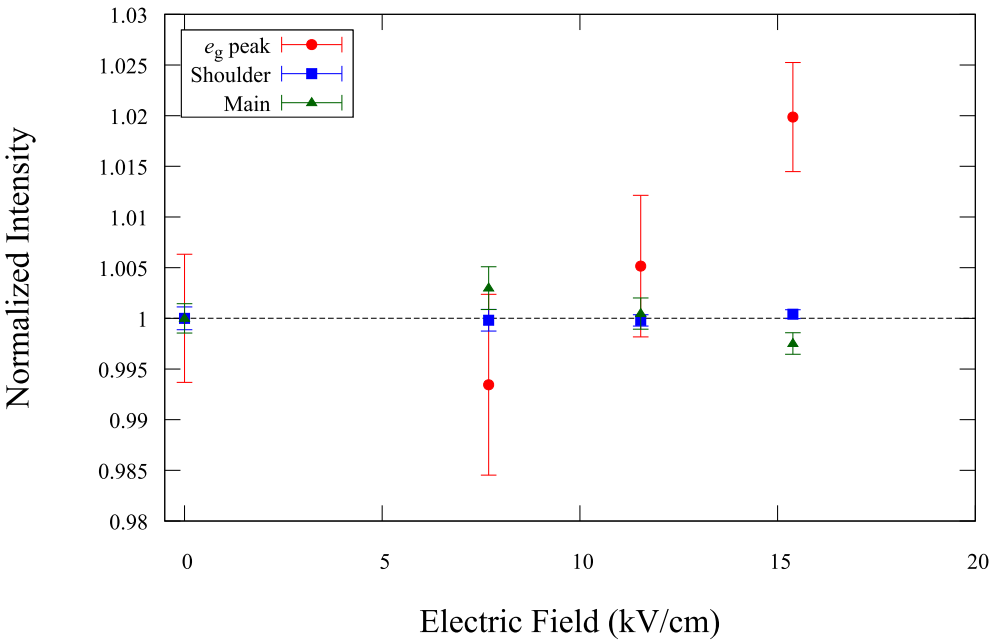

Fig. 5.18: Electric-field dependence of intensity of e_g peak, shoulder structure, and main peak obtained from simulated spectra. Intensity is normalized to the one without electric fields. Calculations averaged XANES spectra of 216 Ti-centered clusters at each electric field. Error bars indicate the standard deviations obtained from five RMC calculations for each point.

In the Chapter 4, the e_g peak intensity is proportional to the magnitude of applied electric fields. On the other hand, the Ti displacements relative to the Ba lattice are enhanced above 10 kV/cm and seems constants below the critical electric field, as can be seen in Fig. 5.15. This step-like curve would reflect the difference between two types of Ti displacements: the displacements relative to the center of the TiO_6 octahedra and the Ba lattice. In a simple point-charge model, where all atoms have nominal charges, the Ti and Ba atoms with positive charges are considered to move in the same direction under applied electric fields, while oxygen atoms with negative charges are to move in the opposite direction. The obtained structural model in this study is more complicated than this feature, as discussed later.

It was found that the e_g peak intensity simulated in Fig. 5.18 was strongly correlated to Ti–O bond lengths procedurally calculated from the RMC configurations. It is noted that the Ti–O bond length is indirect information because a single Ba K-edge EXAFS refinement has never contained the Ti–O bond information. Thus, the Ti and O relative displacement or off-centering are not shown here. However, this correlation is theoretically demonstrated [62] and clearly supported by the experimental stud-

ies [84, 85, 37]. Despite the difficulty of directly investigating the Ti–O relationship, the obtained RMC atomic configurations also reflect the local environment around Ti atoms. The detailed discussion and comparisons to Ti K-edge results are provided later in Chapter 6.

5.4 Conclusions

In summary, the Ti off-center displacements of $BaTiO_3$ under electric fields were investigated using Ba K-edge EXAFS measurements. The experimental EXAFS signals can be reproduced by using the structural model with tetragonal constants in the average structure. The enhancement of the Ti displacements relative to those in the absence of electric fields was ~ 0.5 pm, which is of the same order of magnitude as the lattice distortion of $BaTiO_3$ under electric fields. This study reports the first experimental and quantitative findings for Ti off-center displacements under electric fields. The analysis of the local structure, with small atomic displacements, provides a feasible opportunity to study dielectric/ferroelectric properties, including variations in the Curie temperature and relaxor behavior, induced by chemical substitutions in $BaTiO_3$ and other ferroelectric systems.

Chapter 6

Local structure determination using Ba K-edge and Ti K-edge results

6.1 Introduction

The local Ti displacements are investigated using Ti K-edge and Ba K-edge spectra in Chapter 4 and Chapter 5, respectively. Both results demonstrate the enhancement in the Ti displacements under electric fields. Unlike the quantitative analysis with Ba K-edge EXAFS spectra in Chapter 5, the Ti K-edge XANES spectra in Chapter 4 are qualitatively analyzed due to the difficulty to simplify the X-ray absorption formula in the XANES region. However, variations in the e_g peak intensity in Ti K-edge XANES spectra are comparable between experimental results shown in Chapter 4 and simulated results in Chapter 5. This consistency implies the potentiality for the quantitative local structural analysis using Ti K-edge XANES results.

Vedrinskii *et al.* proposed the relationship between the Ti off-center displacement and the e_g peak intensity [62]. Although this relationship is based on theoretical calculations, and utilized in the various studies for investigating Ti off-center displacements in many perovskite titanates [37, 86, 68, 84], those are limited to the qualitative analysis due to the lack of sufficient evidence for the methodology based on the experimental pre-edge features in Ti K-edge spectra. Therefore, it is essential to verify the relationship between the Ti displacement and the experimental e_g peak intensity.

In this chapter, a quantitative analysis based on Ti K-edge spectra is proposed. The obtained Ti displacement agrees well with the RMC results based on Ba K-edge EXAFS spectra, indicating the validity of the local structural

determination using Ti K-edge XANES spectra. The Ti K-edge XANES and Ba K-edge EXAFS results reflect Ti displacements from the center of TiO_6 octahedra and the Ba lattice, respectively. These two Ti displacements show different behaviors under applied electric fields. It is revealed that the coexistence of displacive and order-disorder characters is more reasonable than a simple displacive model. These findings and analytical schemes pave the way for understanding local structures related to macroscopic phenomena such as the electromechanical properties of ferroelectrics.

6.2 Experimental

6.2.1 XANES measurements

To obtain empirical parameters used in the Vedrinskii's equation (as described later), temperature-dependent Ti K-edge XANES spectra of a $BaTiO_3$ standard powder were measured on beamline BL-9A at KEK-PF. The incident X-ray energy was varied by using a Si(111) double-crystal monochromator. Higher-order harmonics reflected on the Si crystal were removed with a harmonic-rejection mirror. Ti K-edge spectra were collected in transmission mode at temperature range of 100 – 623 K. A liquid-helium cryostat and a loop electric heater were used for controlling the sample temperature in the low-temperature range of 100 – 296 K and in the high-temperature range of 300 – 623 K, respectively. The same powder sample was also measured on beamline BL-15A1 at KEK-PF for comparison with TR-XANES results in Chapter 4. The basic XAS data processing, including background subtraction and normalization, was performed using ATHENA program [87].

6.2.2 XANES pre-edge peak fitting

For extraction of the e_g peak intensity, the Ti K-edge spectra were fitted using several peak functions and an arctangent. An example of the fitting quality is presented in Fig. 6.1. Although there are several features including the small t_{2g} peak at 4967 eV, as mentioned in Section 4.3.1, four peaks are taken into account for simplicity: the e_g peak, a dipole transition at $\sim$ 4970 eV, the shoulder structure, and the main peak. For practical reasons, it is common to use Gaussian, Lorentzian, or pseudo-Voigt functions as peak functions to estimate pre-edge features in K-edge spectra of transition metals, as reported in several studies [88, 89, 90, 91, 92]. Using four pseudo-Voigt functions is a highly flexible model in this case because a pseudo-Voigt function is a weighted sum of Gaussian and Lorentzian functions, while the number

of fitting parameters is large compared to using four Gaussian/Lorentzian functions. It is noticed that Ti K-edge spectra of $BaTiO_3$ are represented well using three Gaussian peaks for e_g peak, the dipole transition, and the main peak, and a Lorentzian peak for the shoulder structure. Hence, this relatively simple model was employed instead of using four pseudo-Voigt functions.

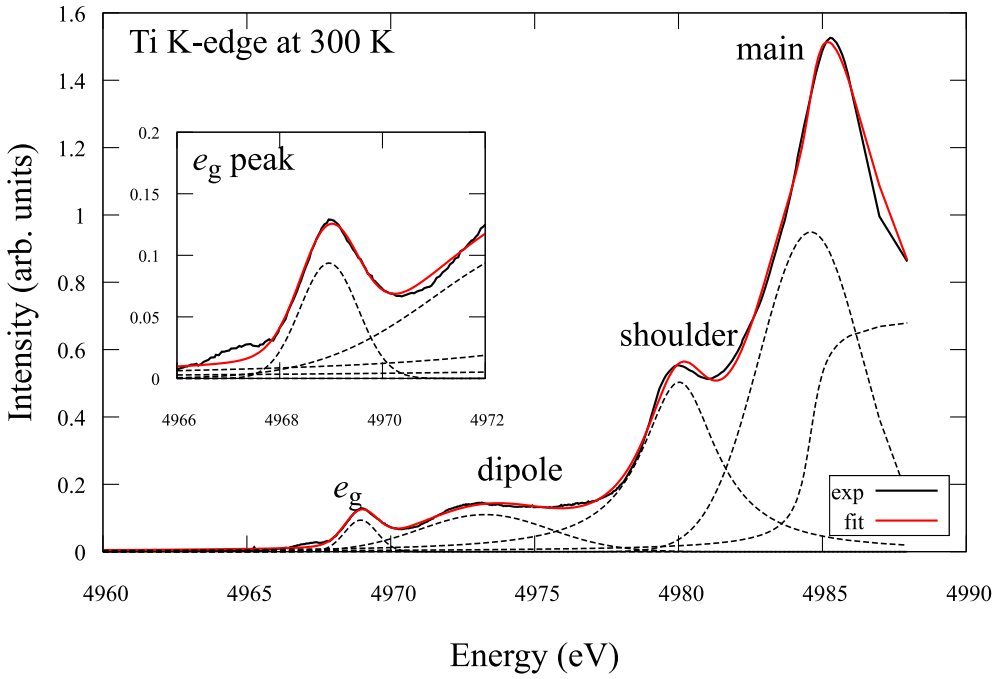

Fig. 6.1: Example of the fitting quality in Ti K-edge pre-edge features.

6.3 Results and discussion

6.3.1 Expression of the e_g peak intensity

The analytical expression on the e_g peak intensity I proposed by Vedrinskii *et al.* is [62]:

$$I = K \frac{\left[u(\mathrm{Ti}) - \frac{1}{2}\left(u(\mathrm{O}_i) + u(\mathrm{O}_j)\right)\right]^2}{\left[u(\mathrm{O}_i) - u(\mathrm{O}_j)\right]^{5.5}}, \tag{6.1}$$

where K is a coefficient independent of atomic positions, u is an atomic coordinate projected along the X-ray polarization vector $\vec{e}$, and O_i and O_j are the two nearest oxygen atoms around a Ti atom in the same O–Ti–O chain parallel to the direction $\vec{e}$. The e_g peak intensity observed in experiments is

expressed as Eq. (6.1) averaging over atomic thermal vibrations and static displacements.

It is reasonable to simplify Eq. (6.1) for the application to this study using some approximations. The denominator part $[u(\mathrm{O}_i) - u(\mathrm{O}_j)]^{5.5}$ is approximated by the lattice constants a or c, because variations of distances between two oxygen atoms caused by thermal vibrations are relatively small; The atomic distance between O–O in $BaTiO_3$ is around 4 Å and much larger than the usual thermal vibrations with an order of 0.1 Å [14, 16, 93]. The value of $[u(\mathrm{O}_i) - u(\mathrm{O}_j)]^{5.5}$ should close to the lattice constants within the error of $(0.1/4.0)^{5.5} < 10^{-6}\%$. Thus, the averaged value $\langle I \rangle$ can be obtained as the following equation:

$$\langle I \rangle = K \frac{\langle \Delta r^2 \rangle_c}{c^{5.5}} \cos^2\theta + \frac{K}{2} \frac{\langle \Delta r^2 \rangle_{ab}}{a^{5.5}} \sin^2\theta, \tag{6.2}$$

where θ is the angle between the X-ray polarization vector $\vec{e}$ and c-axis, $\langle \Delta r^2 \rangle_c$ and $\langle \Delta r^2 \rangle_{ab}$ are the c-axis and ab-plane components of the mean-square displacements of the Ti atom from the center of TiO_6 octahedra, respectively.

The simplified expression Eq. (6.2) allows to separate the static and dynamic disorder effects. The displacement vector $\Delta\vec{r}$ of a Ti atom from the TiO_6 octahedra can be decomposed into the static Ti off-center displacement $\vec{\delta_{\mathrm{Ti}}}$ and the dynamic displacement $\vec{d}$ due to atomic vibrations:

$$\Delta\vec{r} = \vec{\delta_{\mathrm{Ti}}} + \vec{d}. \tag{6.3}$$

The mean-square displacement $\langle \Delta r^2 \rangle$ is

$$\begin{aligned} \left\langle \Delta r^2 \right\rangle &= \left\langle (\vec{\delta_{\mathrm{Ti}}} + \vec{d}) \cdot (\vec{\delta_{\mathrm{Ti}}} + \vec{d}) \right\rangle \\ &= \left\langle \delta_{\mathrm{Ti}}^2 \right\rangle + 2\vec{\delta_{\mathrm{Ti}}} \cdot \left\langle \vec{d} \right\rangle + \left\langle d^2 \right\rangle \\ &\approx \left\langle \delta_{\mathrm{Ti}}^2 \right\rangle + \left\langle d^2 \right\rangle . \end{aligned} \tag{6.4}$$

The displacive model is employed here so that estimated Ti displacements can be compared to the Ba K-edge results shown in Chapter 5. In the tetragonal case, $\langle \delta_{\mathrm{Ti}}^2 \rangle_{ab} = 0$ because the static displacement of the Ti atom is along [001] direction. Therefore, one can obtain

$$\langle I \rangle = K \frac{\langle \delta_{\mathrm{Ti}}^2 \rangle}{c^{5.5}} \cos^2\theta + I_{vib}, \tag{6.5}$$

$$I_{vib} = K \frac{\langle d^2 \rangle_c}{c^{5.5}} \cos^2\theta + \frac{K}{2} \frac{\langle d^2 \rangle_{ab}}{a^{5.5}} \sin^2\theta. \tag{6.6}$$

The dynamical disorder effect $\langle d^2 \rangle$ is correlated to the mean-square displacement (MSD) of a single atom observed in diffraction measurements or the mean-square relative displacement (MSRD) between two atoms observed in EXAFS measurements. However, $\langle d^2 \rangle$ is not identical to the MSD and MSRD because $\langle d^2 \rangle$ is determined by the three-particle distributions involving O–Ti–O chains.

The validity of the equations was confirmed by simulated Ti K-edge spectra of $BaTiO_3$ with several static Ti displacements or dynamic disorder effects. MSRD values were employed instead of using $\langle d^2 \rangle$ for simple calculations. As can be seen in Fig. 6.2, both δ_{Ti} and MSRD values contribute to the enhancement in the e_{g} peak intensity. It was also found that another term $I_{on-center}$ was required because the e_{g} peak remains without Ti displacements and vibrations. Hence, the Eq. (6.5) should be modified:

$$\langle I \rangle = K \frac{\langle \delta_{\mathrm{Ti}}^2 \rangle}{c^{5.5}} \cos^2 \theta + I_{vib} + I_{on-center}. \tag{6.7}$$

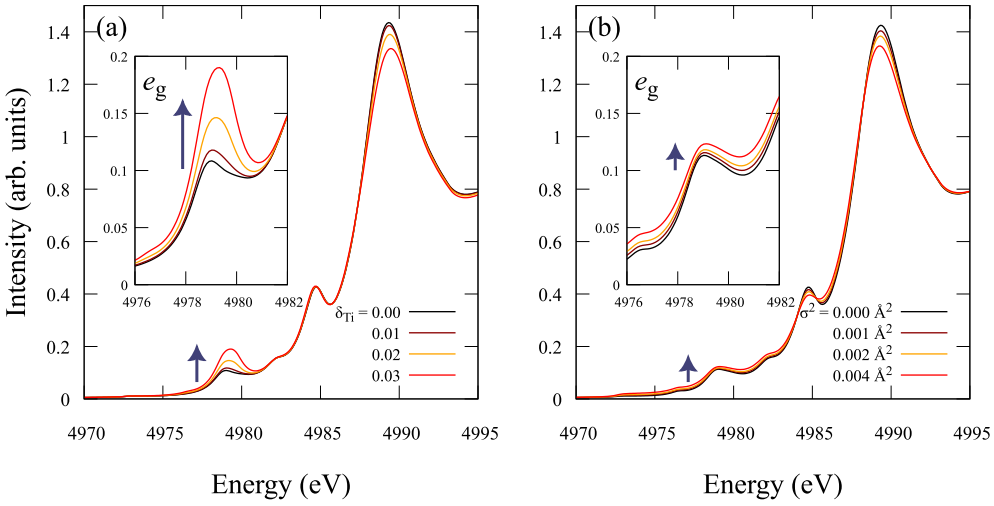

Fig. 6.2: (a) Calculated Ti K-edge spectra for various Ti off-center displacements without atomic vibrations. δ_{Ti} is the static Ti off-center displacement in the fractional coordinates. (b) Calculated Ti K-edge spectra for various atomic vibrations without Ti off-center displacements. σ^2 is the MSRD value for all atoms. Both spectra are simulated by FEFF9.6 with the same calculational options as presented in Section 4.3.3.

In polycrystalline materials, such as powder samples, the e_{g} peak intensity can be calculated by averaging over all possible orientations. Using the angle-integrated results $\int \cos^2 \theta \ d\Omega = 1/3$ and $\int \sin^2 \theta \ d\Omega = 2/3$, one can get the

expressions for polycrystalline materials:

$$\langle I \rangle = \frac{K}{3} \frac{\langle \delta^2_{\mathrm{Ti}} \rangle}{c^{5.5}} + I_{vib} + I_{on-center}, \tag{6.8}$$

$$I_{vib} = \frac{K}{3} \left[\frac{\langle d^2 \rangle_c}{c^{5.5}} + \frac{\langle d^2 \rangle_{ab}}{a^{5.5}} \right]. \tag{6.9}$$

6.3.2 Temperature dependence of e_g peak intensity

As a starting point for the analysis, the temperature dependence of Ti K-edge spectra is probed to investigate the static and dynamic disorder contributions to the e_g peak.

Fig. 6.3 shows the temperature-dependent Ti K-edge spectra of a standard powder sample. The e_g peak intensity decreases as temperature increases, indicating the diminished Ti off-center displacement. This qualitative trend is similar to those seen in the temperature dependence of lattice structures, obtained by diffraction study [14] and theoretical calculation [10]. It should be emphasized that the e_g peak remains even after the tetragonal-cubic phase transition. The distinct e_g peak in the cubic phase is due to I_{vib} and $I_{on-center}$ as described in Eq. (6.8). Therefore, the quantitative analysis of the temperature dependence enables to extract the static Ti displacements from the e_g peak intensity.

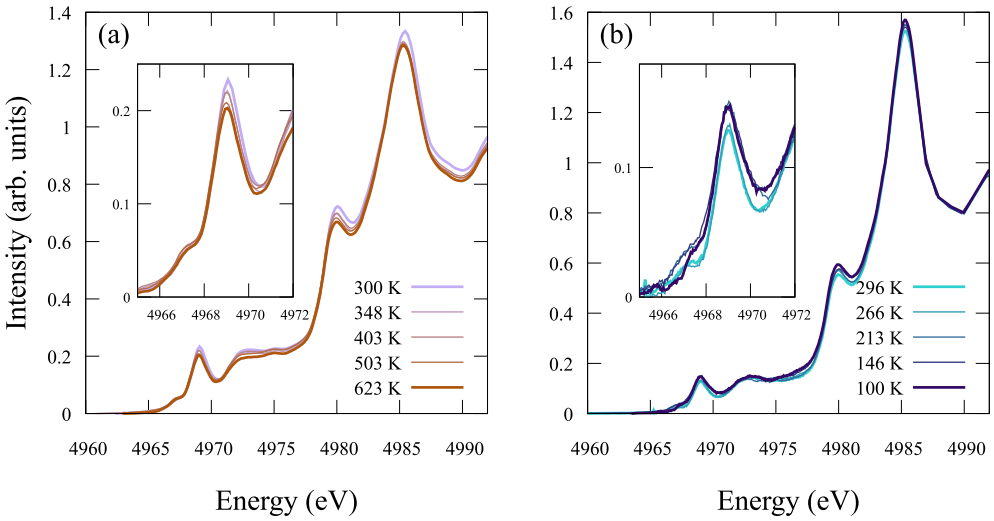

Fig. 6.3: Temperature dependence of Ti K-edge XANES spectra for a $BaTiO_3$ powder sample (a) in the high temperature range and (b) in the low temperature range.

Fig. 6.4 shows the temperature dependence of the e_g peak intensity obtained by fitting Ti K-edge spectra. The e_g peak intensity is normalized to unity at room temperature because of the difficulty in the direct comparison of spectra with different experimental settings. The low/high-temperature measurements using a cryostat/electrical heater produced different backgrounds on experimental results. The normalized e_g peak intensity monotonically decreases as temperature increases. A clear relationship between the phase transitions and the e_g peak intensity was found and the transition temperatures are consistent with those observed in the diffraction studies [94, 95, 14, 15, 16]. This consistency is quite reasonable because the Ti off-center displacement in the average (lattice) structure varies across the phase transition.

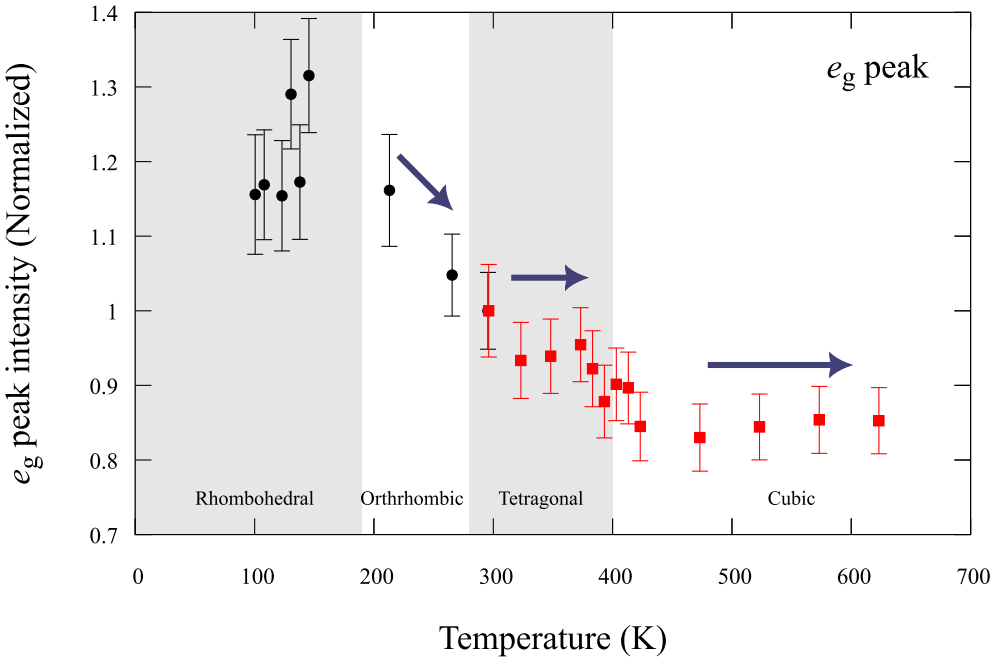

Fig. 6.4: Temperature dependence of the e_g peak intensity in a $BaTiO_3$ powder. The intensity is normalized to unity at room temperature.

Note that the e_g peak intensity remains constant in the cubic phase, where the Ti displacements $\langle \delta_{Ti}^2 \rangle$ can be regarded as zero. The constant intensity of the e_g peak implies the small contribution of dynamic disorder effects in Eq. (6.8). Provided that $I_{vib} + I_{on-center}$ is constant in this case, the local Ti off-center displacement can be estimated using the e_g peak intensity above

the Curie temperature T_C:

$$\langle I \rangle = \frac{K}{3} \frac{\langle \delta_{\mathrm{Ti}}^2 \rangle}{c^{5.5}} + \langle I(T > T_C) \rangle, \tag{6.10}$$

$$\langle I(T > T_C) \rangle \approx const. \tag{6.11}$$

6.3.3 Incident-angle dependence of e_g peak intensity

The e_g peak intensities depend on the incident angle of X-ray. This angle dependence produces the difference between single crystal and polycrystalline materials, as expressed in Eq. (6.7) and Eq. (6.8). Thus, it is necessary to investigate the incident-angle dependence of Ti K-edge spectra for applying the Vedrinskii's equation to the thin film sample used in Chapter 4.

Fig. 6.5a shows the incident-angle dependence of Ti K-edge spectra simulated by FEFF9.6. The e_g peak intensity decreases as the incident angle is close to 90°. This angle dependence is in good agreement with Eq. (6.2). As can be seen in Fig. 6.5b, the intensity can be fitted well with $\langle I \rangle = I_{\parallel} \cos^2\theta + I_{\perp} \sin^2\theta$, where $I_{\parallel}$ and $I_{\perp}$ are the e_g peak intensities at 0° and 90°, respectively.

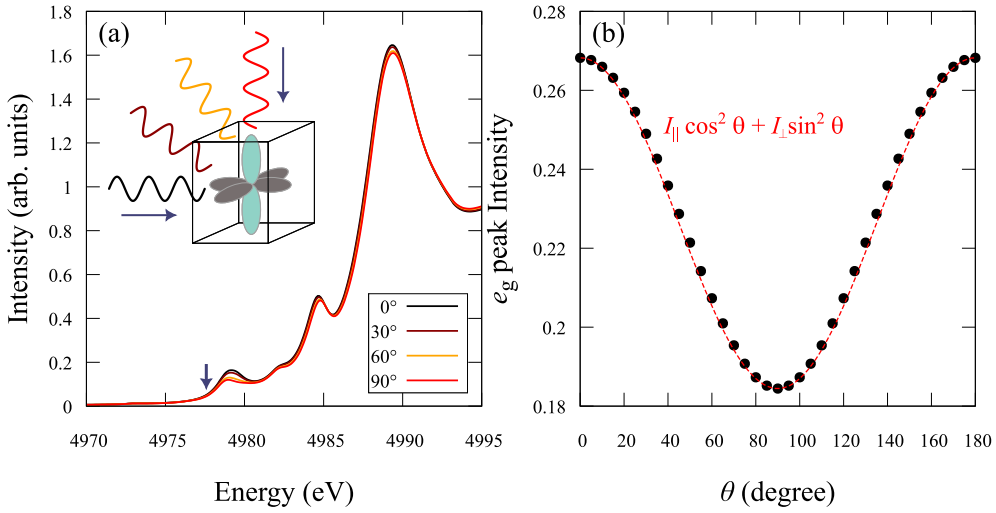

Fig. 6.5: (a) Simulated Ti K-edge spectra with several incident angles. (b) Angle dependence of the e_g peak intensity.

The same procedure as the FEFF calculations can be applied to the experimental results. Fig. 6.6 shows the incident-angle dependence of Ti K-edge spectra for the $BaTiO_3$ thin film. The qualitative trend is similar to that shown in Fig. 6.5. Therefore, $I_{\parallel}$ and $I_{\perp}$ can be obtained from the

curve fitting, which enables to estimate the angle-averaged e_g peak intensity and the Ti off-center displacement. The ratio of the e_g peak intensity in the powder and film sample at 45° was calculated using the obtained values $I_\parallel \approx 0.511$ and $I_\perp \approx 0.262$;

$$\begin{aligned}\frac{\langle I^{powder}\rangle}{\langle I^{film}\rangle} &= \frac{\int d\Omega \;\; I_\parallel \cos^2\theta + I_\perp \sin^2\theta}{I_\parallel \cos^2 45^\circ + I_\perp \sin^2 45^\circ} \\ &= \frac{\frac{1}{3}I_\parallel + \frac{2}{3}I_\perp}{\frac{1}{2}I_\parallel + \frac{1}{2}I_\perp} \\ &\approx 0.893.\end{aligned} \tag{6.12}$$

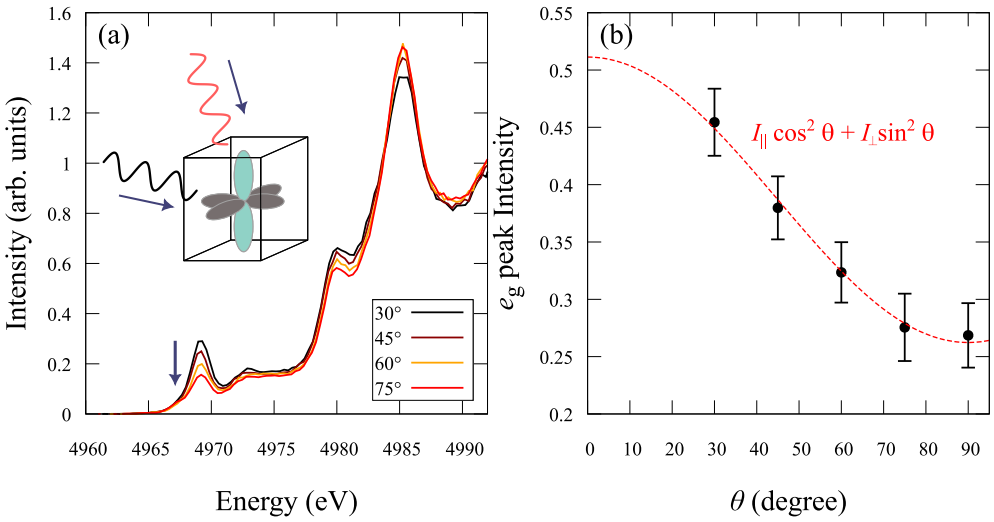

Fig. 6.6: (a) Experimental Ti K-edge spectra of the $BaTiO_3$ thin film, provided in Chapter 4, with several incident angles. (b) Angle dependence of the e_g peak intensity.

It should be noted that it is difficult to determine the angle between Ti displacements and the c-axis by using the incident-angle dependence of the e_g peak intensity. If the local structure is represented as the order-disorder model, the second term $\langle d^2\rangle_{ab}$ in Eq. (6.2) is large. However, the trend of the incident-angle dependence is unchanged in that case; The e_g peak intensity decreases as the incident angle increases. This behavior was verified by FEFF calculations, as shown in Fig. 6.7. Although it might be possible to estimate the Ti angle from the ratio of the intensities at 0° and 90°, the determination of the precise e_g peak intensity without any assumptions is challenging because the e_g peak remains even when Ti atoms are located in

the center of TiO_6 octahedra, as revealed in Fig. 6.2. The displacive model is employed in this section to investigate the local structure because the temperature-dependent e_g peak intensity indicates the displacive characters, and the Ti displacements can be detected by the RMC refinements with the displacive model in Chapter 5.

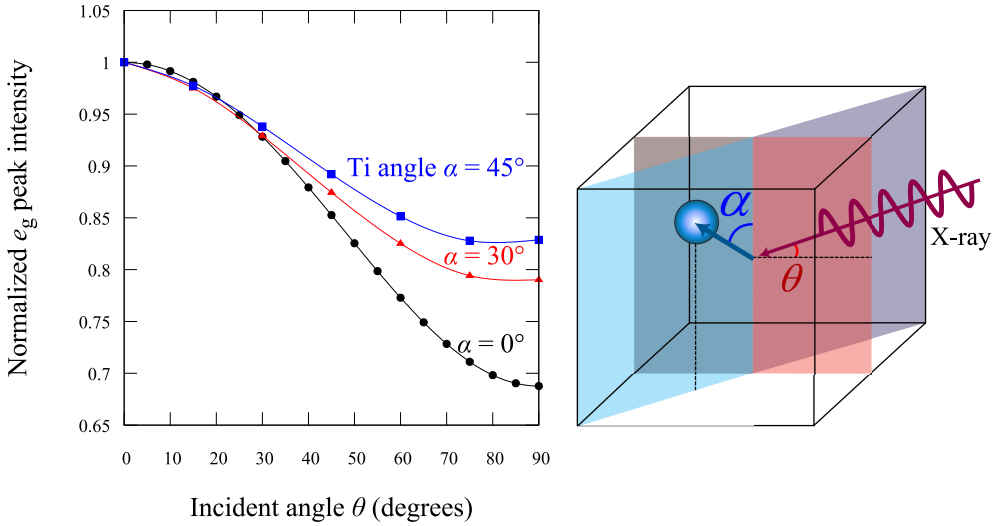

Fig. 6.7: The incident-angle dependence of the e_g peak intensity in calculated spectra for various angles between Ti displacements and the c-axis. The Ti atoms are rotated within the (110) plane. The magnitudes of Ti displacements are fixed. The electric polarization vectors of incident X-ray exist within the (100) plane.

6.3.4 Electric-field dependence of e_g peak intensity

The empirical parameters $\langle I(T > T_C)\rangle$ and $\langle I^{powder}\rangle / \langle I^{film}\rangle$ were obtained by temperature and incident-angle dependence of the e_g peak intensity, respectively. This information enables the estimation of the Ti off-center displacement under electric fields by using TR-XANES results as presented in Chapter 4.

Provided that parameters $\langle I(T > T_C)\rangle$ and K is the same for both samples, it gives

$$\frac{\langle \delta^2_{\mathrm{Ti}}{}^{film}\rangle}{\langle \delta^2_{\mathrm{Ti}}{}^{powder}\rangle} \approx \left(\frac{c^{powder}}{c^{film}}\right)^{5.5} \times \frac{0.893 \times \langle I^{film}\rangle - \langle I(T > T_C)\rangle}{\langle I^{powder}\rangle - \langle I(T > T_C)\rangle}. \tag{6.13}$$

To estimate the electric-field dependence of $\langle \delta^2_{\mathrm{Ti}}{}^{film}\rangle$, the empirical parameters obtained from experimental results; $\langle I^{powder}\rangle$ at room temperature is

unity as a reference, $\langle I(T > T_C)\rangle \approx 0.85$, as shown in Fig. 6.4, $c^{powder} = 4.037$ Å and $\left\langle \delta_{\mathrm{Ti}}^{2\,powder} \right\rangle = (0.137\ \text{Å})^2$, reported in the previous diffraction study [14], and $c^{film} = 4.136$ Å obtained in the diffraction result presented in Fig. 4.2.

The estimated Ti off-center displacement $\sqrt{\langle \delta_{\mathrm{Ti}}^{2\,film} \rangle}$ is provided in Fig. 6.8. It is clear that Ti displacements increase as the magnitudes of electric fields increase. Further, the responses of the Ti displacement to AC electric fields might imply a quite similar trend to a piezoelectric response, so-called a piezoelectric butterfly curve, or a response of lattice distortion as observed in the diffraction studies [96, 97]. Therefore, the Ti displacement as well as the lattice distortion synchronizes with the enhancement in the electric polarization induced by external electric fields. This result demonstrates the presence of displacive characters in $BaTiO_3$, describable by the enhancement in the local Ti displacement from the center of TiO_6 octahedra [10, 28, 29].

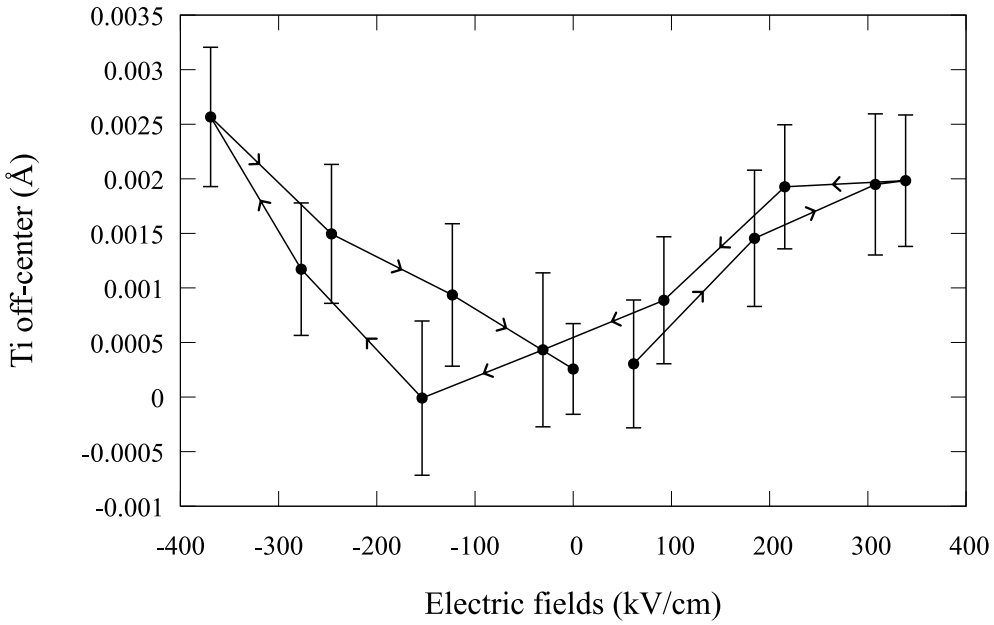

Fig. 6.8: Electric-field dependence of the Ti off-center displacement $\sqrt{\langle \delta_{\mathrm{Ti}}^2 \rangle}$ estimated from Ti K-edge results, shown in Chapter 4.

The enhancement in the Ti displacement at the maximum electric field was around 0.3 pm, which was of the same order as Ti displacement revealed in Chapter 5. Although the magnitude of electric fields applied to the thin film for Ti K-edge measurements is much larger than that to the single crystal for Ba K-edge measurements, it can be assumed that effective fields for both samples are comparable. The coercive field of $BaTiO_3$ samples commonly in-

creases as the sample thickness decreases due to the depolarization fields [98], the surface layer effects [99, 100] or the domain nuclei formation [101, 102]. This phenomenon can be also seen in the present case, as shown in Fig. 4.3 and Fig. 5.1. Despite the difference in coercive fields, external electric fields were large enough to obtain entire hysteresis loops in both Ti K-edge XANES and Ba K-edge EXAFS measurements, indicating intrinsic (lattice) contributions are comparable in the two samples. Hence, it is reasonable to observe the comparable enhancement of the Ti displacement in both measurements.

It should be noted that the Ti displacements obtained from Ti K-edge and Ba K-edge spectra are different. The e_{g} peaks in Ti K-edge spectra provide the Ti displacement relative to oxygen atoms, whereas the Ba K-edge EXAFS spectra provide the Ti displacement relative to the Ba lattice. Although a single Ba K-edge EXAFS refinement has never contained the Ti–O bond information, Ti–O bond lengths can be procedurally calculated as well as Ba–Ti bond lengths using the 6×6×6 $BaTiO_3$ supercell obtained by RMC refinements. These Ti–O bond lengths are indirect information, which was less reliable than Ba–Ti information. However, it was found that the Ti displacements relative to oxygen atoms was enhanced by ∼0.3 pm under electric fields, as shown in Fig. 6.9. This enhancement is consistent with Ti K-edge results, indicating that the RMC atomic configurations obtained in Chapter 5 also reflect the local environment around Ti atoms.

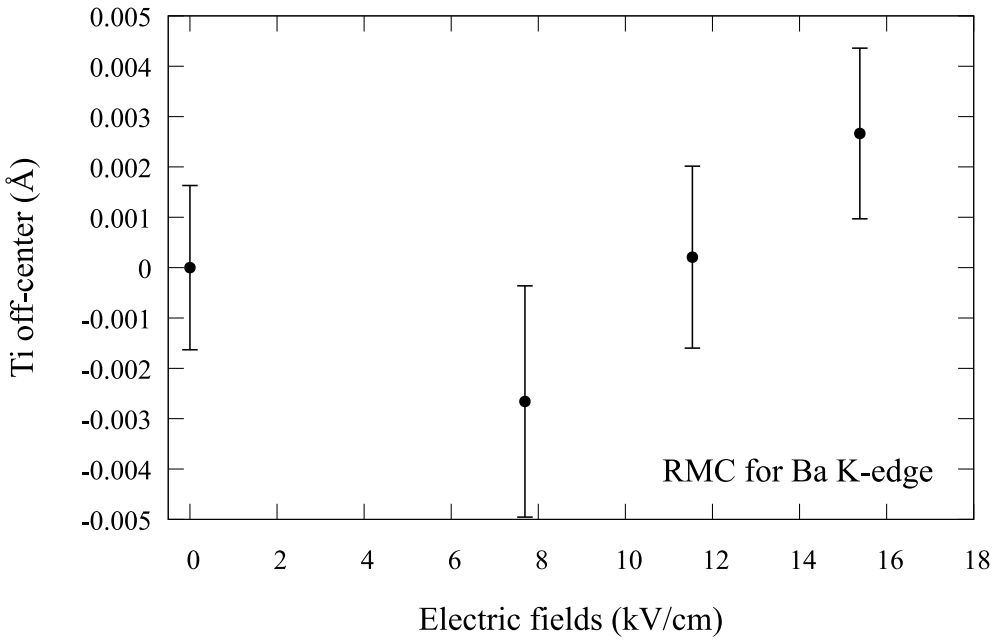

Fig. 6.9: Electric-field dependence of the Ti off-center displacement relative to oxygen atoms procedurally calculated from RMC results. This was 'indirect' information because Ba K-edge EXAFS has never contained the Ti–O bond information.

6.3.5 Responses of local structure under electric fields

In this section, an interpretation is provided for responses of the local structure and electronic states in $BaTiO_3$ under external electric fields. The obtained results in this study are compared to two local structural models: the displacive and order-disorder models, described in Section 2.4.

The Ti displacement relative to the center of the TiO_6 octahedra shows a similar trend with the displacement relative to the Ba lattice, as can be seen in Fig. 6.8, Fig. 6.9, and Fig. 5.15. However, the magnitudes of the enhancement are different between these two types of Ti displacements; the variations of the Ti displacement relative to oxygen atoms are smaller than those relative to Ba atoms. This small off-center displacement relative to TiO_6 octahedra indicates the necessity of order-disorder components in addition to displacive components.

Simple displacive model

Provided that all atoms were allowed to move only in the $\langle 001 \rangle$ direction, observed results in this study would contradict previous studies. In this case,

the difference between the two types of Ti displacements should be explained as the movement of entire TiO_6 octahedra alongside the partial displacement of Ti atoms in the octahedra, as shown in Fig. 6.10. These displacements are not intuitive responses under applied electric fields. If all constituent atoms were completely ionic, Ba and Ti ions with positive charges would have moved in a direction opposite to that of oxygen ions. Therefore, the existence of strong covalent bonds is required for the Ti and O movements in the same direction. Though Ti–O covalent bonds exist in $BaTiO_3$ [20], the Ba–O covalency is weak and inadequate to occur the entire movement of TiO_6 octahedra.

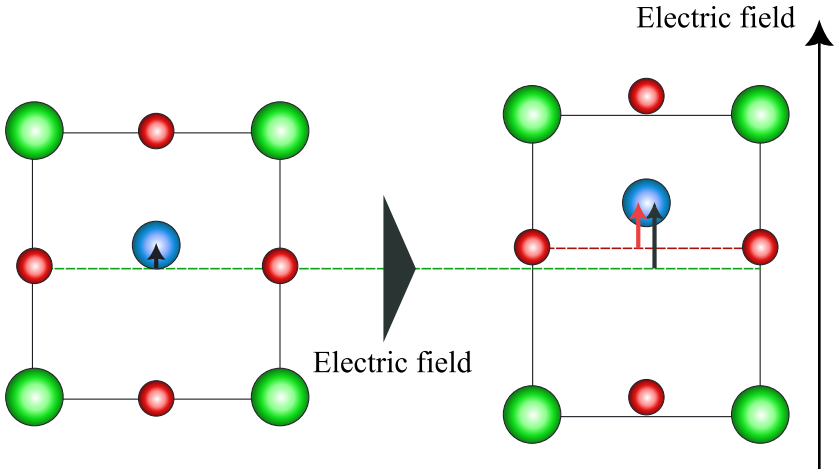

Fig. 6.10: Structural model of $BaTiO_3$ under electric fields based on the displacive model, where atoms move only in the $\langle 001 \rangle$ direction. Note this model is not proposed in this study; The entire movement of TiO_6 octahedra is hardly considered to occur in $BaTiO_3$.

This TiO_6 movement is related to the normal vibration mode called the Last mode in the displacive model [103]. The eigenvector of the Last mode is consistent with atomic displacements described in Fig. 6.10. Hence, the entire TiO_6 movement is realized if the Last mode is softened in ferroelectric phases. In $PbTiO_3$, where Pb–O covalent bonds exist as well as Ti–O covalent bonds [20], the soft mode is Last type [104, 105]. However, the soft mode in $BaTiO_3$ can be approximated by the Slater type [105], where Ti atoms move in the opposite direction to oxygen atoms [28]. It has been also revealed by X-ray diffraction measurements that $BaTiO_3$ and $PbTiO_3$ in the cubic phase show the Slater and the Last type of atomic movements under applied electric fields, respectively [106]. These previous reports disagree with the atomic displacements shown in Fig. 6.10. This structural model is based

on the assumption that atomic displacements are constrained in the $\langle 001 \rangle$ direction. It is required to modify the structural model by employing order-disorder characters.

Coexistence model of order-disorder and displacive characters

Although the enhancement in Ti displacements under electric fields was verified by XAS techniques, a simple displacive model leads to an unphysical structural model. It is essential to take into account the components of *ab*-plane movements as well as *c*-axis movements. These planar displacements correspond to local $\langle 111 \rangle$ displacements in the order-disorder model.

According to the order-disorder model, a local $\langle 111 \rangle$ Ti ordering is assumed yielding four-site distributions ($[111], [\bar{1}11], [1\bar{1}1]$, and $[\bar{1}\bar{1}1]$) in the tetragonal phase. While these site splittings are tiny and have never seen by conventional diffraction measurements, large mean square displacements $\langle u^2 \rangle$ (MSD) of Ti atoms or anisotropies of $\langle u^2 \rangle$ have been reported [14, 107]. Thus, order-disorder characters are assumed to appear in $\langle u^p \rangle$ ($p = 2, 3$, or more).

The spatial distributions of Ti atoms in obtained RMC results were analyzed to investigate order-disorder behaviors. Fig. 6.11a shows the ratio of $\langle u_c^2 \rangle / \langle u_{ab}^2 \rangle$ of Ti atoms, where $\langle u_c^2 \rangle$ and $\langle u_{ab}^2 \rangle$ are *c*-axis and *ab*-plane components of MSD, respectively. The ratio nearly equals one without applied electric fields, i.e., the Ti distributions are close to being spherical or cubical shapes. It was revealed that applied electric fields induced a reduction in the ratio. This reduction distinctly shows the presence of the *ab*-plane components, indicating the order-disorder characters in $BaTiO_3$. It is clear that these planar displacements of Ti atoms are linked to the rotation of Ti displacements; The angle between Ti locations and the *c*-axis increases under applied electric fields, as can be seen in Fig. 6.11b.

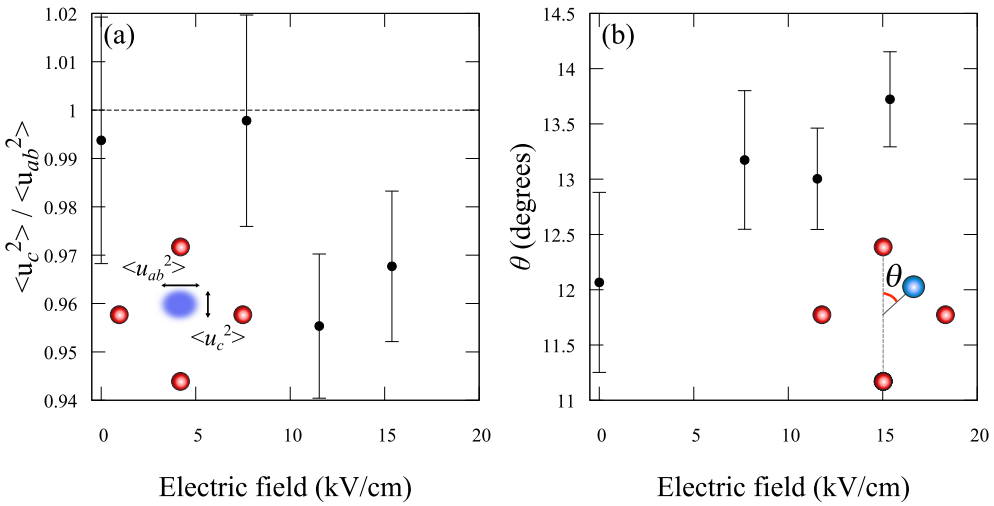

Fig. 6.11: Spatial distributions of Ti atoms in obtained RMC results. (a) Anisotropy of mean square displacements. (b) Average angle between Ti relative positions from the center of TiO_6 octahedra and c-axis.

The reduction in the ratio $\langle u_c^2 \rangle / \langle u_{ab}^2 \rangle$ implies the variation of the displacements in the ab-plane is larger than in the c-axis. One possible explanation for the large planar movements would be due to the anisotropy of interatomic forces acting on Ti atoms. The Raman spectroscopy is sensitive to interatomic forces because interatomic forces are strongly related to lattice dynamics. The distinct differences of vibration modes in ab-plane and c-axis are observed in the Raman spectroscopy. The dominant Raman peaks in ab-plane and c-axis corresponds to the A(TO) peak at $\sim$ 40 cm^{-1} and E(TO) peak at $\sim$ 270 cm^{-1}, respectively [108, 35, 109, 105]. These distinct differences in Raman shifts indicate a relatively weak interatomic force and a large oscillation amplitude in ab-plane.

Interatomic forces can be approximately estimated from the lattice vibration modes. In one of the simplest models, i.e., a harmonic oscillation of a quantum particle, the expected value of square displacements $\bar{u^2}$ is obtained by

$$\bar{u^2} = \frac{\hbar}{m\omega}\left(n + \frac{1}{2}\right), \tag{6.14}$$

where $\hbar$ is the Plank constant, m is the mass of the particle, ω is the frequency, and n is a quantum number. This oscillation is related to lattice dynamics and phonons in a crystalline material; The frequency ω corresponds to the Raman shifts. The quantum number n is determined by the Bose-

Einstein distributions. The average value $\langle u^2 \rangle$ of particles is as follows:

$$\langle u^2 \rangle = \frac{\hbar}{2m\omega} \coth \left[\frac{\hbar\omega}{2k_B T} \right] \tag{6.15}$$

$$\approx \begin{cases} \frac{\hbar}{m\omega} & \text{at low } T \\ \frac{k_B T}{m\omega^2} & \text{at high } T, \end{cases} \tag{6.16}$$

where k_B is the Boltzmann constant and T is the temperature. As can be seen in these expressions, the amplitude is large with low frequency. This estimation is rather simple to perform the detailed analysis of disorder effects. However, the relationship between EXAFS and Raman measurements is clearly revealed by theoretical and experimental reports [110, 111, 112, 113]. Thus, the anisotropy of MSD in $BaTiO_3$ is assumed to be correlated to the anisotropy of phonons: the small frequency of the E(TO) mode in *ab*-plane. It can be concluded that the comparative weak interatomic forces in *ab*-plane induce the enhancement of $\langle u_{ab}^2 \rangle$ in $BaTiO_3$ under electric fields.

Finally, the structural model under applied electric fields is proposed in Fig. 6.12. This model takes into account the coexistence of displacive and order-disorder characters. In this model, the average positions of Ti atoms move towards the nearest oxygen atoms like the Slater type of movements. Unlike the displacive model, applied electric fields induce the variations in Ti distributions, including $\langle 111 \rangle$ directions. Since $\langle 111 \rangle$ directions are parallel to Ba–Ti bonds, the enhancement in $\langle 111 \rangle$ components shorten Ba–Ti distances. On the other hand, $\langle 111 \rangle$ components have a relatively small influence on the magnitudes of the Ti displacements from the center of TiO_6 octahedra because these movements contain the rotation of local displacements. Hence, the variations in Ti displacements relative to O atoms are smaller than those to Ba atoms, as revealed in Fig. 6.8, Fig. 6.9, and Fig. 5.15. The atomic movements are also consistent with variations in the electronic states under applied electric fields, as observed in Fig. 4.12. The short Ba–Ti distances enhanced the Ba–Ti interaction, observed as the increase in the shoulder-structure intensity or anomalous Born effective charges of Ba. Note that the e_g peak intensity is enhanced under electric fields, indicating the displacive characters and enhancement in the covalency between Ti–O atoms. Without any displacive characters, the Ti–O distance would be constant. Therefore, the experimental results in this study support the coexistence of both displacive and order-disorder characters.

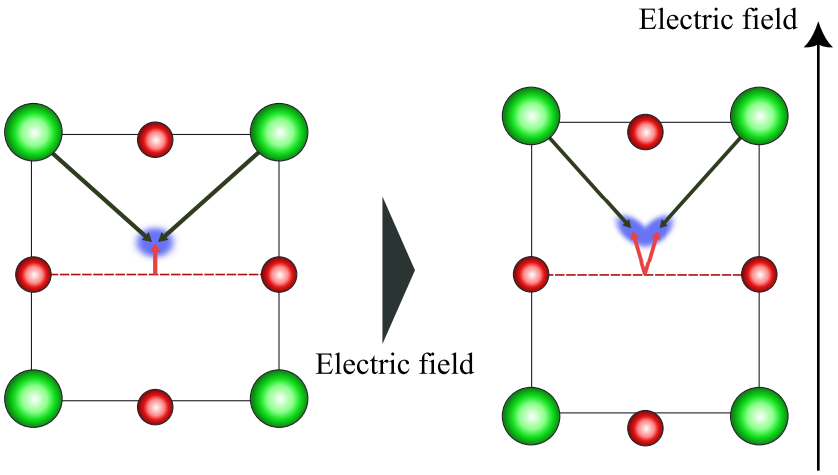

Fig. 6.12: Structural model of $BaTiO_3$ under electric fields taking into account the coexistence of displacive and order-disorder characters.

Conclusions

In summary, the electronic states and local structure in $BaTiO_3$ were investigated under electric fields using X-ray absorption spectroscopy. The electronic states were probed by the Ti K-edge XANES spectra, whereas the local structure information was obtained from the Ba K-edge EXAFS spectra. The XANES and EXAFS spectra have the capability providing a unified description of both structure and electronic states since the physical origin of XANES and EXAFS regions is identical except for the use of some approximations depending on the photon energy. In this study, the Ti K-edge XANES spectra were successfully reproduced by the structural model obtained by the RMC refinement using Ba K-edge EXAFS spectra.

In Chapter 4, the electronic states under triangular AC electric fields were observed by Ti K-edge TR-XANES measurements. Three characteristic features in Ti K-edge spectra were studied, namely the pre-edge e_g peak, shoulder structure, and main peak. Using structural model simulations, it was confirmed that Ti off-center displacements affect the increase in the e_g-peak intensity and decrease in the main peak intensity. Moreover, it was observed that the shoulder structure intensity was enhanced by the Ti off-center displacement and the lattice distortion. Both two structural variations should shorten the Ba–Ti atomic distance, resulting in the enhancement of the Ba contribution into Ti electronic states. Therefore, the Ba contribution to the ferroelectric property of $BaTiO_3$ via electronic hybridization is concluded experimentally using the novel TR-XAS technique.

In Chapter 5, the Ti off-center displacements relative to Ba atoms under electric fields were observed using Ba K-edge EXAFS measurements combined with RMC calculations. The RMC refinements with tetragonal constraints revealed the enhancement in the local Ti displacement under Electric fields. This enhancement was ~ 0.5 pm when compared without electric fields, which is the same order of the magnitude as the lattice distortion of $BaTiO_3$ under electric fields, observed in the previous diffraction measurements [18, 19]. This finding provides unprecedented quantitative and experimental evidence for the enhancement of Ti off-center displacements.

Further, simulated Ti K-edge spectra calculated from the obtained atomic configurations showed the enhancement of the e_g peak intensity. Although the RMC calculations utilized single Ba K-edge EXAFS, the atomic configurations also reflected the local environment around Ti atoms.

In Chapter 6, the local Ti displacements were investigated based on both Ti K-edge and Ba K-edge spectra. Quantitative analysis for Ti off-center displacement relative to oxygen atoms was performed using experimental Ti K-edge spectra. This analysis is based on the relationship between the Ti off-center displacement and the e_g peak intensity, as observed in theoretical spectra [62]. The obtained Ti displacement agrees well with the RMC results, indicating the validity of the local structural determination using Ti K-edge XANES spectra. These results separately evaluated the magnitudes of local Ti displacements within the TiO_6 octahedra and relative to the Ba lattice. It is concluded that applied electric fields induce the variations in the spatial Ti distributions. The obtained results in the present study demonstrate that the coexistence of both displacive and order-disorder characters plays an important role in the ferroelectric behavior in $BaTiO_3$.

These findings and analytical schemes pave the way for understanding local structures and electronic states related to macroscopic phenomena and dielectric/ferroelectric properties, including variations in the Curie temperature and relaxor behavior, induced by chemical substitutions in $BaTiO_3$ and other ferroelectric systems.

Acknowledgements

I would like to express sincere gratitude to my supervisor Prof. Nobuo Nakajima who supported, motivated, and guided me during the whole time of my research and daily life at the university. Discussions and daily conservations with him are quite beneficial for me. He was also an instructor when I was an undergraduate student, helping me with daily campus life and advising me on college course selections. He has taught and given me a lot of things including common knowledge in academic fields since I enrolled in college. I am really happy to participate in his research as a member of the laboratory.

I also thank Dr. Naoki Ishimatu who supported and inspired my research. His useful advice, comments, and suggestions always drive the progress of my work. I would like to express my special thanks to Prof. Hiroshi Maruyama, who provided me first steps in science. He greatly supported me when I started work at the laboratory during my Bachelor studies.

I sincerely appreciate the support from Prof. Takumi Hasegawa. He kindly taught me the interpretation of Raman spectra. It enabled me to discuss a more realistic model than a simple displacive model in Chapter 6.

I really love the great working atmosphere in our laboratory. I enjoy daily activities and experiments at synchrotron beamlines. I would acknowledge my colleagues for the atmosphere they created.

I would also like to thank Prof. Andris Anspoks. He was also a supervisor when I stayed at the Institute of Solid State Physics, Latvia University. Thanks to his kind support, I was able to learn practical knowledge of EXAFS analysis including traditional approaches and RMC calculations. After the one-month stay, he held frequent meetings and always encouraged me to make progress in my study. I sincerely appreciate his impressive advice and comments. I was honored to take part in his project as one of the co-authors of published articles.

I wish to give special thanks to Prof. Janis Timoshenko for his expert knowledge of the RMC algorithm implemented in the EvAX software. The EvAX codes he created are excellent, enabling me to analyze Ba K-edge spectra in $BaTiO_3$.

I would like to express my gratitude to Prof. Shintaro Yasui and Dr. Sou Yasuhara for their sample preparations. Thanks to the well-qualified thin film samples, I have obtained the electric-field-dependent spectra with sufficient accuracy in Chapter 4. Prof. Desheng Fu also provided good powder samples including (Ba, Ca)TiO_3, presented in Fig. 4.10. I really appreciate his technical support and beneficial comments on dielectric materials.

I wish to thank the beamline scientists from synchrotron facilities: KEK-PF and SPring-8. Dr. Junichi Adachi, Dr. Hiroaki Nitani, and Dr. Yasuo Takeichi helped me a lot to set up the time-resolved measurement in Chapter 4. Dr. Hitoshi Osawa, Dr. Kazuo Kato, and Dr. Toshiaki Ina supported me to measure Ba K-edge spectra under applied electric fields. They maintained the beamline equipment in excellent conditions and provided me with beneficial information.

This research was performed under the approval of the Photon Factory Program Advisory Committee (PF-PAC; Contract Numbers 2015G580, 2017G587, and 2019G614) and the SPring-8 Program Advisory Committee (2018B1659 and 2019B1450). These works were financially supported by JSPS KAKENHI Grant Numbers 18H01153, 19H02426, 22H01157, and 18K19126, and JST SPRING Grant Number JPMJSP2132. The experiment for measuring spectra in Fig. 4.9 was performed on beamline BM26A (proposal MA 2731) at the European Synchrotron Radiation Facility (ESRF), Grenoble, France.

The internship program at the Institute in Latvia was financially supported by the MURATA Science Foundation Grant. The RMC calculations were performed using the Latvian SuperCluster (LASC) system, installed at the Institute of Solid State Physics of the University of Latvia. The Institute of Solid State Physics, University of Latvia at the Center of Excellence has received funding from the European Union's Horizon 2020 Framework Programme H2020-WIDESPREAD-01-2016-2017-TeamingPhase2 under grant agreement No. 739508, project CAMART^2.

Finally, I express many thanks to my family for their appreciation and cooperation throughout my study and daily life.

Bibliography

[1] S. Suasmoro, S. Pratapa, D. Hartanto, D. Setyoko, U. Dani, The characterization of mixed titanate Ba1-xSrxTiO3 phase formation from oxalate coprecipitated precursor, Journal of the European Ceramic Society 20 (3) (2000) 309–314. doi:10.1016/S0955-2219(99)00143-0.

[2] J.-H. Jeon, Effect of SrTiO3 concentration and sintering temperature on microstructure and dielectric constant of Ba1-xSrxTiO3, Journal of the European Ceramic Society 24 (6) (2004) 1045–1048, electroceramics VIII. doi:10.1016/S0955-2219(03)00385-6.

[3] A. Ianculescu, D. Berger, M. Viviani, C. E. Ciomaga, L. Mitoseriu, E. Vasile, N. Drăgan, D. Crişan, Investigation of Ba1-xSrxTiO3 ceramics prepared from powders synthesized by the modified pechini route, Journal of the European Ceramic Society 27 (13) (2007) 3655–3658, refereed Reports ELECTROCERAMICS X 2006. doi:10.1016/j.jeurceramsoc.2007.02.017.

[4] L. Zhang, O. P. Thakur, A. Feteira, G. M. Keith, A. G. Mould, D. C. Sinclair, A. R. West, Comment on the use of calcium as a dopant in X8R BaTiO3-based ceramics, Applied Physics Letters 90 (14) (2007) 142914. doi:10.1063/1.2720305.

[5] R. Moussi, A. Bougoffa, A. Trabelsi, E. Dhahri, M.P.F.Graça, M. A. Valente, R. Barille, Effect of Sr-substitution on structure, dielectric relaxation and conduction phenomenon of BaTiO3 perovskite material, Journal of Materials Science: Materials in Electronics 32 (9) (2021) 11453–11466. doi:10.1007/s10854-021-05604-3.

[6] P. Victor, R. Ranjith, S. B. Krupanidhi, Normal ferroelectric to relaxor behavior in laser ablated Ca-doped barium titanate thin films, Journal of Applied Physics 94 (12) (2003) 7702–7709. doi:10.1063/1.1618914.

[7] N. Baskaran, H. Chang, Effect of Sn doping on the phase transformation properties of ferroelectric BaTiO3, Journal of Materials Science: Materials in Electronics 12 (9) (2001) 527–531. doi:10.1023/A:1012453526652.

[8] D. Xu, W. Li, L. Wang, W. Wang, W. Cao, W. Fei, Large piezoelectric properties induced by doping ionic pairs in BaTiO3 ceramics, Acta Materialia 79 (2014) 84–92. doi:10.1016/j.actamat.2014.07.023.

[9] G. M. Osoro, D. Bregiroux, M. P. Thi, F. Levassort, Structural and piezoelectric properties evolution induced by cobalt doping and cobalt/niobium co-doping in BaTiO3, Materials Letters 166 (2016) 259–262. doi:10.1016/j.matlet.2015.12.086.

[10] A. Devonshire, XCVI. theory of barium titanate, The London, Edinburgh, and Dublin Philosophical Magazine and Journal of Science 40 (309) (1949) 1040–1063. doi:10.1080/14786444908561372.

[11] E. Wainer, A. Salomon, Titanium alloy manufacturing co, Electr. Rep 8 (9) (1942).

[12] B. Wul, J. Goldman, Cr acad, Sci URSS 46 (1945) 139.

[13] T. Ogawa, Busseiron Kenkyu (6) (1947).

[14] G. H. Kwei, A. C. Lawson, S. J. L. Billinge, S. W. Cheong, Structures of the ferroelectric phases of barium titanate, The Journal of Physical Chemistry 97 (10) (1993) 2368–2377. doi:10.1021/j100112a043.

[15] S. Pradhan, G. S. Roy, Study the crystal structure and phase transition of BaTiO3 - a pervoskite, 2013.

[16] T. Nakatani, A. Yoshiasa, A. Nakatsuka, T. Hiratoko, T. Mashimo, M. Okube, S. Sasaki, Variable-temperature single-crystal X-ray diffraction study of tetragonal and cubic perovskite-type barium titanate phases, Acta Crystallographica Section B 72 (1) (2016) 151–159. doi:10.1107/S2052520615022544.

[17] W. J. Merz, The electric and optical behavior of batio$_3$ single-domain crystals, Phys. Rev. 76 (1949) 1221–1225. doi:10.1103/PhysRev.76.1221.

[18] R. Tazaki, D. Fu, M. Itoh, M. Daimon, S. ya Koshihara, Lattice distortion under an electric field in BaTiO3 piezoelectric single crystal, Journal of Physics: Condensed Matter 21 (21) (2009) 215903. doi:10.1088/0953-8984/21/21/215903.

[19] C. Moriyoshi, S. Hiramoto, H. Ohkubo, Y. Kuroiwa, H. Osawa, K. Sugimoto, S. Kimura, M. Takata, Y. Kitanaka, Y. Noguchi, M. Miyayama, Synchrotron radiation study on time-resolved tetragonal lattice strain of BaTiO3 under electric field, Japanese Journal of Applied Physics 50 (9) (2011) 09NE05. doi:10.1143/jjap.50.09ne05.

[20] Y. Kuroiwa, S. Aoyagi, A. Sawada, J. Harada, E. Nishibori, M. Takata, M. Sakata, Evidence for Pb-O covalency in tetragonal PbTiO3, Phys. Rev. Lett. 87 (2001) 217601. doi:10.1103/PhysRevLett.87.217601.

[21] R. E. Cohen, H. Krakauer, Electronic structure studies of the differences in ferroelectric behavior of BaTiO3 and PbTiO3, Ferroelectrics 136 (1) (1992) 65–83. doi:10.1080/00150199208016067.

[22] R. E. Cohen, Origin of ferroelectricity in perovskite oxides, Nature 358 (6382) (1992) 136–138. doi:10.1038/358136a0.

[23] L. L. Boyer, M. J. Mehl, J. W. Flocken, J. R. Hardy, Ab initio calculations of the effect of non-rigid ions on the statics and dynamics of oxides, Japanese Journal of Applied Physics 24 (S2) (1985) 204. doi:10.7567/JJAPS.24S2.204.

[24] W. Zhong, R. D. King-Smith, D. Vanderbilt, Giant lo-to splittings in perovskite ferroelectrics, Phys. Rev. Lett. 72 (1994) 3618–3621. doi:10.1103/PhysRevLett.72.3618.

[25] P. Ghosez, X. Gonze, P. Lambin, J.-P. Michenaud, Born effective charges of barium titanate: Band-by-band decomposition and sensitivity to structural features, Phys. Rev. B 51 (1995) 6765–6768. doi:10.1103/PhysRevB.51.6765.

[26] P. Ghosez, J.-P. Michenaud, X. Gonze, Dynamical atomic charges: The case of ABO3 compounds, Phys. Rev. B 58 (1998) 6224–6240. doi:10.1103/PhysRevB.58.6224.

[27] N. Sai, K. M. Rabe, D. Vanderbilt, Theory of structural response to macroscopic electric fields in ferroelectric systems, Phys. Rev. B 66 (2002) 104108. doi:10.1103/PhysRevB.66.104108.

[28] J. C. Slater, The lorentz correction in barium titanate, Phys. Rev. 78 (1950) 748–761. doi:10.1103/PhysRev.78.748.

[29] W. Cochran, Crystal stability and the theory of ferroelectricity, Advances in Physics 9 (36) (1960) 387–423. doi:10.1080/00018736000101229.

[30] K. Itoh, L. Z. Zeng, E. Nakamura, N. Mishima, Crystal structure of BaTiO3 in the cubic phase, Ferroelectrics 63 (1) (1985) 29–37. doi:10.1080/00150198508221381.

[31] H. Takahasi, A note on the theory of barium titanate, Journal of the Physical Society of Japan 16 (9) (1961) 1685–1689. doi:10.1143/JPSJ.16.1685.

[32] R. Comes, M. Lambert, A. Guinier, The chain structure of BaTiO3 and KNbO3, Solid State Communications 6 (10) (1968) 715–719. doi:10.1016/0038-1098(68)90571-1.

[33] G. Shirane, B. C. Frazer, V. J. Minkiewicz, J. A. Leake, A. Linz, Soft optic modes in barium titanate, Phys. Rev. Lett. 19 (1967) 234–235. doi:10.1103/PhysRevLett.19.234.

[34] J. Harada, J. D. Axe, G. Shirane, Neutron-scattering study of soft modes in cubic BaTiO3, Phys. Rev. B 4 (1971) 155–162. doi:10.1103/PhysRevB.4.155.

[35] M. DiDomenico, S. H. Wemple, S. P. S. Porto, R. P. Bauman, Raman spectrum of single-domain BaTiO3, Phys. Rev. 174 (1968) 522–530. doi:10.1103/PhysRev.174.522.

[36] K. A. Müller, W. Berlinger, Microscopic probing of order-disorder versus displacive behavior in BaTiO3 by Fe3+ epr, Phys. Rev. B 34 (1986) 6130–6136. doi:10.1103/PhysRevB.34.6130.

[37] B. Ravel, E. A. Stern, R. I. Vedrinskii, V. Kraizman, Local structure and the phase transitions of BaTiO3, Ferroelectrics 206 (1) (1998) 407–430. doi:10.1080/00150199808009173.

[38] A. M. Pugachev, V. I. Kovalevskii, N. V. Surovtsev, S. Kojima, S. A. Prosandeev, I. P. Raevski, S. I. Raevskaya, Broken local symmetry in paraelectric BaTiO3 proved by second harmonic generation, Phys. Rev. Lett. 108 (2012) 247601. doi:10.1103/PhysRevLett.108.247601.

[39] I. Levin, V. Krayzman, J. C. Woicik, Local structure in perovskite (Ba,Sr)TiO3: Reverse monte carlo refinements from multiple measurement techniques, Phys. Rev. B 89 (2) (2014) 024106. doi:10.1103/PhysRevB.89.024106.

[40] K. Tsuda, R. Sano, M. Tanaka, Nanoscale local structures of rhombohedral symmetry in the orthorhombic and tetragonal phases of BaTiO3 studied by convergent-beam electron diffraction, Phys. Rev. B 86 (2012) 214106. doi:10.1103/PhysRevB.86.214106.

[41] K. Tsuda, A. Yasuhara, M. Tanaka, Two-dimensional mapping of polarizations of rhombohedral nanostructures in the tetragonal phase of BaTiO3 by the combined use of the scanning transmission electron microscopy and convergent-beam electron diffraction methods, Applied Physics Letters 103 (8) (2013) 082908. doi:10.1063/1.4819221.

[42] B. t. Zalar, V. V. Laguta, R. Blinc, Nmr evidence for the coexistence of order-disorder and displacive components in barium titanate, Phys. Rev. Lett. 90 (2003) 037601. doi:10.1103/PhysRevLett.90.037601.

[43] E. A. Stern, Character of order-disorder and displacive components in barium titanate, Phys. Rev. Lett. 93 (2004) 037601. doi:10.1103/PhysRevLett.93.037601.

[44] Y. Qi, S. Liu, I. Grinberg, A. M. Rappe, Atomistic description for temperature-driven phase transitions in BaTiO3, Phys. Rev. B 94 (2016) 134308. doi:10.1103/PhysRevB.94.134308.

[45] J. J. Rehr, J. J. Kas, F. D. Vila, M. P. Prange, K. Jorissen, Parameter-free calculations of X-ray spectra with FEFF9, Phys. Chem. Chem. Phys. 12 (2010) 5503–5513. doi:10.1039/B926434E.

[46] Y. Joly, X-ray absorption near-edge structure calculations beyond the muffin-tin approximation, Phys. Rev. B 63 (2001) 125120. doi:10.1103/PhysRevB.63.125120.

[47] O. Bunău, Y. Joly, Self-consistent aspects of x-ray absorption calculations, Journal of Physics: Condensed Matter 21 (34) (2009) 345501. doi:10.1088/0953-8984/21/34/345501.

[48] R. L. McGreevy, L. Pusztai, Reverse monte carlo simulation: A new technique for the determination of disordered structures, Molecular Simulation 1 (6) (1988) 359–367. doi:10.1080/08927028808080958.

[49] M. Deguchi, N. Nakajima, K. Kawakami, N. Ishimatsu, H. Maruyama, C. Moriyoshi, Y. Kuroiwa, S. Nozawa, K. Ishiji, T. Iwazumi, Luminescence mechanism of (Pr, Al)-doped SrTiO3 fine particles investigated by x-ray absorption spectroscopy, Phys. Rev. B 78 (2008) 073103. doi:10.1103/PhysRevB.78.073103.

[50] N. Nakajima, M. Deguchi, H. Maruyama, K. Ishiji, Y. Tezuka, X-ray spectroscopic study on photoluminescence properties of red phosphor SrTiO3:Pr3+,Al, Japanese Journal of Applied Physics 49 (9) (2010) 09ME04. doi:10.1143/jjap.49.09me04.

[51] S. Kawakami, N. Nakajima, T. Takigawa, M. Nakatake, H. Maruyama, Y. Tezuka, T. Iwazumi, UV-induced change in the electronic structure of SrTiO3 at low temperature probed by resonant X-ray emission spectroscopy, Journal of the Physical Society of Japan 82 (5) (2013) 053701. doi:10.7566/JPSJ.82.053701.

[52] S. Kawakami, N. Nakajima, M. Nakatake, N. Kawamura, M. Mizumaki, H. Maruyama, Mechanism of intrinsic dipole moment induction in quantum paraelectric SrTiO3, Japanese Journal of Applied Physics 54 (10S) (2015) 10NC03. doi:10.7567/jjap.54.10nc03.

[53] C. Lu, C. Temba, N. Nakajima, S. Kawakami, N. Ishimatsu, H. Maruyama, Isotropic shrinkage of the oxygen octahedron in SrTiO3 under uniaxial pressure, Journal of Physics: Condensed Matter 29 (39) (2017) 395502. doi:10.1088/1361-648x/aa7ec6.

[54] A. Anspoks, C. Marini, T. Miyanaga, B. Joseph, A. Kuzmin, J. Purans, J. Timoshenko, A. Bussmann-Holder, Local structure of A-atom in ABO3 perovskites studies by RMC-EXAFS, Radiation Physics and Chemistry 175 (2020) 108072, 17th International Conference on X-ray Absorption Fine Structure - XAFS2018. doi:https://doi.org/10.1016/j.radphyschem.2018.11.026.

[55] R. H. Buttner, E. N. Maslen, Structural parameters and electron difference density in BaTiO3, Acta Crystallographica Section B 48 (6) (1992) 764–769. doi:10.1107/S010876819200510X.

[56] K. J. Choi, M. Biegalski, Y. L. Li, A. Sharan, J. Schubert, R. Uecker, P. Reiche, Y. B. Chen, X. Q. Pan, V. Gopalan, L.-Q. Chen, D. G. Schlom, C. B. Eom, Enhancement of ferroelectricity in strained BaTiO3 thin films, Science 306 (5698) (2004) 1005–1009. doi:10.1126/science.1103218.

[57] M. Tyunina, O. Pacherova, J. Peräntie, M. Savinov, M. Jelinek, H. Jantunen, A. Dejneka, Perovskite ferroelectric tuned by thermal strain, Scientific reports 9 (1) (2019) 3677. doi:10.1038/s41598-019-40260-y.

[58] N. Setter, D. Damjanovic, L. Eng, G. Fox, S. Gevorgian, S. Hong, A. Kingon, H. Kohlstedt, N. Y. Park, G. B. Stephenson, I. Stolitchnov, A. K. Taganstev, D. V. Taylor, T. Yamada, S. Streiffer, Ferroelectric thin films: Review of materials, properties, and applications, Journal of Applied Physics 100 (5) (2006) 051606. doi:10.1063/1.2336999.

[59] J. Shin, A. Goyal, S. Jesse, D. H. Kim, Single-crystal-like, c-axis oriented BaTiO3 thin films with high-performance on flexible metal templates for ferroelectric applications, Applied Physics Letters 94 (25) (2009) 252903. doi:10.1063/1.3158955.

[60] G. Arlt, H. Neumann, Internal bias in ferroelectric ceramics: Origin and time dependence, Ferroelectrics 87 (1) (1988) 109–120. doi:10.1080/00150198808201374.

[61] Z. Luo, S. Pojprapai, J. Glaum, M. Hoffman, Electrical fatigue-induced cracking in lead zirconate titanate piezoelectric ceramic and its influence quantitatively analyzed by refatigue method, Journal of the American Ceramic Society 95 (8) (2012) 2593–2600. doi:10.1111/j.1551-2916.2012.05232.x.

[62] R. V. Vedrinskii, V. L. Kraizman, A. A. Novakovich, P. V. Demekhin, S. V. Urazhdin, Pre-edge fine structure of the 3d atom K x-ray absorption spectra and quantitative atomic structure determinations for ferroelectric perovskite structure crystals, Journal of Physics: Condensed Matter 10 (42) (1998) 9561–9580. doi:10.1088/0953-8984/10/42/021.

[63] F. De Groot, G. Vankó, P. Glatzel, The 1s X-ray absorption pre-edge structures in transition metal oxides, Journal of physics. Condensed matter : an Institute of Physics journal 21 (2009) 104207. doi:10.1088/0953-8984/21/10/104207.

[64] A. Anspoks, D. Bocharov, J. Purans, F. Rocca, A. Sarakovskis, V. Trepakov, A. Dejneka, M. Itoh, Local structure studies of SrTi16O3 and SrTi18O3, Physica Scripta 89 (4) (2014) 044002. doi:10.1088/0031-8949/89/04/044002.

[65] P. Blanchard, A. Grosvenor, Investigating the local structure of B-site cations in (1-x)BaTiO3 - xBiScO3 and (1-x)PbTiO3 - xBiScO3 using X-ray absorption spectroscopy, Solid State Sciences 79 (03 2018). doi:10.1016/j.solidstatesciences.2018.02.018.

[66] D. Fu, M. Itoh, S.-y. Koshihara, T. Kosugi, S. Tsuneyuki, Anomalous phase diagram of ferroelectric (Ba,Ca)TiO3 single crystals with giant electromechanical response, Phys. Rev. Lett. 100 (2008) 227601. doi:10.1103/PhysRevLett.100.227601.

[67] D. Fu, M. Itoh, S. Koshihara, Invariant lattice strain and polarization in BaTiO3-CaTiO3 ferroelectric alloys, Journal of Physics: Condensed Matter 22 (5) (2010) 052204. doi:10.1088/0953-8984/22/5/052204.

[68] I. Levin, E. Cockayne, V. Krayzman, J. C. Woicik, S. Lee, C. A. Randall, Local structure of Ba(Ti,Zr)O3 perovskite-like solid solutions and its relation to the band-gap behavior, Phys. Rev. B 83 (2011) 094122. doi:10.1103/PhysRevB.83.094122.

[69] A. Bootchanont, J. Jutimoosik, S. Chandarak, M. Unruan, S. Rujirawat, R. Yimnirun, R. Guo, A. Bhalla, Investigation of local structure in BaTiO3-BaZrO3 system by synchrotron x-ray absorption spectroscopy, Ceramics International 39 (2013) S579 – S582, the 8th Asian Meeting on Electroceramics (AMEC-8). doi:https://doi.org/10.1016/j.ceramint.2012.10.139.

[70] M. Yashima, T. Hoshina, D. Ishimura, S. Kobayashi, W. Nakamura, T. Tsurumi, S. Wada, Size effect on the crystal structure of barium titanate nanoparticles, Journal of Applied Physics 98 (1) (2005) 014313. doi:10.1063/1.1935132.

[71] I. N. Leontyev, O. E. Fesenko, N. G. Leontyev, B. Dkhil, Ferroelectric BaTiO3 single crystal under superstrong electric fields up to 55 MV/m: A comparative experimental and theoretical study, Applied Physics Letters 96 (14) (2010) 142904. doi:10.1063/1.3386537.

[72] S. B. Seshadri, A. D. Prewitt, A. J. Studer, D. Damjanovic, J. L. Jones, An in situ diffraction study of domain wall motion contributions to the frequency dispersion of the piezoelectric coefficient in lead zirconate titanate, Applied Physics Letters 102 (4) (2013) 042911. doi:10.1063/1.4789903.

[73] Y. Ehara, S. Yasui, T. Oikawa, T. Shiraishi, T. Shimizu, H. Tanaka, N. Kanenko, R. Maran, T. Yamada, Y. Imai, O. Sakata, N. Valanoor,

H. Funakubo, In-situ observation of ultrafast 90 domain switching under application of an electric field in (100)/(001)-oriented tetragonal epitaxial Pb(Zr0.4Ti0.6)O3 thin films, Scientific Reports 7 (1) (2017) 9641. doi:10.1038/s41598-017-09389-6.

[74] R. F. Pettifer, O. Mathon, S. Pascarelli, M. D. Cooke, M. R. J. Gibbs, Measurement of femtometre-scale atomic displacements by X-ray absorption spectroscopy, Nature 435 (7038) (2005) 78–81. doi:10.1038/nature03516.

[75] J. Purans, N. D. Afify, G. Dalba, R. Grisenti, S. De Panfilis, A. Kuzmin, V. I. Ozhogin, F. Rocca, A. Sanson, S. I. Tiutiunnikov, P. Fornasini, Isotopic effect in extended X-ray-absorption fine structure of germanium, Phys. Rev. Lett. 100 (2008) 055901. doi:10.1103/PhysRevLett.100.055901.

[76] M. Kousa, S. Iwasaki, N. Ishimatsu, N. Kawamura, R. Nomura, S. Kakizawa, M. Mizumaki, H. Sumiya, T. Irifune, Element-selective elastic properties of Fe65Ni35 invar alloy and Fe72Pt28 alloy studied by extended x-ray absorption fine structure, High Pressure Research 40 (1) (2020) 130–139. doi:10.1080/08957959.2019.1702175.

[77] J. Timoshenko, A. Kuzmin, J. Purans, Reverse monte carlo modeling of thermal disorder in crystalline materials from EXAFS spectra, Computer Physics Communications 183 (6) (2012) 1237 – 1245. doi:10.1016/j.cpc.2012.02.002.

[78] P. Fornasini, Study of lattice dynamics via extended x-ray absorption fine structure, Journal of Physics: Condensed Matter 13 (34) (2001) 7859–7872. doi:10.1088/0953-8984/13/34/324.

[79] X. Moya, E. Stern-Taulats, S. Crossley, D. González-Alonso, S. Kar-Narayan, A. Planes, L. Mañosa, N. D. Mathur, Giant electrocaloric strength in single-crystal BaTiO3, Advanced Materials 25 (9) (2013) 1360–1365. doi:10.1002/adma.201203823.

[80] I. Jonane, A. Anspoks, G. Aquilanti, A. Kuzmin, High-temperature X-ray absorption spectroscopy study of thermochromic copper molybdate, Acta Materialia 179 (2019) 26–35. doi:10.1016/j.actamat.2019.06.034.

[81] N. Ishimatsu, S. Iwasaki, M. Kousa, S. Kato, N. Nakajima, N. Kitamura, N. Kawamura, M. Mizumaki, S. Kakizawa, R. Nomura, T. Irifune, H. Sumiya, Elongation of Fe-Fe atomic pairs in the invar alloy

Fe65Ni35, Phys. Rev. B 103 (2021) L220102. doi:10.1103/PhysRevB.103.L220102.

[82] A. Di Cicco, F. Iesari, Advances in modelling X-ray absorption spectroscopy data using reverse monte carlo, Phys. Chem. Chem. Phys. 24 (2022) 6988–7000. doi:10.1039/D1CP05525A.

[83] F. m. c. Farges, G. E. Brown, J. J. Rehr, Ti K-edge xanes studies of ti coordination and disorder in oxide compounds: Comparison between theory and experiment, Phys. Rev. B 56 (1997) 1809–1819. doi:10.1103/PhysRevB.56.1809.

[84] S. Kato, N. Nakajima, S. Yasui, S. Yasuhara, D. Fu, J. Adachi, H. Nitani, Y. Takeichi, A. Anspoks, Dielectric response of BaTiO3 electronic states under AC fields via microsecond time-resolved X-ray absorption spectroscopy, Acta Materialia 207 (2021) 116681. doi:10.1016/j.actamat.2021.116681.

[85] B. Ravel, E. Stern, Local disorder and near edge structure in titanate perovskites, Physica B: Condensed Matter 208-209 (1995) 316 – 318, proceedings of the 8th International Conference on X-ray Absorption Fine Structure. doi:10.1016/0921-4526(94)00686-P.

[86] U. Chon, H. M. Jang, M. G. Kim, C. H. Chang, Layered perovskites with giant spontaneous polarizations for nonvolatile memories, Phys. Rev. Lett. 89 (2002) 087601. doi:10.1103/PhysRevLett.89.087601.

[87] B. Ravel, M. Newville, *ATHENA*, *ARTEMIS*, *HEPHAESTUS*: data analysis for X-ray absorption spectroscopy using *IFEFFIT*, Journal of Synchrotron Radiation 12 (4) (2005) 537–541. doi:10.1107/S0909049505012719.

[88] G. Calas, J. Petiau, Coordination of iron in oxide glasses through high-resolution k-edge spectra: Information from the pre-edge, Solid State Communications 48 (7) (1983) 625–629. doi:https://doi.org/10.1016/0038-1098(83)90530-6.

[89] T. E. Westre, P. Kennepohl, J. G. DeWitt, B. Hedman, K. O. Hodgson, E. I. Solomon, A multiplet analysis of fe k-edge 1s $\rightarrow$ 3d pre-edge features of iron complexes, Journal of the American Chemical Society 119 (27) (1997) 6297–6314. doi:10.1021/ja964352a.

[90] S. DeBeer George, P. Brant, E. I. Solomon, Metal and ligand k-edge xas of organotitanium complexes: Metal 4p and 3d contributions to

pre-edge intensity and their contributions to bonding, Journal of the American Chemical Society 127 (2) (2005) 667–674, pMID: 15643891. doi:10.1021/ja044827v.

[91] F. Farges, Ab initio and experimental pre-edge investigations of the mn k-edge xanes in oxide-type materials, Phys. Rev. B 71 (2005) 155109. doi:10.1103/PhysRevB.71.155109.

[92] P. C. Angelomé, L. Andrini, M. E. Calvo, F. G. Requejo, S. A. Bilmes, G. J. A. A. Soler-Illia, Mesoporous anatase tio2 films: Use of ti k xanes for the quantification of the nanocrystalline character and substrate effects in the photocatalysis behavior, The Journal of Physical Chemistry C 111 (29) (2007) 10886–10893. doi:10.1021/jp069020z.

[93] C. N. W. Darlington, W. I. F. David, K. S. Knight, Structural study of barium titanate between 150 and 425 k, Phase Transitions 48 (4) (1994) 217–236. doi:10.1080/01411599408213215.

[94] H. D. Megaw, J. D. Bernal, Temperature changes in the crystal structure of barium titanium oxide, Proceedings of the Royal Society of London. Series A. Mathematical and Physical Sciences 189 (1017) (1947) 261–283. doi:10.1098/rspa.1947.0038.

[95] S. Miyake, R. Ueda, On phase transformation of BaTiO3, Journal of the Physical Society of Japan 2 (5) (1947) 93–97. doi:10.1143/JPSJ.2.93.

[96] L. Fan, J. Chen, Y. Ren, Z. Pan, L. Zhang, X. Xing, Unique piezoelectric properties of the monoclinic phase in Pb(Zr,Ti)O3 ceramics: Large lattice strain and negligible domain switching, Phys. Rev. Lett. 116 (2016) 027601. doi:10.1103/PhysRevLett.116.027601.

[97] S. Kim, G. P. Khanal, H.-W. Nam, M. Kim, I. Fujii, S. Ueno, C. Moriyoshi, Y. Kuroiwa, S. Wada, In-situ electric field induced lattice strain response observation in BiFeO3-BaTiO3 lead-free piezoelectric ceramics, Journal of the Ceramic Society of Japan 126 (5) (2018) 316–320. doi:10.2109/jcersj2.17259.

[98] R. R. Mehta, B. D. Silverman, J. T. Jacobs, Depolarization fields in thin ferroelectric films, Journal of Applied Physics 44 (8) (1973) 3379–3385. doi:10.1063/1.1662770.

[99] W. J. Merz, Switching time in ferroelectric BaTiO3 and its dependence on crystal thickness, Journal of Applied Physics 27 (8) (1956) 938–943. doi:10.1063/1.1722518.

[100] P. Glogar, V. Janovec, On the dependence of the coercive field of BaTiO3 single crystals on their thickness, Cechoslovackij fiziceskij zurnal B 13 (4) (1963) 261–265. doi:10.1007/BF01688463.

[101] V. Janovec, On the theory of the coercive field of single-domain crystals of BaTiO3, Cechoslovackij fiziceskij zurnal 8 (1) (1958) 3–15. doi:10.1007/BF01688741.

[102] J. Y. Jo, Y. S. Kim, T. W. Noh, J.-G. Yoon, T. K. Song, Coercive fields in ultrathin BaTiO3 capacitors, Applied Physics Letters 89 (23) (2006) 232909. doi:10.1063/1.2402238.

[103] J. T. Last, Infrared-absorption studies on barium titanate and related materials, Phys. Rev. 105 (1957) 1740–1750. doi:10.1103/PhysRev.105.1740.

[104] J. D. Freire, R. S. Katiyar, Lattice dynamics of crystals with tetragonal BaTiO3 structure, Phys. Rev. B 37 (1988) 2074–2085. doi:10.1103/PhysRevB.37.2074.

[105] V. Dwij, B. K. De, G. Sharma, D. Shukla, M. Gupta, R. Mittal, V. Sathe, Revisiting eigen displacements of tetragonal BaTiO3: Combined first principle and experimental investigation, Physica B: Condensed Matter 624 (2022) 413381. doi:10.1016/j.physb.2021.413381.

[106] S. Kim, S. Noda, T. Abe, Y. Yokoi, Y. Nakahira, C. Moriyoshi, Y. Kuroiwa, Electric-field-induced structural changes for cubic system of lead-free and lead-based perovskite-type oxides, Japanese Journal of Applied Physics 59 (SP) (2020) SPPA05. doi:10.35848/1347-4065/aba554.

[107] K. H. Ehses, H. Bock, K. Fischer, The temperature dependence of the debye-waller-factor in barium titanate, Ferroelectrics 37 (1) (1981) 507–510. doi:10.1080/00150198108223468.

[108] A. Pinczuk, E. Burstein, S. Ushioda, Raman scattering by polaritons in tetragonal BaTiO3, Solid State Communications 7 (1) (1969) 139–142. doi:/10.1016/0038-1098(69)90711-X.

[109] P. Lagos L, R. Hermans Z, N. Velasco, G. Tarrach, F. Schlaphof, C. Loppacher, L. M. Eng, Identification of ferroelectric domain structures in BaTiO3 for raman spectroscopy, Surface Science 532-535 (2003) 493–500, proceedings of the 7th International Conference on Nanometer-Scale Science and Technology and the 21st European Conference on Surface Science. doi:/10.1016/S0039-6028(03)00138-9.

[110] P. Lottici, J. Rehr, A connection between raman intensities and exafs debye-waller factors in amorphous solids, Solid State Communications 35 (7) (1980) 565–567. doi:/10.1016/0038-1098(80)90899-6.

[111] P. P. Lottici, Extended x-ray-absorption fine-structure debye-waller factors and vibrational density of states in amorphous arsenic, Phys. Rev. B 35 (1987) 1236–1241. doi:10.1103/PhysRevB.35.1236.

[112] C. Y. Yang, M. A. Paesler, D. E. Sayers, Determination of bond strengths of arsenic and arsenic chalcogen compounds using the temperature dependence of extended x-ray-absorption fine structure, Phys. Rev. B 36 (1987) 980–988. doi:10.1103/PhysRevB.36.980.

[113] S. Mansouri, S. Jandl, M. Balli, J. Laverdière, P. Fournier, D. Z. Dimitrov, Raman and crystal field studies of Tb-O bonds in TbMn2O5, Phys. Rev. B 94 (2016) 115109. doi:10.1103/PhysRevB.94.115109.